Universidade de Aveiro Departamento de Biologia
2017

Diana Sofia Conduto António

Detection and characterization of silver and titania nanomaterials in biological and environmental matrices

Detecção e caracterização de nanomateriais de prata e titânio em matrizes biológicas e ambientais

Universidade de Aveiro Departamento de Biologia
2017

Diana Sofia Conduto António

DETECTION AND CHARACTERIZATION OF SILVER AND TITANIA NANOMATERIALS IN BIOLOGICAL AND ENVIRONMENTAL MATRICES

DETECÇÃO E CARACTERIZAÇÃO DE NANOMATERIAIS DE PRATA E TITÂNIO EM MATRIZES BIOLÓGICAS E AMBIENTAIS

Tese apresentada à Universidade de Aveiro para cumprimento dos requisitos necessários à obtenção do grau de Doutor em Biologia, realizada sob a orientação científica dos Doutores António José Arsénia Nogueira, Professor associado em agregação do Departamento de Biologia da Universidade de Aveiro, e Luigi Calzolai, Investigador principal do Centro Comunitário de Invetigação da Comissão Europeia

I would like to dedicate this work to the Nanobiosciences working group of JRC for the great introduction to the ‘nano-world’.

o júri

presidente

Prof. Doutor João Carlos de Oliveira Matias

professor catedrático do Departamento de Economia, Gestão, Engenharia Industrial e Turismo da Universidade de Aveiro

Prof. Doutor Amadeu Mortágua Velho da Maia Soares

professor catedrático do Departamento de Biologia & CESAM da Universidade de Aveiro

Prof.ª Doutora Fernanda Maria Fraga Mimoso Gouveia e Cássio

professora associada com agregação do Departamento de Biologia & CBMA da Escola de Ciências da Universidade do Minho

Prof. Doutor António José Arsénia Nogueira

professor associado com agregação do Departamento de Biologia & CESAM da Universidade de Aveiro

Prof. Doutor José Luis Capelo Martinez

professor auxiliar do Departamento de Química da Faculdade de Ciências e Tecnologia da Universidade Nova de Lisboa

Doutor Douglas Gilliland

Scientific Officer at Joint Research Centre, European Commission, Italy

agradecimentos

Agradeço à minha família o incansável apoio e aos meus colegas sem os quais não teria chegado aqui.

palavras-chave Nanopartículas, prata, óxido de titânio, caracterização, matrizes complexas, fracionamento por campo e fluxo assimétrico, tomografia 3D.

resumo

A nanotecnolgia tem tido um impacto significativo em muitas áreas devido às peculiares propriedades dos nanomateriais (NM). O crescent uso de NM em diversos sectores da indústria veio aumentar a preocupação, a nível científico e legislativo, em desenvolver produtos mais benéficos mas com menor impacto ecológico. Uma das maiores limitações de ambos os sectores, científico e legislativo, é a capacidade de detectar e caracterizar NM. Diversas técnicas têm vindo a ser desenvolvidas durante as últimas décadas, mas a maioria apresenta limitações na capacidade de análise de NM em matrizes complexas. Geralmente é necessário combinar várias técnicas analíticas para obter dados satisfatórios. Neste estudo focamo-nos em algumas dessas limitações. Com o uso de técnicas complementares foi possível desenvolver um método de detecção e caracterização de nanopartículas (NP) em matrizes complexas mais robusto e compreensivo. O foco foi dado ao desenvolvimento de métodos alternativos de detecção e caracterização de partículas de titânio em produtos comerciais, e de prata em ambiente marinho e organismos marinhos. Foi proposta a combinação de análises por AF4/UV-Vis/MALS/DLS, após extracção por CO_2 supercrítico, para detecção de NP de titânio em cremes solares. Este método poderá ser adaptado à caracterização de NP de titânio em águas recriacionais. A detecção de NP de prata em águas marinhas baseou-se na combinação das técnicas de AF4/UV-Vis/DLS, que poderão ser usadas, por exemplo, na avaliação do potencial tóxico de águas residuais em zonas costeiras. Propôs-se a determinação da concentração de NP por análise de ICP-MS no entanto recomendou-se o uso de TEM para identicação da sua forma. A caracterização de NP de prata mostrou-se limitada devido à instabilidade destes materiais em presença de elevada carga iónica e matéria orgânica dissolvida. Além disso, para estudos de internalização, propôs-se o uso do método desenvolvido para detecção e localização de NP de prata em células. O método, baseado em análise por TEM-EDX, foi optimizado para análise 3D de células intactas. Espera-se que este método se torne útil na avaliação dos mecanismos de acção de NP, visto permitir identificar interacções entre NP e elementos cellulares.

keywords Nanoparticles, silver, titanium dioxide, characterization, complex matrices, asymmetric flow field-flow fractionation, 3D tomography.

abstract

Nanotechnology is having a significant impact in many application fields due to the peculiar properties of nanomaterials. The rapid uptake of nanotechnology innovation to products onto the market has stimulated scientific and regulatory activities aimed at maximizing the products benefits, while minimizing their potential adverse ecological impact. One of the key problems of both scientific and regulatory development is the detection and proper characterization of nanomaterials. Several techniques have been developed during the last decades, but most of them have shortcomings, especially when analysing nanomaterials in complex matrices. The combination of several techniques is usually required to obtain enough data to characterize a nanomaterial.

In this work we addressed some of the limitations of existing methods. By using complementary techniques it was possible to develop more complete and robust methods for detection and characterization of silver and titanium dioxide nanoparticles in complex matrices. In particular, this research focused on the development of alternative approaches for detecting and characterizing titania nanoparticles in consumer products and silver nanoparticles in sea water and marine organisms. A combination of AF4/UV-Vis/MALS/DLS analysis, after spCO_2 extraction, was proposed for titania nanoparticle detection in sunscreen lotions but this method could be also adapted to characterize titania nanoparticles in recreational waters. Detection of silver nanoparticles in sea water was based on the combination of AF4/UV-Vis/DLS techniques, which could be used, for instance, to determine the toxic potential of waste water discharges in coastal areas. Determination of nanoparticles concentration was proposed by ICP-MS while TEM was recommended for shape determination. The characterization of silver nanoparticles was shown limited due to the instability of the material in the presence of high ionic strength and dissolved organic matter. Furthermore, detection and localization of silver nanoparticles in cells was developed as proxy for uptake studies. A method based on TEM-EDX analysis was optimized for whole cell imaging in 3D. This method showed the ability to identify nanoparticle interactions with cell elements and therefore is expected to become a useful tool in the mechanism of action research field.

Table of Contents

Images were acquired using a JEOL JEM 2100 TEM microscope at 200 KeV. The system was equipped with a Quantax EDS (Bruker) for EDX analysis, with element spectral resolution and sensitivity down to carbon. Grids were mounted on a high tilt holder (EM-21311 HTR, JEOL) and TEM was fully aligned before sample screening. Once a single cell was found, far from the grid boarder, the optical path was assured to be aligned and a tomogram series was acquired with *SerialEM* software (Boulder Laboratory). Prior to image series acquisition, maximum allowed rotation is determined. High tilt holder allows rotation from -60º to 60º, and selected cells were imaged for at least 60º rotation amplitude. The software automatically corrects grid deviations, avoiding high shifting of the cell. One image was acquired at each rotational degree and autofocus was automatically applied at each two degrees. Afterwards, chemical mapping of the cells was performed with *ESPRIT* software (Bruker) for, at least, the neutral stage (zero angle). When sample degradation was not visible other chemical maps were acquired at higher tilt angels. Several elements were mapped simultaneously, including carbon, silicon, chlorine, silver and osmium.

Symbols

3D	tri-dimensional
AgNP	silver nanoparticles
AF4	asymmetric flow-filed flow fractionation
CLS	centrifugal liquid sedimentation
CPS	centrifugal particle sedimentation (equivalent to CLS)
DLS	dynamic light scattering
FIB	focused ion beam
spICP-MS	single particle inductively coupled plasma mass spectrometry
NP	nanoparticles
PDI	polydispersity index
scCO2	supercritical carbon dioxide
SEM	scanning electron microscopy
TEM	transmission electron microscopy
TiO_2	titania or titanium dioxide
UV-Vis	ultraviolet tovisible spectrometry

List of figures

List of tables

1. General Introduction

1.1. Nanomaterials

Nanotechnology is having a significant impact in many fields due to their peculiar properties [2]; for example nanomaterials are currently used in many industrial fields and there are great expectations for their use as innovative medical diagnostics or improved materials. Currently nanomaterials are used in several consumer products, thus potentially coming into direct contact with the general public. This very fast translation of new materials and technology into products on the market has started scientific and regulatory activities, aimed at maximizing the benefits of products containing nanomaterials while minimizing their potential adverse effects on organisms and the environment. One of the problems facing the sector was the lack of an agreed definition of what constitute a nanomaterial. In this context, the European Commission has published in 2011 its recommendation on the definition of nanomaterials (Official Journal of the European Commission [3]).

'Nanomaterial' means a natural, incidental or manufactured material containing particles, in an unbound state or as an aggregate or as an agglomerate and where, for 50 % or more of the particles in the number size distribution, one or more external dimensions is in the size range 1 nm-100 nm.

In specific cases and where warranted by concerns for the environment, health, safety or competitiveness the number size distribution threshold of 50 % may be replaced by a threshold between 1 and 50 %.

By derogation from point 2, fullerenes, graphene flakes and single wall carbon nanotubes with one or more external dimensions below 1 nm should be considered as nanomaterials.

For the purposes of point 2, 'particle', 'agglomerate' and 'aggregate' are defined as follows:

'particle' means a minute piece of matter with defined physical boundaries;

'agglomerate' means a collection of weakly bound particles or aggregates where the resulting external surface area is similar to the sum of the surface areas of the individual components;

'aggregate' means a particle comprising of strongly bound or fused particles.'.

At the moment there are efforts to harmonize this recommended definition with slightly different definitions that are already in place in the EU legislation, such as the cosmetic directive and the food information directive [4].

1.2. Legislation on Nanomaterials in the European Union

At the moment there is no specific legislation covering nanotechnology or nanomaterials *per se* at the European Union level. There are however several regulations that explicitly cover some aspects of nanomaterial detection and characterization. Some of these regulations are already in place with legally binding obligation (Cosmetics Directive, Food Contact Materials, Food Information to Consumers, and Biocidal Products regulation). As for Plant Protection Products, nanomaterials are covered but there are no specific provisions. In other cases, such as the REACH regulation, nanoparticles are covered by the existing regulation and the practical implementations for nano-based chemicals are being discussed at the moment.

In particular, for cosmetic products, according to EC Regulation 1223/2009 (Cosmetics Directive [4]) covering cosmetic products, producers of cosmetics are obliged to notify the Commission in case they want to use ingredients in nano-form in their products. There is the obligation to add information in the label on ingredients used in nano-form. The label on the cosmetic products could include indications such as "Titanium dioxide (nano)" for example in case the product contains titanium dioxide particles smaller than 100 nanometers. This regulation has been published before the "official" EC definition of nanomaterial and thus it uses a slightly different definition of what a nanomaterial is. Work is in progress at the technical and legislative level to reconcile the two definitions and harmonize them.

1.2.1 Reach regulation

The REACH regulation (1907/2006 [5]) addresses Registration of manufactured/imported substances (in volume larger than 1 tonne per year), the Evaluation of some registration dossiers, and the Authorisation for use of substances of very high concern. There are no provisions in REACH referring specially to nanomaterials, but REACH addresses chemical

substances, in whatever size, shape or physical state. Substances at the nano-scale are therefore covered by REACH and its provisions apply. Substances at the nano-scale manufactured, or imported, in volumes of ≥ 1 tonne per year have to be registered and information requirements increase with production volumes. At volumes bigger than 1t/year a Chemical Safety Report (CSR) has to be included in the registration. The registration dossier for a nanomaterial needs to include all relevant information on that material, thus covering the properties, uses, effects and exposure related information as well as the classification and labelling and the safety assessment. Nanomaterials having specific properties may require a different classification and labelling compared to the bulk material.

At the moment there is still some uncertainty about the specific characterization of nanomaterials that should be included in the registration dossier of chemicals in nano-form.

1.3. Common uses

Nanotechnology-based products are increasingly being available to consumers in different application areas as shown by Aitken and colleagues already in 2006 [2]. Paint, cosmetics, medicines, clothing or pastry, many are the offered products. For instance, Calzolai and colleagues have assembled a list of nanomaterials used in food industry [1]. Table 1 shows a short list of nanoparticles applications in various industry sectors.

Table 1. Short list of metal and metal oxide uses in industry.

Material	**Sector**	**Use**
Titanium oxide	Food	White colouring agent (glaze)
	Cosmetics	Sun-blocker (sunscreen lotions and creams)
	Energy	Photocatalist (photovoltaic panels) [6]
	Building	Self-cleaning agent (cement finishing, paints)

Iron oxide	Food	Yellow, red and black colouring agent
	Health	Contrast agent (magnetic resonance imaging) [7]
Metallic silver	Packaging	Labelling colour (food packaging)
	Health	Antimicrobial agent (bandages, medical devices) [8]
	Clothing	Antimicrobial agent (sportswear) [9, 10]
	Remediation	Antimicrobial agent (water purification, e.g. The Drinkable book™) [11]
	Glass	Yellow colour agent
Metallic gold	Food	Colour agent
	Cosmetics	Aging treatment (creams)
	Clothing	Fabric technology (e.g. Nanofont™)
	Glass	Red colour agent
Silicon dioxide	Food	Anticaking agent (powder formulations)
	Clothing	Water and stain repellent coating [12]

The present study was based on the evaluation of titania and silver nanoparticles, reason for which only those will be commented from now on. The choice of the studied materials was based on its expected availability and impact in the aquatic environment, the physical availability of the materials for analysis and the fact that they represent two different challenges in terms of detection and characterization.

1.3.1 Titanium oxide nanoparticles

Titanium dioxide (TiO_2) is widely used in building, green energy and cosmetics industries. Self-cleaning products and photovoltaic cells are developed around the photocatalytic properties of titania. These applications use a broad size range of materials, not necessarily in the nano-range. Indeed, the use of titania nanoparticles as colouring agent in food and paint is based on the characteristic scattering of particles, bigger than 200 nm, in the visible (white) range. Sunscreen materials exploit the UV reflection capacity of the particles, using non-photocatalytic particles. These particles can be coated with other materials such as silicon, decreasing skin reactivity or toxicity [13]. Titania-based sunscreens can also use materials bigger than 100 nm in its formulations but primary particles are frequently bellow 100 nm. Moreover, particles in the nano-range show high absorbance at the UV range and low scattering at the visible region. Consequently, the whitish finishing of the cream is reduced, which is appreciated by the consumer [13, 14].

1.3.2 Silver nanoparticles

One of the most interesting properties of silver is its antimicrobial activity, which was known and exploit already by the Phoenicians. In the 1880s silver was extensively used as preventive medicine, reducing gonorrheal ophthalmia disorders in newborns. This practice was maintained until antibiotics were discovered. Several other reports of silver use along the last six millennia are known, as summarized by Alexander [15]. Introduction of colloidal silver in the health sector started in the 1900s. Nowadays silver nanoparticles (AgNP) are widely used in consumer products due to their antimicrobial properties [16]. It is used on wound bandages to avoid wound infection [17]; on food packaging to increase shelf life [18]; on sports clothes and socks to reduce the smell resulting from bacterial growth [9, 19] or on water purification systems to produce potable water [20]. The Drinkable Book™ is just one example of the many products developed for water purification, designed to fight potable water scarcity in underdeveloped countries. Rai and colleagues presented an exhaustive list of new applications of silver as antimicrobial agent [21]. The spread use of AgNP-containing products results on an estimated median worldwide production of around 55 tons per year [22].

1.4. Characterization

Detection of nanomaterials in samples or evaluation of engineered nanomaterials production requires characterization techniques. In this section a set of particle analysis methods, used in the current study, are presented.

1.4.1 Asymmetric flow field-flow fractionation

Asymmetric flow field-flow fractionation (AF4) is a one-phase chromatographic method used to separate materials by their relative size. As shown in figure 1, the separation is achieved by a combination of multi-directional forces. In principle, bigger the size of a particle, higher the impact of the separation field applied (cross-field). These results on a horizontal distribution of the samples where smaller particles are placed on the most central area of the chamber where the parabolic flow pushes them out the system earlier [23]. This is a non-informative separation method considering that it is not possible to follow the materials separation. Furthermore, materials recovery is dependent of the interactions with the membrane, both charge-dependent of physical (cross-flow force applied). Nevertheless, this method is quite useful as complement of other techniques since it allows the use of equipment, which cannot deal with polydispersed samples, in flow mode (i.e. hyphenated, connected to the out-put line). In fact, this technique is always hyphenated with other detectors, evaluating light scattering properties for instance, in order to follow the particles elution in real time.

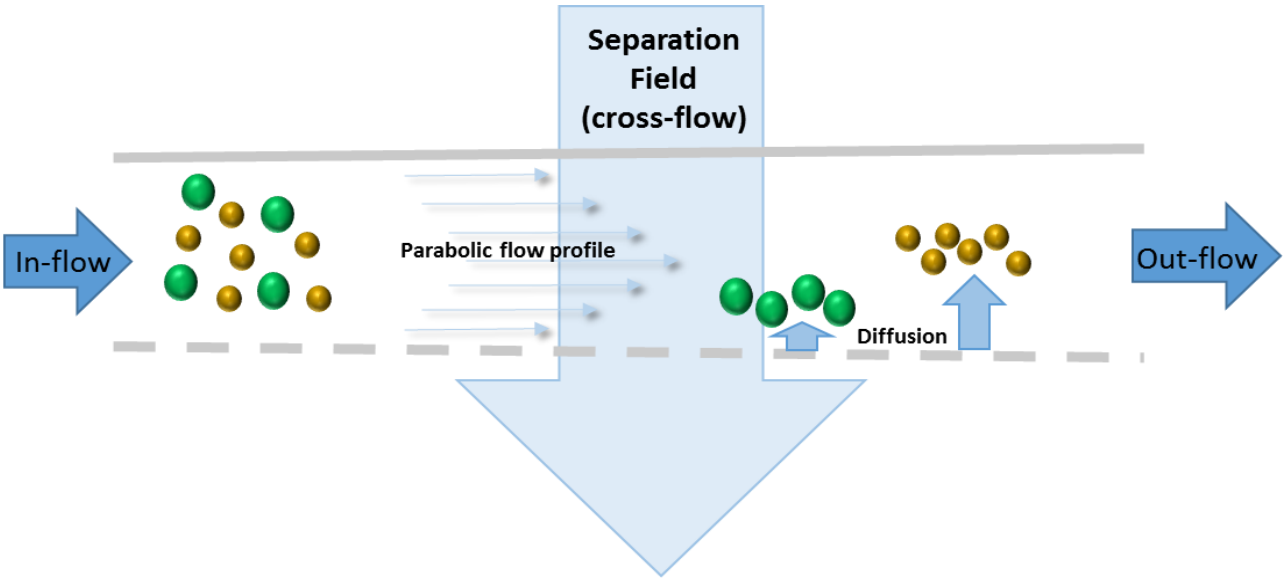

Figure 1. Schematic view of an AF4 separation channel showing the effect of the combination of cross-flow, diffusion and parabolic flow on the separation and elution of the different particle sizes.

1.4.2 Ultra violet to visible range spectroscopy

Ultra violet to visible range spectroscopy (UV-Vis) is a simple technique for evaluation of material. In molecular biology for instance it is used to determine the purity of nucleic acids and infer about the presence of proteins in the sample. In nanotechnology field, it is broadly used for instance linked to the AF4 channel, to follow nanoparticle elution. In static mode, UV-Vis is used to follow nanoparticle synthesis and evaluate their stability. Metallic particles, such as silver or gold NP in the nano-range, show size dependent localized surface plasma resonance (LSPR) which can be used to estimate the size of the particle [24]. The sensitivity of this method also allows estimation of the relative concentration of the materials. Titania NP, on the other hand, have a maximum absorbance in the UV range, similarly to proteins, which cannot be used for size evaluation [14].

1.4.3 Centrifugal liquid sedimentation

Centrifugal liquid centrifugation (CLS) is the easiest method for analysis of polydispersed nanoparticle samples. The instrument is composed of a transparent disk and a detector set to

detect crossing particles at a fixed point. The disc is filled with a gradient of sucrose and the particles, injected at the centre of the disk, are pulled towards the outer edge by a centrifugal force (figure 2). Particles travel-velocity is mainly dependent on their mass and therefore density. At constant density, higher than the density of the sucrose, particle centrifugal velocity is related to the particle size [25]. The hydrodynamic size of a particle is calculated based on the velocity of migration in the gradient, at a fixed RI and density. The main limitation of this method is the density factor. Particles of unknown density such as aggregated particles or coated particles, give misleading measurements. For instance, organic coatings can decrease the overall density of the complex, decreasing the centrifugal velocity of the particle and therefore decreasing the reported size compared to the equivalent nude material [26].

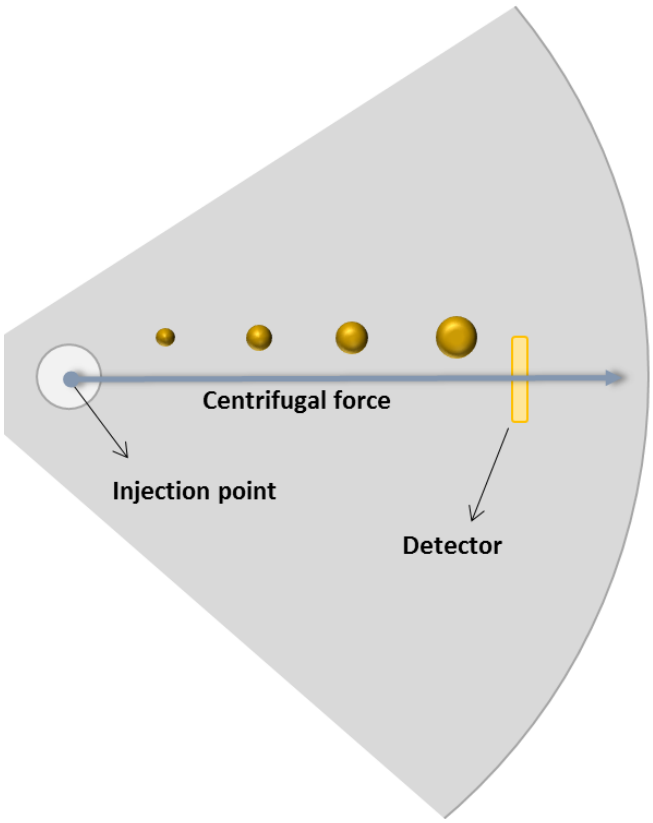

Figure 2. Schematic representation of the CLS disk showing the injection point and the applied centrifugal force in the detector direction. The particles orientation represents the direct size dependency on centrifugal velocity.

1.4.4 Dynamic light scattering

The quickest method for particle sizing is the dynamic light scattering (DLS). Based on materials RI and their back-scattering properties, this method is able to measure the hydrodynamic size of a material. The main limitation of this technique is the fact that it cannot deal with polydispersed samples [27]. Particles light scattering intensity depends on the particle radius by the sixth power [28, 29]. Accordingly, the presence of big particles, even at low number, will mask the signal of smaller ones [30]. Nevertheless, this instrument can be linked to a size exclusion equipment, such as AF4, working in (real-time) flow mode. Able to deal with diluted samples [31], the decreased concentration of a sample after AF4 separation is, at a certain extent, not problematic.

1.4.5 Multi-angle light scattering

Multi-angle light scattering (MALS) is a technique broadly used in biochemistry. It allows the determination of the molecular weight materials, being useful for protein crystallography studies [32]. This is also one of the most used detectors to evaluate AF4 separation. In the field on nanotechnology, MALS as the power to retrieve a materials' size distribution. Fitting the light scattering data of several angles into the most suitable model, one can retrieve the radius of gyration (R_G) of a material. The radius of gyration gives an indication of the particle size (similarly to hydrodynamic size). If another technique is used to determine the hydrodynamic radius (R_H), the radius of gyration can also be used to determine the shape factor (R_G/R_H) of the particle [33, 34]. The main constrain of this method for nanoparticle evaluation lays on the fact that the R_G can only be calculated if there is an angular light scattering dependence. In fact small particles (usually near 10 nm) may not show such dependence, being called isotropic materials. Another type of isotropic materials are metallic colloids, like silver [35].

1.4.6 Transmission electron microscopy

Electron microscopy is a comprehensive technique allowing acquisition of an interesting set of data and applicable to various types of samples. Electron microscopy allows evaluation of

geometric size and shape of particles, aggregation state and quantitative dispersion status of a sample. Transmission electron microscopy (TEM) can also be used to evaluation metals crystalline pattern. Inorganic samples can be directly spotted into support grids and imaged once dried. In the case of organic samples, such as microorganisms, the high-vacuum environment inside the instrument obliges to a more complex protocol. A complete dehydration of the sample is required, which may cause deformation of the cell if suitable protocols are not used. As for coated nanoparticles, TEM resolution allows imaging of hard materials only. Organic coating such as with proteins or organic matter cannot be sized. Sample dehydration invalidates the evaluation of the coating thickness and even mask their presence. Furthermore, those techniques are expensive and the sample preparation and imaging complexity are prohibitive for performance of numerous routine measurements. Nevertheless, it is the only method that allows shape and geometrical size evaluation of hard materials. It is also quite spread among toxicologists. Being a resourceful technique, adaptation of the instrument can allow imaging of resin embedded or cryo-preserved samples [36, 37]. It can use a broad set of sample supports depending on the data analysis requirements. For instance, it allows tri-dimensional evaluation of a sample. Furthermore, it can be coupled with chemical identification instruments to map the presence and distribution of elements in the sample [38].

1.4.7 Energy dispersive X-ray spectroscopy

Energy dispersive X-ray spectroscopy (EDX) is an interesting technique to analyse, or map, the chemical composition of a surface. Coupling EDX with electron microscopy covers the main limitation of the second, the identification of the analytes' elemental composition. Briefly, the chemical determination is based on the detection of the x-ray emissions (measured in Volts) once the sample surface is bombarded with an electrons focused beam. The rastering of the beam allows clear mapping of several elements, simultaneously, in the analysed area. EDX is a destructive technique and therefore used as an end-point analysis. Chemical detection is dependent on the atomic number of the element and the sensitivity of the instrument. Some EDX systems are not able to detect elements with atomic number below 10 although the theoretical limitation lies between 4 and 92 (information from Jeol Ltd.).

1.4.8 Single particle ion-coupled plasma mass spectrometry

Ion-coupled plasma mass spectrometry (ICP-MS) is an ideal method for chemical identification of highly diluted samples. It is able to detect trace amounts of inorganic elements. For nanoparticle characterization, it is a useful but expensive technique. There are a set of standard material available for ICP-MS analysis which allow quantification of elements on their ionic form. Mass back calculation allows extrapolation of the bulk material concentration in the initial sample. The measurements accuracy is strongly dependent of sample pre-digestion [39], however studies on quantification of materials with no prior digestion shown interesting results [40]. The principle of this technique is based on the passage of a material by an inductive plasma cell were it is vaporized by an inert gas. The resulting ions are measured by mass spectrometry and the recorded average background to signal obtained is proportional to the concentration of the element in the sample. Operated in the 'single particle' mode (spICP-MS), which means at a reduced flow and using extremely high dilution factors, the technique allows the detection of individual nanoparticles. Theoretically, high dilution of nanoparticle-containing samples allows the passage of single particles in the nebulizer chamber (figure 3). In this situation, measurements are recorded in a time resolution ranging 10 to 20 milliseconds. The correspondent measured signal converted to mass will provide an indication of the particle size. This method can give information not only on the elemental composition of a nanomaterial but also on its size distribution. The sizing is however based on a theoretical shape. The accuracy of the measurements depends on full ionization of the nanoparticles and on optimization of dilution and flow, in order to have no coincident particles or particle fractions in the nebulizer chamber. As shown by Mitrano and colleagues, this technique allows evaluation of nanoparticle dissolution kinetics in complex systems, where chloride or organic matter are present, following the size variation in time and the changes on the ionic content of the sample [41].

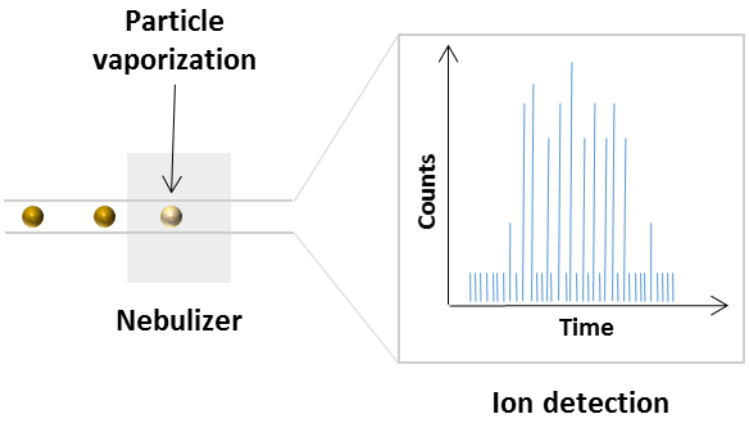

Figure 3. Schematic representation of the spICP-MS system showing ionization of single particles in the plasma cell and recorded peak signals.

1.5. Comparison of characterization methods

Each instrument has the potential to give a specific set of information and has certain limitation. Table 2 summarizes some of the available data on the above referred techniques. The suitability of the different techniques, with respect to several nanoparticle characterization parameters, was considered on an array of studies presented from *Chapter I* to *Chapter VII*.

Table 2. Summary of instruments informative potential and its limitations.

Instrument	Size	Shape	Chemical composition	Dispersion	Requirements	Limitation	Data analysis	Analysis cost	Analysis time
CLS	Hydrodinamic diameter	No	No	Yes	Known RI and density	Only spheric materials	Easy	Low	Inversely dependent on size
DLS	Hydrodinamic diameter	No	No	No	Known RI	Only spheric and monodispersed materials	Easy	Low	Low
MALS	Radius of gyration	Theoretical	No	Yes	Angle dependent scattering	R_G only for anisotropic materials	Difficult	Low	Medium
UV-Vis	Approximate size by calibration dependent		No	Qualitative	Optimized concentration	Only materials with LSPR	Easy	Low	Low
AF4	No	No	No	No	Optimized carrier and membrane	Charged materials, sizes over 200 nm	Easy	Medium	Medium
ICP-MS	No	No	Yes	No	Standards availability		Difficult	High	High

Instrument	Size	Shape	Chemical composition	Dispersion	Requirements	Limitation	Data analysis	Analysis cost	Analysis time
spICP-MS	Calculated from ion mass	No	Yes	Yes	Optimized particle flow and dilution		Difficult	High	High
SEM	Geometric size, bidimensional	Real, bidimensional	No	Yes	Sample preparation	Non-organic materials	Easy	Medium	Low
TEM	Geometric size	Real	Only based on crystalline structure pattern	Yes	Sample preparation	Non-organic materials	Easy	High	Medium
EDX	No	No	Yes	No	Atomic number from 4 to 92	Elements of atomic number below 10	Easy	Medium	Medium

Another interesting aspect of techniques comparison was reported by Calzolai and colleagues and presented in table 3 [1]. For consideration, field flow fractionation and centrifugal particle sedimentation are directly comparable with asymmetric field flow-field fractionation and centrifugal liquid sedimentation, respectively.

Table 3. Qualitative evaluation of the relative advantages and disadvantages of different techniques to measure the size of nanoparticles in the 1-100 nm size range. (adapted from [1])

	SEM	**TEM**	**FFF**	**CPS**	**DLS**	**spICP-MS**
Minimum size	++	+++	+++	+	+++	+
Dynamic range	+++	++	++	+++	+++	++
Accuracy of measure	++	++	+	+	+	+
Suitable for mixtures	+	+	++	++	-	++
In situ measure	-	-	+	+	++	++
Easy of use	-	-	+	++	++	+
Cost	-	-	++	++	+++	+

Notes: Different properties are evaluated as: excellent (+++), good (++), fair (+) and insufficient (-).
CPS, centrifugal particle sedimentation; DLS, dynamic light-scattering; FFF, field flow fractionation; SEM, scanning electron microscopy; spICP-MS, single particle inductively coupled plasma mass spectrometry; TEM, transmission microscopy.

Overall, the more accurate evaluation of particle size, morphology and distribution are based on electron microscopy. The main *cons* are the price and the difficulty on analysing organic materials. NP protein coating, for instance, is very difficult to detect with conventional EM

due to the low contrast of the organic protein layer. The simplest technique for size determination is DLS although it cannot be used with polydispersed samples, therefore, in such situations, CLS is the preferential technique. However, to reduce analysis costs and to fully characterize a material, we must combine different instruments. Since CLS is an end-point analysis, it can be used only as indication, for instance in protocol optimization. Similarly, electron microscopy is reserved as complementary analytic system for when shape information is crucial or retrieved data must be confirmed. Consequently, AF4 is the elected method for analysis of polydispersed samples, allowing separation of the materials by size and hyphenation of other detectors, such as DLS, MALS, UV-Vis or even ICP-MS.

1.6. Sample treatment strategies

Matrix complexity and nanoparticles concentration are sometimes limiting direct analysis of samples. Analytic methods such as AF4, CLS or ICP-MS frequently require sample pre-treatment. Fluidification of the matrix is often the main reason although it can also be used to avoid clogging the system tubing of altering the fluidic density, among others. Nevertheless, pre-treatment can also be adopted to reduce the complexity of the matrix. Chemical-based extraction is often chosen although it requires use of hazardous materials. Environmental friend alternatives are available, such as supercritical fluid extraction. In our study, supercritical CO_2 extraction was attempted for matrix simplification.

1.6.1 Supercritical CO_2 extraction

Supercritical fluid extraction is a method based on the use of a superfluid to remove polar components of a complex matrix. The use of carbon dioxide as superfluid is called supercritical CO_2 ($scCO_2$) extraction. This technique can be used either to remove compounds from a desired sample, e.g. to remove caffeine from coffee grains, or to extract desired compounds from a sample, e.g. to extract essential oils from herbs [42]. Cosmetic products are composed, among others, of fatty and non-polar compounds which exhibit a high solubility in CO_2. This technique, in opposition to chemical based extraction protocols, is ecologically safer and simpler in preparation. For the extraction, pressure is increased in order

to allow diffusion of $scCO_2$ in the sample, solubilizing non-polar and small compounds, maintaining the structure of the remaining material [43]. Extraction temperature can be controlled to optimize the process. By lowering the pressure bellow the critical threshold and the temperature to ambient conditions, the compounds are removed together with the CO_2. For the purpose of our study, simplification of sunscreen lotion matrix was envisaged and therefore the remaining of the extraction was used, therefore we have used inverse $scCO_2$ extraction.

1.7. Nanoparticles toxicity

Nanotechnology has found application in many industrial sectors, increasing the number of industrial and commercial available products in the market. Consequently, the production tonnage of such materials continues increasing and the related waste amounts as well. Concern regarding its potential toxicological impact, in humans health and environment, are a natural consequence. Titania and silver NP were shown to affect the cell performance. Instability of nanoparticles in culture media is widely known although the toxicity of the materials is not necessarily reduced in such conditions. Photo-reactive capacity of TiO_2 NP increase formation of reactive oxygen species, linked to oxidative stress and cell damage [44]. The impact of titania materials is not restricted to mammalian cell lines. Toxicity at the level of the phytoplanktonic community was also reported [45] although it is not consensual [46]. Potentiating hazardous effect of other toxics by TiO_2 NP was equally reported [47]. Silver nanoparticles were also found to promote oxidative stress in cells in a size dependent manner [48] and to affect phytoplanktonic organisms, with consequent effect on higher trophic levels [49, 50]. Furthermore, AgNP are considered reservoirs of ionic silver (Ag^+) able to continuously, and locally, release the silver toxic form, as is of consensus that the toxic form of silver is ionic [51]. Adsorption or uptake of nanoparticles would therefore potentiate the toxicity of the material. A broad list of Ag^+ interactions with essential biological proteins and oligoelements are known. Among others, silver ions are known to bind to thiol or cysteine groups impairing protein function, such as in the case of glutathione [52, 53]; they can bind selenium [54], promoting selenium deficiency and affecting proteins with Se-Cysteine bounds [54-57]; and can also inhibits glucose oxidase [58], inhibiting the reduction of FAD to FADH2 and consequently blocking the respiratory chain. A general awareness grew within

the toxicologists community with regards to the limitations of 'traditional' tests, used for dissolved compounds, for evaluation of nanomaterials [59].

1.8. NP disposal and environmental interactions

Nanoparticles can enter the environment by diverse routes. Titania nanoparticles, used in cements, paints and other building materials can enter aquatic systems through leaching [60, 61]. Others used in food industry end up in solid wastes and waste water treatment plants. Finally, cosmetic additives such as sunscreen creams can directly enter aquatic environments, result of recreational activities. Silver concentration in open ocean is in the range of 0.05 to 5 ng/L [62, 63]. In coastal areas, dissolved silver concentrations may surpass 30 ng/L [62, 64]. These values may be expected to increase specially in coastal areas due to the increased exploitation of nanomaterial in diverse industrial sectors. Nanomaterials present in building or daily use products represent potential environmental hazards. Through products disposal or accidental leaching [60] and by different routes, NP are expected to enter the aquatic ecosystem. Several studies have analysed nanoparticle leaching and fate of nanomaterials in waste water treatment plants. Waste water treatment plants and soil are the first expected reservoirs as natural soil leaching and discharge of water treatment plants are likely to be the main routes for contamination of aquatic system. Indeed, silver NP leaching from soil is expected low since particles seem to strongly bound to the soil particles [65]. Retention, although lowering the expected concentration of silver in the aquatic system, can represent an increased risk for soil microbiota and lower invertebrates [66, 67]. Additionally, silver nanoparticles entering WWTP seem to be mostly complexed and precipitated, end-upping in the solid fraction [68]. Therefore the use of the sewage sludge for agriculture is conditioned. Silver materials entering the aquatic system will also suffer modifications. Many are the transformations and interactions known to particles. Light, temperature, ionic strength, oxygenation and presence of organic matter are some of the factors that can affect AgNP agglomeration, aggregation and oxidative release of silver ions, influencing AgNP toxic potential [69-72]. In the presence of chloride, and depending on its concentration, silver forms soluble ($AgCl^-$) or insoluble species ($AgCl_3^{2-}$ and $AgCl_2^-$) [73]. Furthermore, it reacts strongly with thiol groups and organic compounds found in the environment. Silver reaction with sulphur can attenuate its noxious environmental impact [16]. However, particles

degradation depends on the presence and power of stabilizer agents, which cover a broad range of materials from organic coatings, such as citrate, proteins or dissolved organic matter (DOM), to harder materials, such as PVP or silica shells.

1.9. Effect of DOM

Alginate and humic acid are two components of DOM, present in aquatic environments at variable concentrations, depending on factors such as algal bloom or soil leaching [74]. Alginic acid, also called alginate, is an anionic linear polysaccharide present in the cell walls of brown algae and used by some bacteria for biofilm formation. Alginate has industrial interest being used as thickening agent in food products. Humic acid is one of the main components of organic matter in natural waters and is frequently used as model compound for the presence of DOM. Natural humic acids are available as standards for scientific work. The advantage of these materials regards alginate is the increased complexity of the polymer (branched). In fact, many studies were done with both model polymers and for that reason were chosen for this study as well. Dissolved organic matter (DOM) is expected to play an important role on AgNP and titania NP behaviour in the environment being able to change the chemical properties of the nanoparticle surface. For example, it has been shown that humic acids, components of DOM, can alter AgNP size distribution [75], similarly to what happens with TiO_2 NP [76]. Formation of DOM coating can reduce the oxidation rate of AgNP, and therefore their availability [77, 78] but it can also help the formation of non-bioavailable Ag_2S species [79]. Furthermore, considering the impact of humic acids in the increased uptake of cadmium by algae, disregards their low availability [80], one can expect similar results on the impact of silver. Regarding titania NP, oxidation and light are not retained major impairing agents although increasing ionic strength and DOM concentration have strong aggregation effect [76, 81]. Disaggregation of TiO_2 NP was also reported to be dependent on alginate concentration, affecting the availability of the potential hazard in freshwater systems [82].

1.10. Cell uptake

Nanoparticle incorporation has been intensively studied. Besides animal [83, 84] and human cell lines [85] also organisms from other trophic levels have been evaluated. Fish [86, 87] nematodes [88] and algae [89-92] are just some examples. However the uptake routes are not always known and the mechanism of action of the materials is yet not clear. The peculiarity of nanoparticles properties and the complexity of their interaction within the biological environment difficult the use of routine evaluation methods however, further evaluation is required to fill the knowledge gaps. Development of alternative evaluation methods may be a key to retrieve additional information.

1.11. Uptake evaluation

Diatoms are eukaryotic unicellular microorganisms belonging to the phytoplankton community. These cosmopolitan organisms are responsible for 20% of the carbon fixation in the oceans. Furthermore, some species are quite sensitive to pollution and eutrophycation, reason for which was for long used as ecological indicator [93, 94]. Diatoms are also used to investigate the mechanism of toxicity of chemical pollutants at the molecular level [95]. Regarding their morphology, diatoms are very interesting as they present a silica outer shell which works as a natural biofilter, considering the presence of various nano-pores. The pore size is expected to allow the internalization of nanomaterials similarly to other pollutants. For their particular morphology, size and environmental relevance, *T. pseudonana* was chosen as model organism for the development of an alternative method for cell uptake evaluation.

2. Aim of the study

Considering the vast array of different ecotoxicological tests found in literature it is thus very difficult to compare results on the effect of nanoparticles on the environment. In addition, as addressed in the previous pages the existing methods to detect and characterize nanoparticles in the environment are still not ideal. Thus, the development of accurate and robust methods to detect nanoparticles in the environment is crucial to enable the assessment of the real impact of nanoparticles in the environment

The present study aimed to develop techniques for nanoparticle detection and characterization in complex matrices. Characterization of both TiO_2 NP in consumer products and AgNP in sea water and marine organisms were addressed. Methods developed to detect titania NP in diluted sunscreen lotions where then adapted to measure the concentration of titania nanoparticles in recreational waters. Detection of AgNP in sea water could allow determination of toxic potential of waste water treatment plants discharges in coastal areas. Detection and localization of AgNP in cells is expected to improve the knowledge of NP mechanism of action, becoming an interesting tool for NP uptake studies. Therefore, the proposed approaches are expected to be transposed to 'real' environmental samples.

3. Chapter I

Strategies for the determination of the Particle Size Distribution of Titanium Dioxide. Key study on commercially-sourced materials

C. Cascio[b] , D.C. António[a], D. Mehn[a], F. Rossi[a], D. Gilliland[a], L. Calzolai[a]

[a] *NanoBioSciences, Institute for Health and Consumer Protection Unit, Joint Research Centre, European Commission, via E. Fermi, 2749, I-21027 Ispra (VA), Italy*

[b] *formerly, NanoBioSciences, Institute for Health and Consumer Protection Unit, Joint Research Centre, European Commission, via E. Fermi, 2749, I-21027 Ispra (VA), Italy*

Ready for submission to Journal of Nanoparticle Research

3.1. Abstract

Titanium dioxide is an approved food additive (colour white, E171) and a cosmetic ingredient (pigment white 6) widely used in processed food and sunscreens. The European Commission recommended definition of "nanomaterials" is based on the determination of the number-based particle size distribution (PSD) and thus a need for suitable and tailored methods, able to measure the PSD of titanium dioxide in complex matrices such as food and cosmetics, has arisen. In this work, two commercially available titanium dioxide ingredients for food and cosmetics (E171 and pigment white 6) were characterized by a battery of complementary techniques including Raman spectroscopy, Centrifugal Liquid Sedimentation (CLS), Asymmetric Flow-Field Flow Fractionation (AF4) hyphenated to Dynamic Light Scattering (DLS) and Transmission Electron Microscopy (TEM).

The set of techniques used in this study outlines a tiered approach to the determination of the PSD of titanium dioxide products. Quicker screening techniques, such as CLS, can be used to explore and optimize sample preparation protocols. More complex options (AF4 with multi-detectors and TEM) act as more general methods to obtain detailed PSD, while "identity" techniques, such as Inductively Coupled Plasma Mass Spectrometry and Raman, have firstly, confirmed the presence of titanium dioxide in the samples and secondly identified the

crystalline phase. The combination of CLS and AF4/DLS data allows the estimation of size and apparent density. In particular, both compounds analysed here were confirmed to be based on anatase; sample preparation parameters (sonication time and pH) influenced the particle size distributions. E171 and pigment white 6 showed a median diameter of around 350 nm and 250 nm, respectively, while TEM shows the presence of primary particles smaller than 100 nm, together with large number of aggregates. The results highlight the difficulties in determining the PSD of titanium dioxide in particular in the presence of strongly bound aggregates that are not easily separated into primary particles with normal sample preparation methods.

3.2. Introduction

Titanium dioxide (TiO_2) due to its UV light absorbing capacity, high refractive index and light scattering properties resulting in brilliant whiteness, is a widely used material in consumer products; it is the mostly used as a whitening pigment and it is commonly applied in a wide variety of products among which paints, inks, paper, toothpaste and ceramics; every year more than 4.5 million tons of TiO_2 are produced worldwide [1]. TiO_2 is authorized for use in the food industry where, under EU designation, it is identified as the additive E171 and commonly used as colorant [2] in processed food. TiO_2 is also an authorized ingredient in cosmetics, where it is used either as colorant (known as pigment white 6), as an opacifier agent, or as an ultraviolet radiation filter. There has been evidence in the literature that part of the food-grade titanium dioxide particles are in nano-form [3, 4] and similar evidences exist for TiO_2 used in cosmetic products [5-7]. Over 90 products containing nano-titanium are listed on the Woodrow Wilson consumer product inventory [8].

In 2011, the European Commission published its recommendation for the definition of the term nanomaterial: "Nanomaterial means a natural, incidental or manufactured material containing particles, in an unbound state or as an aggregate or as an agglomerate and where, for 50 % or more of the particles in the number size distribution, one or more external dimensions is in the size range 1 nm - 100 nm" [9]. As yet, this definition has not been implemented into the food and cosmetic sector where currently a number of different definitions of what constitute a nanomaterial are in place (ex. EU Regulation 1169/2011 on the provision of food information to consumers and EU Regulation 1223/2009 on cosmetic

products). Nevertheless, the issue of greater harmonization of legislation by a more widespread adoption of a single definition continues to be under discussion and consequently there remains an urgent need to develop methods to determine the particle size distribution of challenging materials according to the EC recommendation. It has been already highlighted that the practical application of the EC recommended definition in legislation is still hindered by the lack of single analytical methods which can easily determine whether a material should or should not be classified as a nanomaterial under the terms of this definition [10]. At the moment, no single analytical method can completely satisfy the requirement of the definition, but a variety of methods exist which, in combination, offer the possibility of addressing the problem [11]. In addition, the analysis of nanomaterials in consumer products, poses a number of difficulties due to the complexity of most matrices and the fact that sample preparation can greatly alter the resulting particle size distributions [4, 12].

In this work, two commercially available titanium dioxide ingredients, one intended for cosmetic products (white pigment 6) and the other for food products (E171) were analysed by means of various characterization techniques to determine the chemical identity and crystalline form, the variation of Zeta-potential with pH and the particle size distribution once dispersed in water. Centrifugal Liquid Sedimentation (CLS), Transmission Electron Microscopy (TEM), Raman Spectroscopy, Asymmetric Flow-Field Flow Fractionation (AFFF) on-line hyphenated to Dynamic Light Scattering (DLS) and off-line to Inductively Coupled Plasma Mass Spectrometry (ICP-MS) were used to provide complementary information on the samples. Results will be critically presented in light of their applicability to the current legislative situation.

3.3. Materials and Methods

Chemicals and Samples Description

Two commercial product ingredients were analysed in this work: the first was a colorant indicated as Pigment White 6, titanium dioxide (CAS#13463-67-7) and sold for cosmetics application (from here on will be referred to as pigment white 6). The second was a titanium dioxide based ingredient intended as colorant for food (from now on addressed as E171) whose label declared it to contain as ingredients: E171, sucrose and maize starch. HCl and

NaOH used were from Sigma Aldrich. Water was supplied from a Millipore Advantage System (Merck Millipore, © Merck KGaA, Darmstadt, Germany). 0.02% Novachem ((Postnova Analytics, Germany) in ultrapure water was used as eluent for the AF4 with the eluent being ultrasonically degassed 10 minutes before use. To produce reference spectra for the Raman spectroscopy, anatase nanopowder from Sigma Aldrich and rutile from Kronos (© KRONOS Worldwide, Inc., Dallas, TX, United States) were used. Stock solutions for ICP-MS standard preparation were made from titanium at 1000 mg/L in H_2O/0.24% F- (SpeX Certi-Prep, Assurance) and scandium in 2% nitric acid (Absolute, Inc.).

3.3.1 Ultrasonication

A Vial Tweeter (Hielsher) type sonicator was used to effectively disperse powder into homogenous suspensions. The use of conventional probe sonication was avoided as direct contact between the tip and the sample solution has been found to be a possible source of particle or titanium contamination. The vial tweeter was used at 0.5 on-off cycle time and 75% power (amplitude) on 1 mL volumes in Eppendorf tubes.

3.3.2 Zeta-potential and pH

Zeta-potential was measured using a Zetasizer Nano-ZS instrument (Malvern Instruments Ltd, UK) with temperature control (25 ºC) and recorded in a DTS1060C disposable cell with an equilibration time of 120 sec. Forty runs per sample were acquired. Z-potential was measured in triplicate; measured electrophoretic mobilities were converted into Z-potential using Smoluchowski's formula within the instrument software. A Smulochowski model with a F(Ka) of 1.5 was used. pH was measured before Z-potential measurement.

3.3.3 Particle Size Distribution by CLS analysis

A Disc Centrifuge (CLS) model DC24000UHR (CPS Instruments, EU) was used to size the dispersed particles. The instrument was operated at a disc rotation speed of 22000 rpm using an aqueous sucrose gradient (8%-24% w/w) capped with dodecane and calibrated before each measurement using an aqueous reference solution of polyvinil chloride (PVC) spheres of

known diameter. Gradient quality was daily checked by running 40 nm citrate stabilized silver nanoparticles as in house quality check.

3.3.4 AF4, DLS and off-line ICP-MS

An Asymmetric Flow-Field Flow Fractionation instrument (AF2000 MT Multiflow FFF, (Postnova Analytics, Germany) was used for size fractionation. A 350 µm channel-spacer was used (Postnova Analytics, Germany, Part No. Z-AF4-SPA-V-355). The carrier liquid was high purity water containing 0.02% vol of Novachem surfactant mix. The injection volume was 20 µL. An injection flow of 0.2 mL/min for 4 minutes was used; focus flow was 1.3 mL/min; the applied starting cross flow was 0.5 mL/min, with a linear decay to 0 mL/min in 30 minutes being applied. Detector flow was 1 mL/min. This elution method was derived from the literature from an optimized method for food and cosmetic titanium dioxide particles [13]. A polyethersulfone (PES) membrane with 10 kDa MWCO was used instead of the Regenerated Cellulose in our study (Postnova AF2000 MF z-AF4-MEM-611-10, lot CF090512-214814). AF4 channel was coupled to a UV-VIS detector set at λ=300 nm (Postnova SPD-20AV). The liquid flow exiting the column was split between a DLS quartz flow cell (ZEN0023) and a fraction collector.

Fractions (2 min/fraction) were collected in 2 mL plastic Eppendorf tubes, starting from minute 15. Collected fractions were analysed by an Agilent ICP-MS 7700x (Agilent Technologies, Santa Clara, USA) equipped with platinum sampling and skimmer cones, MicroMist quartz nebulizer and a quartz Scott spray chamber ICP-MS. An octopole reaction system (ORS) was used to reduce interferences on titanium, and He was used as collision gas at a flow of 4.3 mL/min on an octopole collision cell; ICP-MS standards were prepared in Novachem 0.02% to match matrix at the following concentrations of titanium 0, 0.1, 1, 10, 100 and 200 µg/L. Scandium was used as an internal standard (ISTD) at a concentration of 500 ppb in 1% nitric acid and it was added on line with a T piece before sample introduction into the nebulizer. Monitored signals included masses 46, 47, 48 and 49 for titanium and 45 for scandium. ICP-MS was operated in spectrum mode with 5 replicates per sample and 3 points peak pattern with 100 sweeps. Integration time was 0.99 for scandium and 0.09 sec for titanium isotopes. Isotope 47 in gas mode using He as a collision gas, was used for quantification.

3.3.5 Preparation of samples for TEM analysis

Samples of 1 mg/mL concentration were sonicated 15 minutes with a vial tweeter sonicator to avoid any possible contamination that could happen with a probe sonicator. A drop of sample was then added to positively charged grid made of silicon dioxide (Smart Grid, Nano plus grids NG01-051A, Dune Sciences Inc., USA) using an inverted grid-on-drop strategy in order to minimize aggregation artefacts during the drying process. In practice, the positively charged grid was placed on top of a 20 µL droplet of sample and incubated for 10 minutes. The excess of sample was removed by successive washing with MilliQ water. Water excess was carefully wiped with a tissue and grids were left to air-dry before analysis. Images were acquired using a JEOL JEM 2100 TEM microscope at 200 KeV.

3.3.6 Raman Spectroscopy

Raman analysis of the powder samples was performed without any pre-treatment, using a WiTec alpha300 confocal Raman microscope operating with a 532 nm laser source. Average spectra were generated by applying 10 times 0.1 s collection time and are presented without either smoothing or baseline subtraction.
Results and Discussion

3.4. Results and discussion

3.4.1 Fast screening method for optimization of sample preparation

Centrifugal liquid sedimentation (CLS) is a sedimentation technique able to provide particle size distribution (PSD) for particles in a 20-500 nm size range. It is based on the fact that most of the nanoparticles have a higher density from the liquid in which they are suspended and consequently a centrifugal force will tend to make them sediment [14]. Among centrifugation based techniques an alternative to CLS might have been represented by Analytical Ultracentrifugation (AUC), that allows the achievement of higher centrifugal force (>100,000g) that results in a quicker sedimentation time [15] nevertheless the higher price of

this instrumentation makes it less accessible and therefore less useful as a quick and cheap general screening technique. In CLS the suspending liquid is represented by a gradient of sucrose and the centrifugal force is induced by the acceleration of a rotor that tends to move the particles through a disc. The injection point of the sample is positioned in the centre of the rotating disc. Once particles are injected into the rotating gradient, they are subjected to a number of forces: i) the *sedimentation force* that drives the particles towards the edge of the rotating disk, which is proportional to particle mass. ii) *buoyant force* (governed by the Archimedes' principle) and the iii) *frictional force* generated by the movement of the particles through the solvent and will act in opposite direction to the centrifugal force, impeding sedimentation. In few microseconds the three mentioned forces come into balance and the nanoparticle achieves terminal velocity that is related to particle size and density. The velocity of the particle is measured and the Stokes equation is used to calculate the particle diameter given the assumption of a known density and spherical geometry [16].

The instrument is calibrated using a known size calibration standard before each test. The concentration of particles at each size is determined by instantaneously measuring the turbidity of the fluid near the outside edge of the rotating disc using a laser light source (λ=405 nm). The conversion of instantaneous light attenuation into a corresponding mass of particles is done by treating the raw light attenuation data with a series of conversion factors taken from a pre-calculated data set referred to as the Qnet function by the instrument manufacturer. The Qnet function is described as being the effective light scattering cross section of a particle compared to its physical cross section and is calculated by the instrument software using a model based on the Mie theory of light scattering.

To test the possibility to analyse the two samples by mean of CLS, a mother stock (0.5% w/v stock) of each of the material was prepared in water, by sonication. In both cases visual examination showed them to be easily dispersible in water. To ensure homogeneous sub-sampling all stock solutions were vortexed thoroughly immediately before aliquoting to produce sub-samples for dilution. To determine suitable injection concentration for CLS analysis of the E171 a range of dilutions (1:10, 1:100, 1:1000) from the mother stock were analysed using a standard sample volume of 100 µL. It was verified that the peak position was independent of sample concentration in the tested range confirming the absence of streaming effects due to overloading of sample. After evaluation of these data a concentration of 0.05 mg/mL (0.005% w/v) was selected as being the most suitable for further analysis on CLS. To test the effect of sonication, a samples of E171 (0.005% w/v) dispersed with increasing sonication time on a vial-tweeter (0.5 cycle 70% power) were analysed by CLS. Results are

presented in Figure 2.A. An increase of sonication time (keeping all other parameters constant) resulted into a gradual change of the weight based particle size distribution with the peak maximum shifting from about 360 nm down to 320 nm (from 0 up to 15 minutes of sonication). The shift of the peak maximum of the PSD with the increase of the sonication time is the likely result of a gradual break-up of large TiO_2 agglomerates into small agglomerates possibly with the release of individual primary particles. Once the sample concentration and sonication time was selected (15 minutes vial tweeter sonication and concentration of 0.05 mg/mL) both samples, E171 and colorant white 6, were prepared and further analysed under the same conditions.

Figure 1.B shows the CLS data for both samples, following a 15 minute vial-tweeter sonication. While both products have a wide PSD, E171 has a larger mean size than the other. Furthermore CLS shows negligible amount of particles below 100 nm even after 15 minutes of sonication (Figure 1.B).

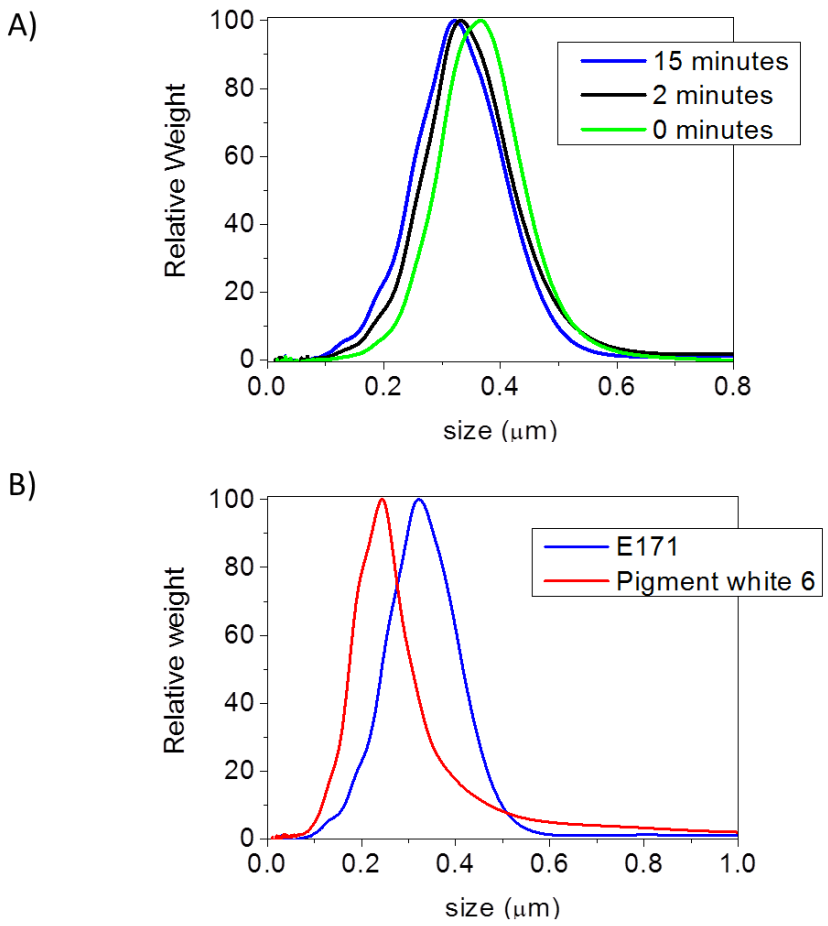

Figure 1. A) the effect of the dispersion procedure on E171 based product: an increase in sonication time causes a reduction of peak maximum for the weight based PSD measured on

CLS; B) a comparison of weight based PSD measured on CLS for pigment white 6 (red line) and E171 based product (blue line) at a concentration of 0.05 mg/mL of powder, sonicated for 15 minutes.

Dispersions in water of both samples were also measured at different pH, for which both Zeta-potential and PSD by CLS were determined. Initial pH (0.005% w/v %, after 15 minutes sonication) was found to be 5.5 and 5.9 for E171 and pigment white 6 respectively. The pH of sample was modified by adding concentrate acid (HCl) or base (NaOH), a small aliquot of sample was taken at given values of pH, sonicated for 15 minutes and measured. Figure 2 shows the Z-potential and CLS data. The data show that for both samples at pH higher than 5 the Z-potential is strongly negative, while it is much less negative for pH < 4. The less negative Z-potential values in strong acidic conditions cause instability of the suspension leading to particle aggregation and agglomeration as indicated by the increase of the mean value of PSD.

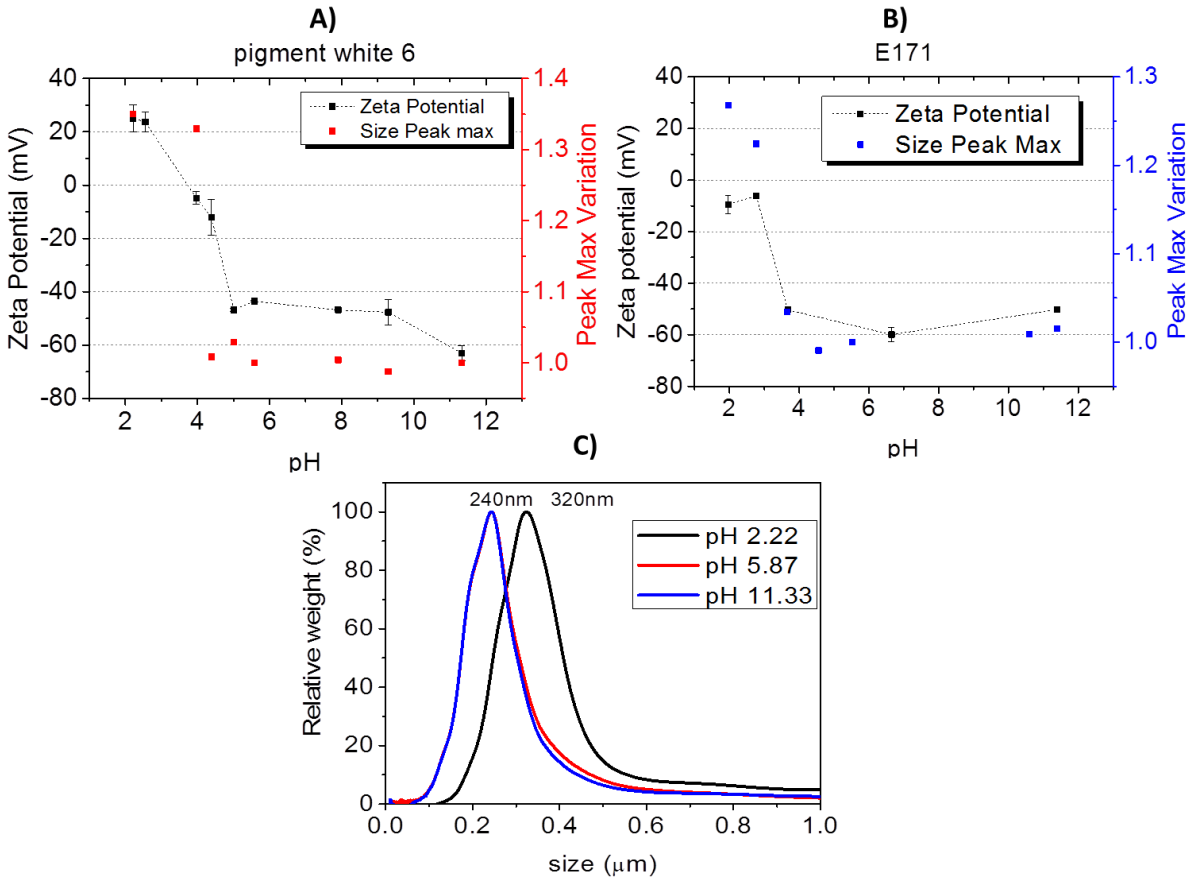

Figure 2. Zeta-potential and relative size (determined by CLS) variations for pigment white 6 (A) and E171 based product (B) at different pH. Peak max variation is intended as the ratio

between the initial size determined by CLS at native pH UPW (exactly 243nm at pH 5.58. For pigment white 6, and 321nm at pH 5.53 for E171) and the size detected by CLS upon pH modification. Complete PSD of pigment white 6, determined by CLS, at three different pH values (C). All measurements were performed at 0.005% wt /vol, after 15 minutes tweet sonication.

CLS data could also provide a more quantitative sizing of the analysed samples but the determination of the accurate particle size distribution requires the knowledge of the density and geometry of the actual particles present in the sample. In general, the samples under analysis could form aggregates, have non-spherical forms, have different crystalline forms or be coated with different molecules. All these factors could affect the density of the material and thus give inaccurate values of the PSD determined by CLS. As shown in the Raman spectroscopy analysis paragraph, both analytes were mainly composed by the anatase form, allowing one possible source of error to be removed. This knowledge allowed the correction of the density to the one of anatase (3.78 g/cm^3) instead of the rutile one (4.23 g/cm^3) as a first approximation for the actual density of the material. The use of the rutile density in the evaluation of CLS data for two samples would have resulted in a PSD with significantly lower mode diameters than those shown in figure 1.B.

The uncertainties due to the variable densities of aggregates (or functionalization of the particle surface or the presence of residues from the matrix, such as starch) is even more complex and can be only partially addressed by combining CLS measurements with other techniques that can provide an independent measure of the size of particles, such as AF4/DLS.

3.4.2 General Methods for Assessing Particle Size Distribution

While the analysis performed by CLS is valuable for performing a general screening of the two selected products, it is a non-specific method which cannot distinguish the type of particle being detected. In the case where it is necessary to simultaneously determine size and chemical nature of a material in dispersion an option is to use hyphenated confirmatory methods such as Field Flow Fractionation-DLS with additional off-line ICP-MS [17]. Among the broader family of Field Flow Fractionation techniques suitable the two most widely applied for nanoparticles separation are represented by Asymmetric Flow-Field Flow

Fractionation (AF4) and Sedimentation-Field Flow Fractionation (Sd-FFF), both Sd-FFF and AF4 were able to accurately size AgNP in the range 20−100 nm and deal with polydispersed samples [18]; AF4 has generally a smaller running time than Sd-FFF and was therefore preferred for the purpose of this study.

Dispersions of pigment white 6 and E171 products were prepared by dilution from fresh stock suspensions, sonicated 15 minutes according to conditions described before and immediately injected into the AF4/UV-Vis/DLS system. This set-up has the advantage of allowing the fractionation of particles by size, the UV-Vis detector (at 300 nm) allows a relatively quick and inexpensive (yet unspecific) detection of particles, while DLS allows on-line sizing of the fractionated samples [15]. The application of an on-line sizing technique is highly recommended over either channel retention time vs. size calibration or solely retention theory of Field Flow Fractionation systems to check the quality of separation and to ensure the absence of deviations from expected retention times due to the presence of matrix in real-case samples [19]. Finally, to add specificity to the system, key fractions were collected and further analysed by batch ICP-MS to confirm and quantify the titanium content. This approach opens a number of options to laboratories that do not have an in-house ICP-MS facility, since fractions can be collected and transported to the final analysis place, once their stability in dispersion is proved.

The AF4 elution profile, as described in the method section, was derived on slight modification from literature [13]. The chosen eluent (Novachem 0.02%) has a pH of about 7.5 and should therefore not result into particle agglomeration/aggregation. Collated results from all the detectors (UV-Vis, DLS and ICP-MS) are presented in Figure 4: for both products, the elution of fractionated particles started at around 15 minutes, as detectable on UV-Vis detector signal (black line) and from the ICP-MS determined content of Ti found in the specific fractions (green triangles). The inclusion of the DLS in the hyphenated system allowed on-line measurement of the hydrodynamic diameter of the particles as they exit the separation channel. This approach appeared to be most reliable choice for particle sizing since channel calibration with particles of the same chemical nature of the analyte was not possible due to the lack of suitable reference materials. DLS data where filtered based on their count rate intensity eliminating points having a too low S/N ratio. DLS data after fractionation show a peak maximum at about 400 nm for E171 and 230 nm for pigment white 6. In both cases AF4/DLS/ICP-MS have produced very broad distributions that are compatible with the presence of large agglomerates/aggregates of titanium dioxide as indicated from CLS data (Figure 2). As already remarked, CLS is not able to identify the chemical composition of the

particles and therefore a more tailored approach was needed to verify the particles as being TiO_2. ICP-MS chemical analysis of the fractions collected from the main eluted peak produced a profile of the titanium content (green triangles in Figure 3). The content of titanium in the fractions is visibly following the peak elution confirming that the particles are TiO_2. As already mentioned, the bigger particles are probably aggregates and agglomerates, possibly characterized by having poorly defined non-spherical shapes. This variability in shape will impact negatively on the elution behaviour in AF4, the size determination with DLS and the mass to number conversion based on ICP-MS titanium content which requires calculations based on reliable assumptions about particle density and shape. Considering the possible level of error introduced by these limitations, it was not considered relevant to attempt to transform any of the presented data to number-based PSD. Titanium recovery was 52% for E171 and 63% for pigment white 6 determined by comparing the titanium content found in the injected volume to the sum of all collected fractions by mean of ICP-MS. Both the AF4 fractions and as-dispersed samples were treated in the same way, therefore any possible artefact due to sample preparation (including incomplete ionization in the plasma) should be cancelled in this relative estimation; therefore a possible reason for this incomplete recovery is amenable to a large loss of un-fractionated material in the void peak and/or loss on the membrane during separation. It is evident from the fractrogram that in both cases, a significant void peak is present at about 5 minutes.

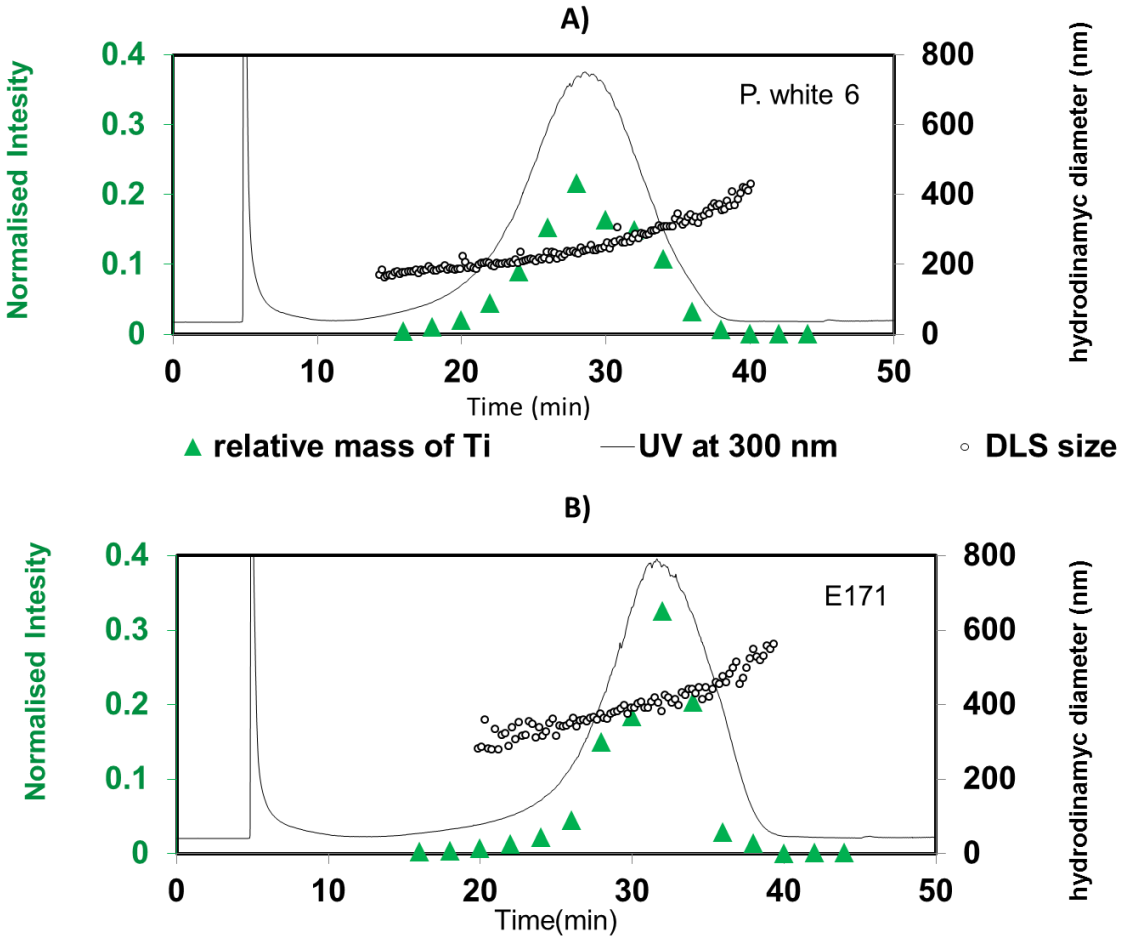

Figure 3. AF4 fractionation of pigment white 6 (A) and E171 (B): black line represents UV-Vis signal acquired at 300 nm, normalized by its maximum intensity (refereed to the left axes), green triangles are based on titanium ICP-MS off-line analysis of key fractions and indicate the relative mass normalized to the sum of total mass in the fractions (referred to the left axes), circles are related to right axes and represent the hydrodynamic diameter measured by on-line DLS detector.

TEM micrographs (Figure 4) show that both pigment white 6 and E171 are composed of both smaller single particles (of diameters mainly in the 100 nm size range) and larger aggregates. Two of these aggregates are shown in Figures 4.B and 4.D, for pigment white and E171, respectively. The data suggest that many of the apparently larger particles (>200 nm) detected by the non-specific DLS are in fact aggregates composed of tightly bound smaller particles. TEM data, especially regarding aggregates/agglomerates inspection, can be misleading due to formation of artefact during drying process. However the preparative technique used in this study, based on the inverted grid-on-a-drop strategy, is expected to diminish the possible formation of artefacts. In fact, the NP attachment to the grid is mainly based on charge

interaction and the excess of sample is washed away before drying. The use of positively charged grids placed above the sample for a short contact time, promotes a homogeneous binding of the particles.

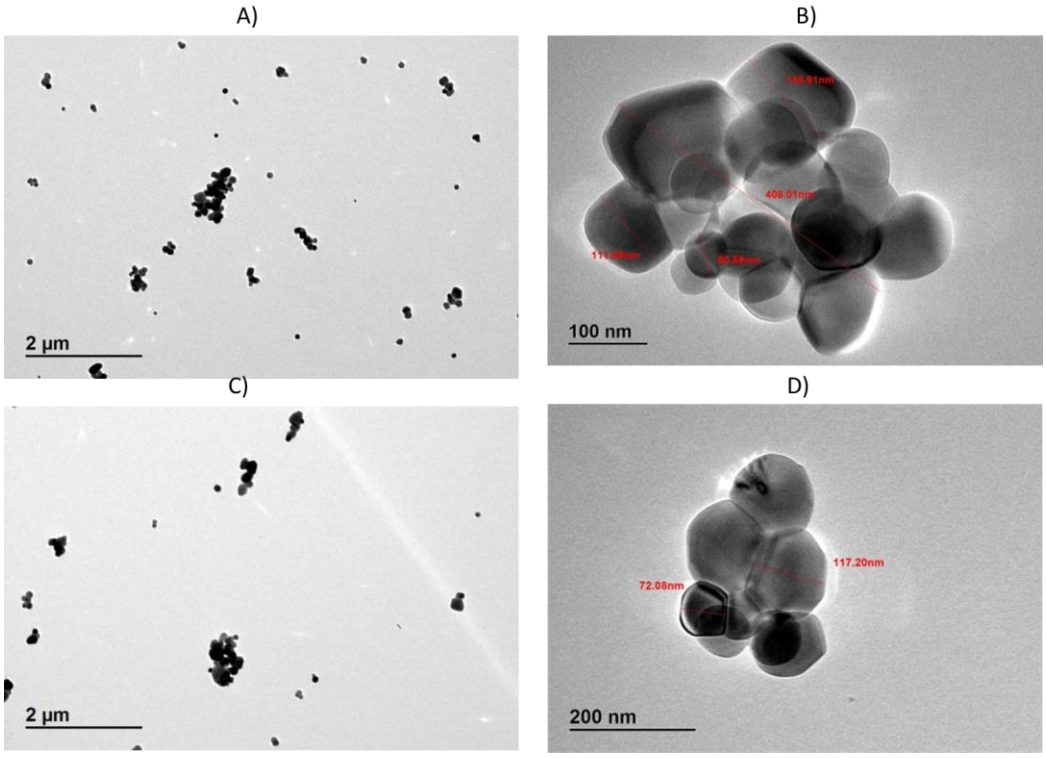

Figure 4. TEM micrographs of E171 (A and B) and pigment white 6 (C and D).

3.4.3 Combining CLS and AF4/DLS data

The separation of particles in CLS is a function of size, shape, and density and the determination of PSD in CLS critically depends on the exact knowledge of these parameters. By combining the size information obtained by AF4/DLS with the CLS data it is possible to obtain the apparent density of the samples and of the eventual aggregates present. Comparing the AF4/DLS size of 400 nm for E171 with the CLS mode diameter of 350 nm (obtained using the anatase density) indicates that the effective density of E171 particles is smaller than 3.78 g/cm3 with a density value of around 3.5 g/cm3 being a more realistic estimate. This reduced density could be due to either the presence of organic coating of the TiO_2 particles (starch) or to a fractal dimension of the aggregates smaller than 3. In fact, the coalescence

fractal sphere model (Sterling et al., 2005) predicts a lower density of aggregates for fractal dimensions smaller than 3. In contrast, for pigment white 6 the diameter obtained from CLS and AF4/DLS are very close (250 nm and 230 nm, respectively) suggesting that the density used in the CLS analysis is appropriate.

3.4.4 Assessment of crystalline state with Raman spectroscopy

Raman spectroscopy is a non-destructive technique that allows fast analysis of real samples, including titania, in complex matrices using extremely low sample volumes. In the case of titania, Raman spectroscopy allows detecting the chemical nature and crystalline structure directly on powders [20] and it has been successfully applied to the analysis of titania nanoparticles [21]. The identification of titania crystal structure is important in order to apply the correct physical characteristics (density, refractive index) of the particles in methods (like CLS) that require calculations based on these parameters. Moreover, titanium oxide particles with different crystal structure show different catalytic activity and biological interactions (through generation of free radicals). Anatase has higher photocatalytic activity [22] and usually higher degree of surface hydroxylation than rutile. Thus, evaluation of the crystal form provides additional information about the possible behaviour in a biological system contributing to the risk assessment [23].

Figure 5 shows the Raman spectra of pigment white 6 and E171, together with Raman spectra of rutile and anatase reference materials. The typical spectral fingerprint of anatase (peaks at 145, 399, 516, 639 cm^{-1} Raman shift) can be clearly recognized in both products and the anatase reference sample. No trace of rutile (bottom line) or of organic components (typically expected to appear in the 2800-3000 cm^{-1} Raman shift range at the C-H stretching vibration region) was detected. The unequivocal identification of the crystalline form for the two products as anatase allows an assignment of appropriate density values for use in the CLS analysis of the uncoated, primary particles, at 3.78 g/cm^3 (as opposed to 4.23 g/cm^3 for rutile).

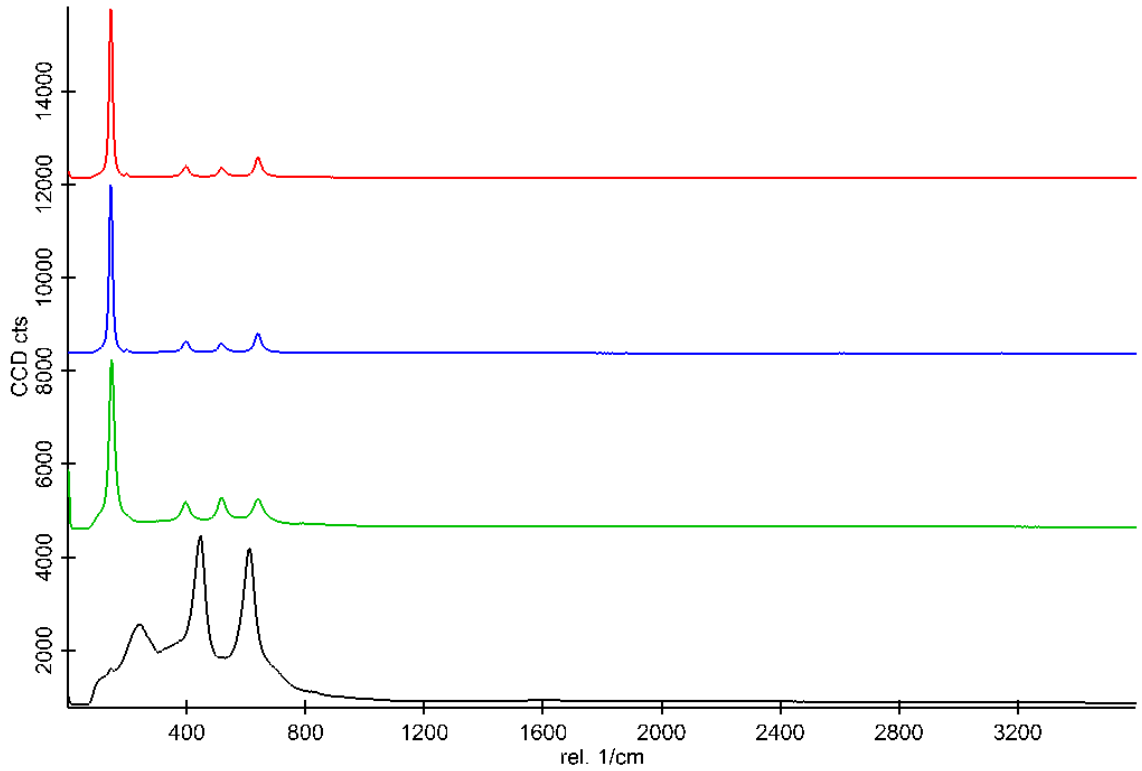

Figure 5. Raman spectra (from top to bottom) of pigment white 6 (red line), E171 product (blue line), anatase reference from Sigma Aldrich (green line) and rutile reference Kronos (black line) demonstrates that both products are based on anatase form of titanium dioxide.

3.5. Conclusions

In this study two commercially available titanium dioxide products used in the food and cosmetic sectors were analysed with a pool of complementary techniques.

The set of techniques used in this study provide a general strategy for determination of the PSD of titanium dioxide products. Simpler and quicker screening techniques, such as CLS, can be used to screen and optimize sample preparation protocols. Vial sonication was used for sample preparation with the median value of the mass-based PSD being found to decrease with increasing sonication time up to 15 minutes. In particular, CLS was shown to be a simple and useful (although non-specific) screening technique for rapidly screening the influence of changes (such as pH and sonication time) in sample preparation protocols. CLS revealed, for both products, a wide particle size distribution having a peak maximum at over 200 nm. Both titanium dioxide products showed a negative Z-potential when dispersed in water. Upon sonication at acidic pH, detectable particle size increased along with increasing Z-potential,

towards 0 mV. More complex methods (AF4 with multi-detectors and TEM) provide confirmatory methods with more detailed PSD, while "identity" techniques, such as Raman and ICP-MS, gave the unequivocal evidence on the crystalline phase and presence of titania in the samples. The more complex AF4 with on-line DLS and off-line ICP-MS allowed in fact the identification of titanium dioxide particles with a particle size distribution comparable to that obtained by CLS. The evidence provided by TEM micrographs suggest the presence of particles in the 100 nm size range and of larger aggregates in the 200 nm to 300 nm size range formed by smaller primary particles. Both E171 and pigment white 6 were confirmed to be based on anatase according to Raman spectroscopy, thus giving direct evidence of both chemical identity and crystalline phase of the samples under investigation. In addition, the combination of data from CLS and AF4/DLS gives indication on both the size and density of the aggregates present in the samples.

These results highlight the difficulties in determining the PSD of titanium dioxide in complex matrices and in particular the challenges associated in detecting the size of primary particles in the presence of strongly bound aggregates. The results also show how a combination of techniques and a tiered experimental approach can be applied in addressing this challenging problem.

Acknowledgements

The work leading to these results has received funding from the FP7 program of the European Union under the SMARTNANO consortium (contract number FP7-NMP-2011-SME-5-280779).

3.6. References

1. Gázquez, M.J., et al., *A Review of the Production Cycle of Titanium Dioxide Pigment.* Materials Sciences and Applications, 2014. **5**: p. 441-458.
2. Taskaya, L., Y.-C. Chen, and J. Jaczynski, *Color improvement by titanium dioxide and its effect on gelation and texture of proteins recovered from whole fish using isoelectric solubilization/precipitation.* LWT - Food Science and Technology, 2010. **43**(3): p. 401-408.

3. Weir, A., et al., *Titanium dioxide nanoparticles in food and personal care products.* Environmental Science and Technology, 2012. **46**(4): p. 2242-2250.
4. Peters, R.J.B., et al., *Characterization of titanium dioxide nanoparticles in food products: Analytical methods to define nanoparticles.* Journal of Agricultural and Food Chemistry, 2014. **62**(27): p. 6285-6293.
5. Butler, M.K., et al., *High-pressure freezing/freeze substitution and transmission electron microscopy for characterization of metal oxide nanoparticles within sunscreens.* Nanomedicine, 2012. **7**(4): p. 541-551.
6. Australian Government TGA, *Literature review on the safety of titanium dioxide and zinc oxide nanoparticles in sunscreens*. 2013, Australian Government.
7. Schilling, K., et al., *Human safety review of "nano" titanium dioxide and zinc oxide.* Photochemical & Photobiological Sciences, 2010. **9**(4): p. 495-509.
8. Wilson Centre. *www.nanoproject.org*. [cited 2015 25-03-2015]; Available from: http://www.nanotechproject.org/cpi/search-products/?title=&asmSelect0=&date_created=&date_modified=&nanomaterials%5B%5D=1167&search-products_submit=Search&_submitKey=16%3Asearch-products%3A0.
9. *Regulation (EU) No 1169/2011*, in Official Journal of the European Commission.
10. Linsinger, T., et al., *JRC Reference Report Requirements on measurements for the implementation of the European Commission definition of the term 'nanomaterial'*. 2012, JRC.
11. Cascio, C., et al., *Detection, quantification and derivation of number size distribution of silver nanoparticles in antimicrobial consumer products.* Journal of Analytical Atomic Spectrometry, 2015.
12. Wagner, S., et al., *First steps towards a generic sample preparation scheme for inorganic engineered nanoparticles in a complex matrix for detection, characterization, and quantification by asymmetric flow-field flow fractionation coupled to multi-angle light scattering and ICP-MS.* Journal of Analytical Atomic Spectrometry, 2015.
13. López-Heras, I., Y. Madrid, and C. Cámara, *Prospects and difficulties in TiO2 nanoparticles analysis in cosmetic and food products using asymmetrical flow field-flow fractionation hyphenated to inductively coupled plasma mass spectrometry.* Talanta, 2014. **124**(0): p. 71-78.

14. Kamack, H., *Particle-Size Determination by Centrifugal Pipet Sedimentation.* Analytical Chemistry, 1951. **23**(6): p. 844-850.
15. Calzolai, L., D. Gilliland, and F. Rossi, *Measuring nanoparticles size distribution in food and consumer products: A review.* Food Additives and Contaminants - Part A Chemistry, Analysis, Control, Exposure and Risk Assessment, 2012. **29**(8): p. 1183-1193.
16. ISO, *ISO 13318-2:2001* in *Determination of particle size distribution by centrifugal liquid sedimentation – Part 2: photocentrifuge method*. 2001, International Organization for Standardization: Geneva, Switzerland.
17. Bednar, A.J., et al., *Comparison of on-line detectors for field flow fractionation analysis of nanomaterials.* Talanta, 2013. **104**(0): p. 140-148.
18. Cascio, C., et al., *Critical experimental evaluation of key methods to detect, size and quantify nanoparticulate silver.* Analytical Chemistry, 2014. **86**(24): p. 12143-12151.
19. Dubascoux, S., et al., *Optimisation of asymmetrical flow field flow fractionation for environmental nanoparticles separation.* Journal of Chromatography A, 2008. **1206**(2): p. 160-165.
20. Bear, J.C., et al., *Anatase/rutile bi-phasic titanium dioxide nanoparticles for photocatalytic applications enhanced by nitrogen doping and platinum nano-islands.* Journal of Colloid and Interface Science, 2015. **460**: p. 29-35.
21. Choi, H.C., Y.M. Jung, and S.B. Kim, *Size effects in the Raman spectra of TiO2 nanoparticles.* Vibrational Spectroscopy, 2005. **37**(1): p. 33-38.
22. Sclafani, A. and J.M. Herrmann, *Comparison of the Photoelectronic and Photocatalytic Activities of Various Anatase and Rutile Forms of Titania in Pure Liquid Organic Phases and in Aqueous Solutions.* The Journal of Physical Chemistry, 1996. **100**(32): p. 13655-13661.
23. Sayes, C.M., et al., *Correlating Nanoscale Titania Structure with Toxicity: A Cytotoxicity and Inflammatory Response Study with Human Dermal Fibroblasts and Human Lung Epithelial Cells.* Toxicological Sciences, 2006. **92**(1): p. 174-185.

4. Chapter II

Detection, Sizing, and Quantification of Titanium Dioxide Nanoparticles in Sunscreens using flow field flow fractionation coupled with DLS and ICP-MS detection

Claudia Cascio [a], Diana Antonio [b], Meital Portugal [c], Douglas Gilliland [b], Luigi Calzolai [b]

[a] formerly, European Commission - Joint Research Centre, Via E. Fermi 2749, 21027 Ispra (VA), Italy

[b] European Commission - Joint Research Centre, Via E. Fermi 2749, 21027 Ispra (VA), Italy

[c] AHAVA Dead Sea Laboratories, 1 Arava Street, 70150 Lod, Israel

Under preparation for publication

4.1. Abstract

Titanium dioxide (TiO_2) nanoparticles are extensively used in commercial sunscreen lotions due to their properties of absorption of UV light and being relatively transparent in the visible light region. By combing a size separation technique (based on FFF) with a titanium specific quantification (based on ICP-MS) and size measurement (based on dynamic light scattering) we were able to measure the amount of titanium dioxide NP present in sunscreens. Our technique is flexible enough in making use either of direct coupling of FFF with ICP-MS, or by analysing FFF fraction in off-line mode. Our results show that the coupling of FFF with ICP-MS (and DLS) allows determining the nanoparticle size distribution in difficult matrices such as sunscreen lotions. This approach shows promising in light of the EU legislation for cosmetics which requires in the labelling of nanomaterials, i.e. particles in the size range of 1 to 100 nm.

4.2. Introduction

Nanotechnology-based products are increasingly being available to consumers in different application areas, ranging from paint and inks to food and medicines. In particular, titanium dioxide nanoparticles are used as additives in cement and paints to increase self-cleaning properties and in the cosmetics sector as ingredients able to block UVa and UVb radiation, while being transparent in the visible region.
As a consequence sunscreen lotions that use titanium dioxide nanoparticles as UV blocker are less whitish than those using bulk titanium dioxide and they seem to be preferred by consumers: titanium dioxide nanoparticles have thus found widespread use in the cosmetic sector [1].

The detection and quantification of nanoparticles is a complex issue due to the need to combine "classical" identification and quantification of the constituent material, with the accurate determination of the size of sub-micrometer objects, usually well below the optical diffraction limit. This task is rendered even more difficult when measuring engineered nanoparticles embedded in complex matrices (such as cosmetic sunscreens) that contains several other ingredients and could potentially contain also natural occurring nanoparticles.
Nanotechnology-based products (and especially industry-based materials) usually contain nanosized objects with a wide heterogeneity of sizes and for their proper characterization it is necessary to measure the complete particle size distribution in the complex matrix. One of the opening issues in the field is related to the most relevant metrics that should be used to assess the effect of nanomaterials on biological systems and the environment. In this respect a quite common opinion is emerging that one of the main drivers of the interaction/toxicity is the total surface area [2, 3]. Thus, to be able to address this point the number size distribution of the particles is the most relevant property that should be determined. In the European Union the determination of the number particle size distribution is the main property that should be determined in order to classify a material as nanomaterial. This recommended definition of what constitute a nanomaterial is finding its way in the legislative process and, for example, has become mandatory in the case of cosmetic to report its presence in the product ingredients list as of June 2013 (EC Regulation 1223/2009 - Cosmetics Directive [4]). At the moment no single technique is able to provide an accurate nanoparticle size distribution, especially in complex matrices. In particular asymmetric flow field flow fractionation (AF4) is able to separate objects in the 1-300 nm size range, but usually it lacks the ability to specifically quantify the presence of inorganic materials at very low detection levels. Detection is done by UV which in the case of titania is based on an unspecific range (see figure S1). In this respect

ICP-MS provides a very high specificity and sensitivity to accurately measure titanium content.

AF4 can be used to also determine the size of nanoparticles based on the exit time from the separation channel, but it requires the use of calibrants and it assumes that no interaction with the semipermeable membrane takes place [5]. Dynamic light scattering (DLS) can easily measure the size of objects in the 1nm to 1um range without the need of any calibration or calibrating standards, but it is not able to accurately measure the particle size distribution of samples containing particles of different sizes [6]. On the other hand, DLS is very well suited for measuring the size of monodispersed samples, such as those that have been previously size-separated by techniques such as AF4.

In this work by combining AF4 separation with DLS on-line and ICP-MS detection we were able to determine and quantify the particle size distribution of titanium dioxide nanoparticles in a very complex matrix, such as sunscreen lotion.

4.3. Materials and Methods

4.3.1 **Sample preparation**

The sunscreen lotion used in this study was prepared by AHAVA company. To evaluate the effect of the matrix components on the fractionation process, two samples were provided: i) control sample, a lotion lacking UV blockers and ii) P25 sample, a lotion with identical composition with the addition of Aeroxide P25 titania nanoparticles (Evonik Industries). For AF4 analysis, fluidification of the samples is required. Lotions were dispersed in 0.5% TEGO® Care 450 (polyglyceryl-3 methylglucose distearate, Evonik Industries) at a final concentration of 5 mg/mL. Samples were homogenized by tweet sonication during 3 minutes at 70% amplitude and half cycle frequency, immediately before injection.

4.3.2 **Asymmetric Flow Field Fractionation and Dynamic Light Scattering size measurement**

An AF4 system (Postnova Analytics) coupled to UV and DLS detectors was used for particle size separation, detection and size determination, respectively. The elution method used a 280 mm long separation channel, with a 350 µm spacer and a 10 kDa cut off membrane of regenerated cellulose and a 50 µL injection loop were used. A solution of 0.01% Novachem (Postnova Analitics) in water, freshly prepared and degassed each day, was used as carrier. All samples were analysed under the following elution conditions: 0.5 mL/min injection flow; 0.2 mL/min tip flow for 5 min; 1.3 mL/min focus flow; and a linear decrease of the cross flow from 1 to 0 mL/min over 30 minutes followed by 10 minutes of steady flow. The UV detector was set at 250 nm, considering the low specificity of the LSPR titania band. Fractions of 1 mL, representing 2 minutes of elution, were individually collected for ICP-MS analysis (off-line).

4.3.3 **ICP-MS analysis**

An Agilent 7700x ICP-MS system (Agilent Technologies, Santa Clara, USA) equipped with quartz nebulizer and a Scott spray chamber was used for the off-line determination of the content of titanium in collected fractions. The ICP-MS was operated in spectrum mode using a He octopole collision cell. Scandium was used as an internal standard. Key parameters used are shown in table 1. For off-line analysis of eluent fractions by ICP-MS each sample was spiked with a known quantity of scandium as an internal reference standard up to a final scandium concentration of 10µg/L. Calibrated was performed using appropriate ionic titanium standard diluted in the AF4 eluent. A 5 point calibration curve was generated using eluent solution with the addition of titanium standard at the following concentration: 0, 0.1, 1, 10, 100 µg/L. Quantification of the titanium by the ICP-MS was based on the count ratio ^{47}Ti / ^{45}Sc.

Table 1. Parameters used for ICP-MS instrument in He mode.

Parameter	**Details**
RF-Power	1550 w

Reflected- matching	1.80 V
Sample Depth	8 mm
Carrier Gas type	Argon (99,999%)
Carrier Gas	0.85 L/min
Dilution Gas	0.30 L/min
Cell He Flow	4.3 mL/min
Cell Stabilization time	40 sec
Nebuliser type	MicroMist (quartz)
Nebuliser flow rate	0.35 ml/min
Spray Chamber	Scott (quartz)
Scan mode and Resolution	Spectrum mode
Integration Time	0.3 sec
Monitored masses	Titanium (47, 48) Scandium (45)

For the on-line AF4/DLS/CP-MS set-up, the ICP-MS was connected to the AF4/DLS and operated in time resolved acquisition mode. The connection to the ICP-MS was realised after the DLS; the flow was regulated by the AF4 being set-up at 0.5 mL/min. The ICP-MS peristaltic pump was at 0.1 rpm, corresponding to a flow of 0.3 mL/min. The connection was realised via a T-connector that allowed the excess of carrier to go to waste. The peristaltic flow was monitored using a flow meter during each run. This experimental setup is still not very common and at the moment there is no commercially-available kit for a direct physical connection between the two instruments. To this end we have developed such a connection using off-the-shelf parts. In our setting we are using an additional three-way switching valve after the AF4 separation for the intensity calibration of the on-line ICP/MS detector and an additional reference standard for flow monitoring. Calibration was performed in a spectrum mode by mean of Ti standards in the range 1-100 ng Ti/mL. Scandium was added on line using the ICP-MS peristaltic pump before the nebuliser.

4.3.4 **TEM imaging**

Aliquots of the eluted fractions were reserved for TEM analysis. For confirmation of nanoparticle presence, fractions where a maximum UV signal was detected were spotted in C-Cu grids. Images were acquired using a JEOL JEM 2100 TEM microscope at 200 KeV. TEM images also gave an idea of the particles size and aggregation/agglomeration state.

4.4. Results

4.4.1 **Experimental setup**

Lotions, with and without titania nanoparticles were sequentially analyzed by AF4/DLS/ICP-MS. A first separation step performed in the AF4 instrument allowed the size separation of all sample components while the particle size determination was carried on by DLS in real-time. Finally, the identification and quantification of the particles material was performed by ICP-MS. To compare the performance of the hyphenized quantification system, ICP-MS was used both on- and off-line. The process workflow is schematized in figure 1.

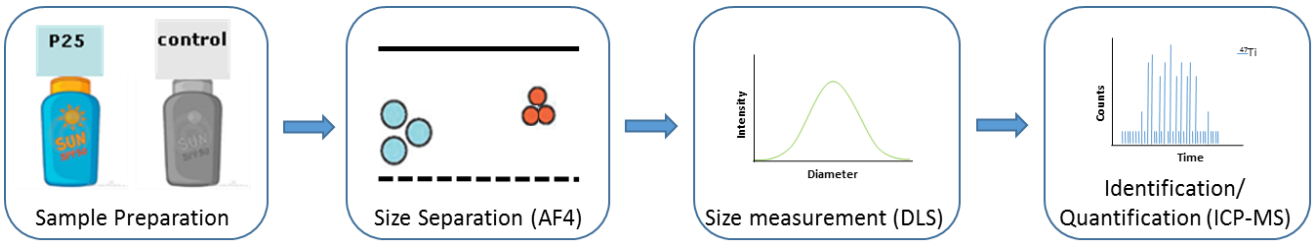

Figure 1. Experimental setup showing the analytical protocol for characterization of nanoparticles in sunscreens. Sequentially, size separation, size measurement and chemical identification/quantification are performed by AF4, DLS and ICP-MS, respectively.

4.4.2 **AF4/DLS size measurement**

P25 samples, were analysed by on-line AF4/UV-Vis/DLS. Figure 2.A represents the UV signal at 250 nm (sensitive to titanium dioxide nanoparticles): it shows an apparently bimodal distribution of the sample exiting the AF4 separation column with absorption peaks at 8 and 16 minutes. Figure 2.B represents the corresponding DLS data, showing the intensity of the signal (counts per second), and the hydrodynamic diameter (Z-average). The data indicate that the sample contain a significant quantity of nanoparticles with a hydrodynamic diameter between 50 and 200 nm. Control samples were analysed using the same protocol (Figure 3). Analysis of both the UV-Vis and the DLS signals, indicate that the measurements with this simple sample preparation are not reproducible

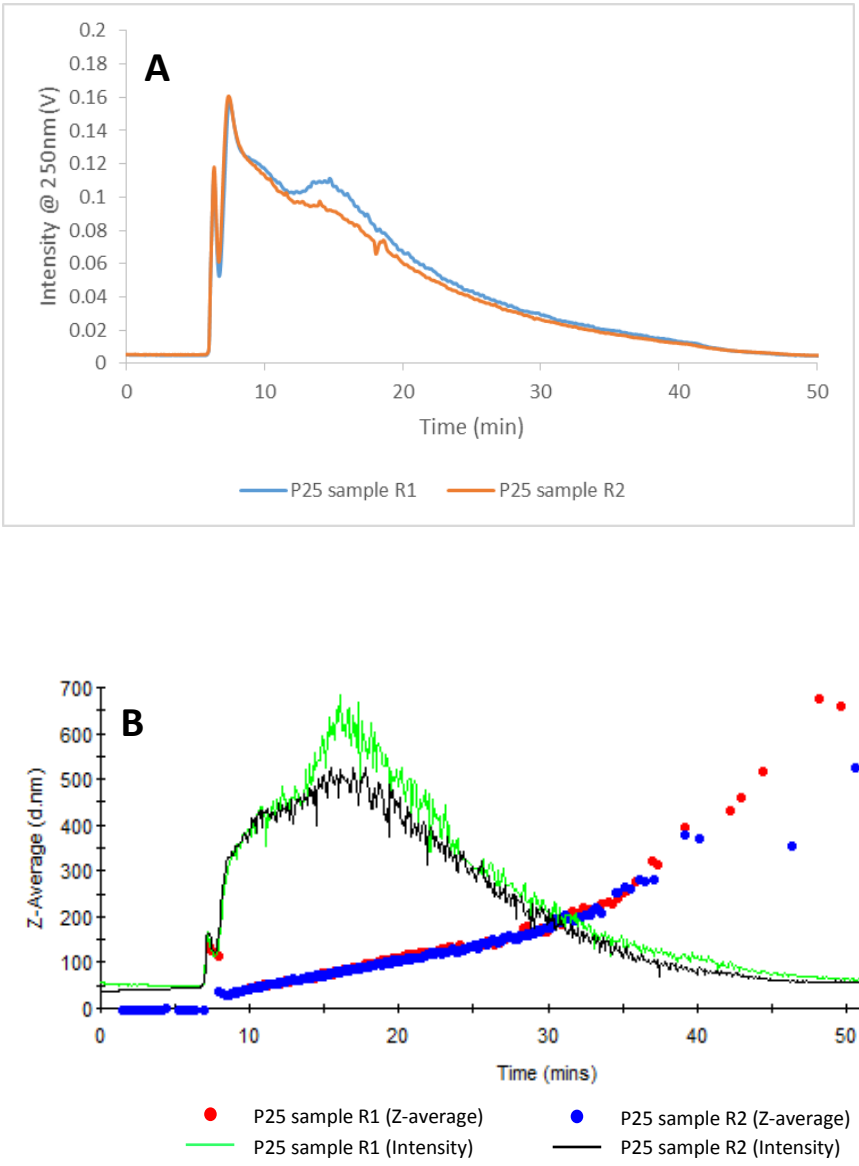

Figure 2. On-line AF4/UV-Vis/DLS analysis of the P25 sample, in duplicate. AF4 elutions were evaluated in real time by A) UV-Vis, showing the adsorption signal recorded at 250nm

and B) DLS, showing the particles diameter (Z-average in nm) and signal intensity (in counts per second).

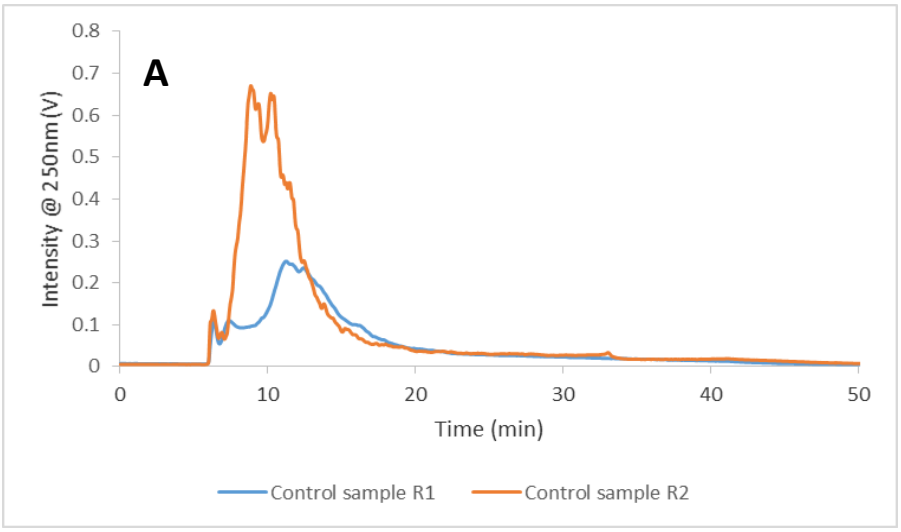

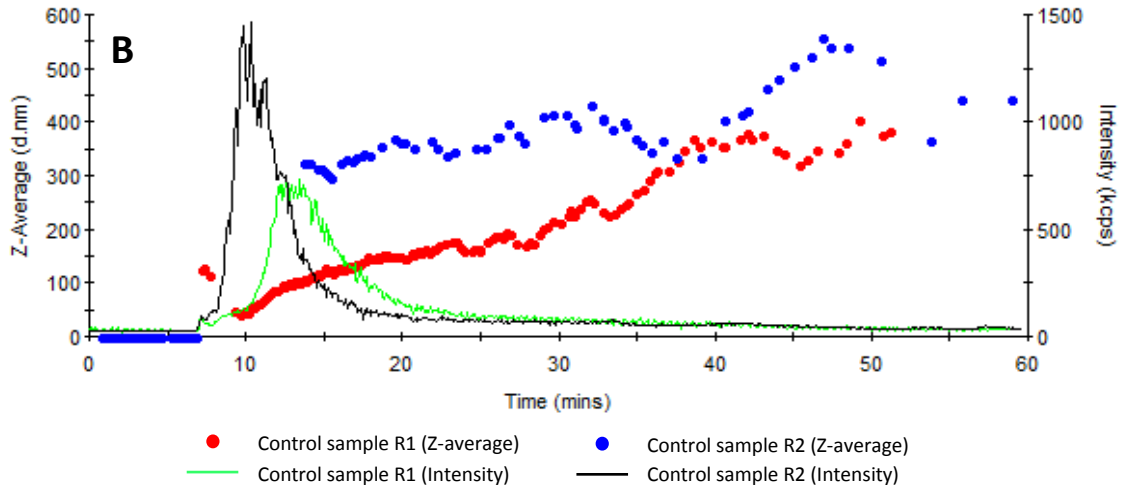

Figure 3. On-line AF4/UV-Vis/DLS analysis of the control sample, in duplicate. AF4 elutions were evaluated in real time by A) UV-Vis, showing the adsorption signal recorded at 250nm and B) DLS, showing the particles diameter (Z-average in nm) and signal intensity (in counts per second).

4.4.3 **Off-line ICP-MS analysis**

Inconclusive AF4/DLS data was checked by additional particle identification and quantification methods. Off-line ICP-MS analysis of the collected fractions, both from control samples and from P25 samples was performed. ICP-MS analysis revealed the presence of titanium in the P25 sample fractions recovered from AF4 (Figure 4.A). Higher content was detected essentially where DLS particle size measurements were consistently more intense. A concentration of around 7µg/L was detected in the spiked sample (P25), while no signal was recorded for the control sample, as expected. The declared concentration of aeroxide P25 in the spiked sample was 1%. Considering that the cream was diluted 800 times before injection and that the NP were eluted with 20mL of solvent, we would expect to detect near 1.25 mg/L. However, the channel recovery was determined to be 53% (data not shown), meaning an expected concentration of 33 µg/L. Even considering the 40% sample loss between DLS and AF4, 19.8 µg/L recovery would be expected. In addition, previous tests showed that ICP-MS analysis of not digested titania NP samples have recoveries in the range of 50% (see "Quantification of total titanium content" section in SI). With such consideration, the detected concentration of 7 µg/L is close to the expected 9.9 µg/L concentration.

A formulation identical to the sunscreen with no titania added (control sample) was also analysed (figure 4.B). Although DLS measurements revealed a particle size distribution of 100 nm, in average, ICP-MS confirmed Ti absence in the sample fractions. Unfortunately DLS is not a reliable method for formulations containing fatty acids. The micelles formed during the sample preparation (i.e. sonication) are detectable by DLS even when the protocol is optimized for titania determination. Regardless of this size determination limits, online DLS data confirmed the presence of particles of increasing size as a function of exit time from the separation AF4 channel. This data is in agreement with those obtained with ICP-MS in off-line mode.

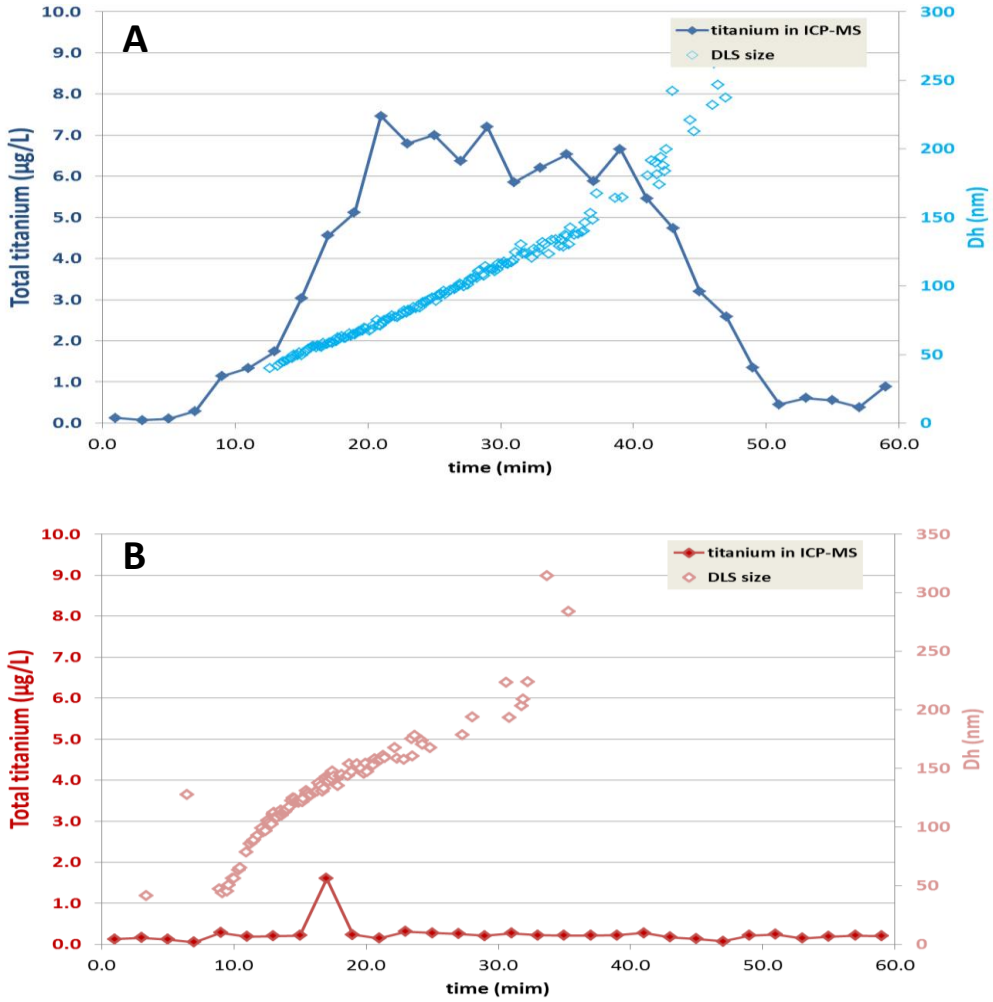

Figure 4. Analysis of eluted A) spiked sunscreen and B) blank cream by off-line ICP-MS. DLS data acquired on-line was aligned with ICP-MS data by elution time.

TEM imaging

TEM verification of the P25 sample fraction was performed in fractions were higher UV-Vis and DLS signal were recorded. Images revealed presence of variable sized agglomerates. Primary particle size was found to be around 20-30 nm. TEM data supports the limitation of both AF4/DLS and ICP-MS in determining the dispersion state of the sample.

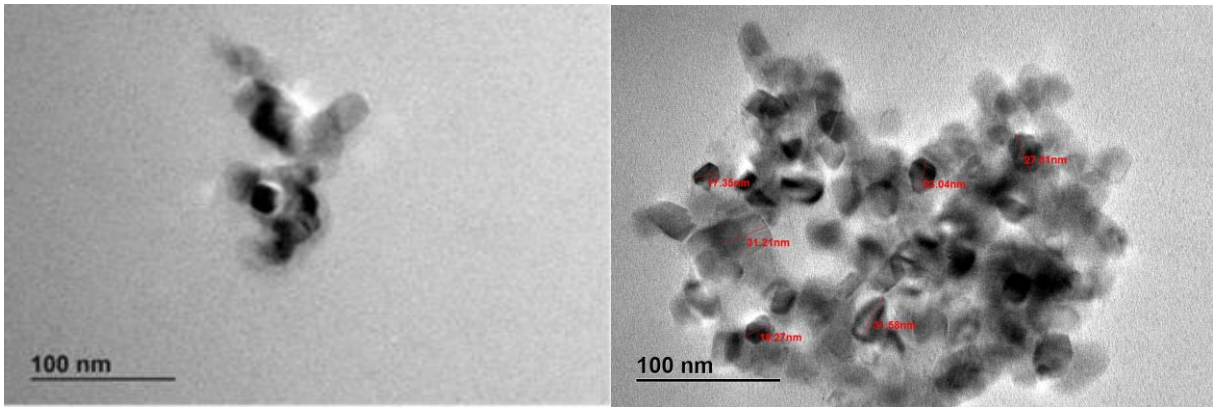

Figure 5. TEM images of P25 sample fractions.

Comparison of online / offline ICP-MS quantification

Comparison of on-line and off-line ICP-MS analysis showed very satisfying. Similarly to the off-line ICP-MS analysis, on-line analysis revealed the presence of Ti in the same concentration range. It was remarkable to see the range of titanium content for the AF4-separated nanoparticles showing a similar range, in on- and off-line mode, in the range 1.5 to 7 µg/L.The absence of titanium in the blank is confirmed by the on-line approach as well as the presence of titanium dioxide in the spiked cream. Recorded concentration also showed to be reproducible. It is interesting to notice that the noise of the measurement increases with elution time and therefore with size: since the particles are not digested, their size increases along with the elution time, the heterogeneous composition of the analysed fraction (solvent- TiO_2 particles) is probably causing an increase of the noise after 40 minutes.

The possibility to analyse the Ti content in real time and with no need for further sample manipulation decreases the overall analysis time, error and cost . The fact that the data is comparable also allows the samples to be shipped for analysis, in case an ICP-MS is not available in house.

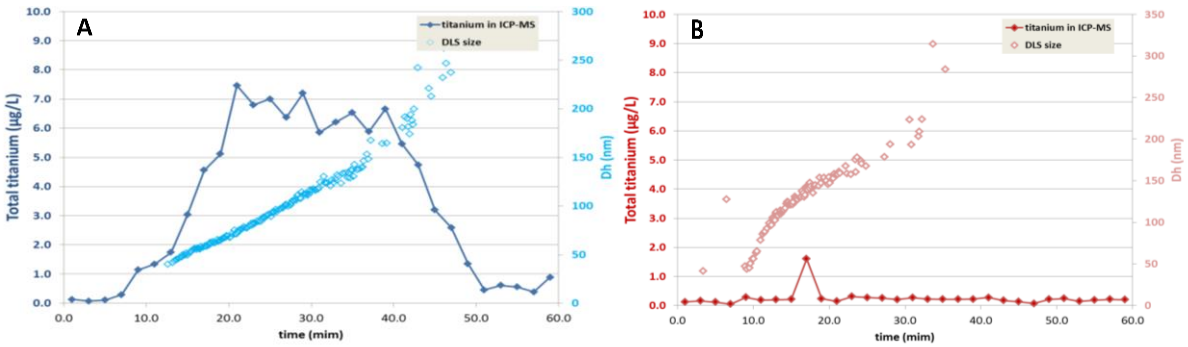

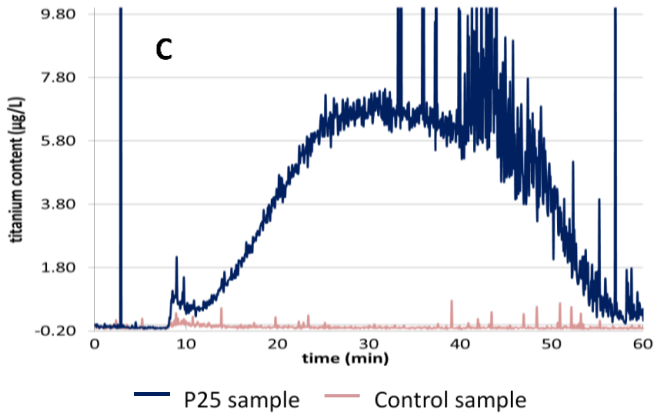

Figure 6. Quantification of titanium in eluted samples by off-line (A and B) on-line (C) ICP-MS analysis.

4.5. Conclusions

Cosmetics legislation raises the need for routine characterization methods although the evaluation of NP-containing creams is complex due to the complexity of its matrix.

AF4/DLS assessment of NP in commercial products has been reported but we show the inaptitude of this method to analyse materials rich in fatty acids and with unspecific adsorption wavelengths. When non-metallic particles are evaluated, and therefore no specific LSPR exists, UV-Vis is clearly not a useful technique. Our results suggest that also DLS is not suited to address the challenge of measuring nanoparticles in fatty creams. Micelles formed during sample preparation show a strict size range near 100 nm which mimics real NP in non-spiked creams and misreports the size of real NP. The use of ICP-MS solved the problem of false-positive particle detection and sizing reported by DLS. Moreover, we show the robustness of the ICP-MS in quantifying titanium in on-line mode. Although ICP-MS analysis of non-digested samples has losses in the order of 50%, the sensitivity of the method is enough to quantify creams spiked with as little as 1% TiO_2 NP.

Several issues remain to be solved, such as how to move from the previous results to a number-based particle size distribution as requested by the EC definition. Another problem that needs to be addressed is the determination of the dispersion state of the sample (revealed here by TEM).

We believe that this can be addressed by additional size measurement techniques. Single particle ICP-MS is a feasible alternative for particle sizing, although it does not give information on sample dispersion. A simpler approach is the off-line analysis of size distribution by CLS. Furthermore, sample preparation method should be improved in order to mitigate micelle formation.

4.6. Supporting information

4.6.1 I – Absorbance behaviour of titania materials

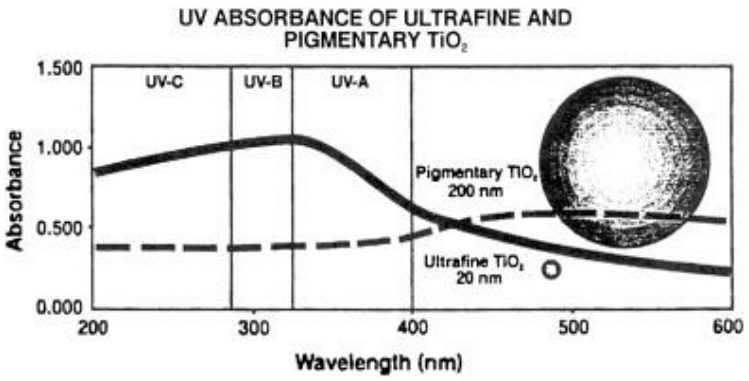

Figure S1. Comparison of the optical behaviour of ultrafine TiO_2 and pigmentary TiO_2.. (information from Kemira Pigments Oy)

4.6.2 **II -** Quantification of total titanium content

The standard procedure to measure the total content of titanium dioxide with ICP-MS involves the microwave digestion of the sample after incubation with a mixture of nitric acid, hydrogen peroxide, and hydrofluoric acid. To assess the performance of this quantification step we measured the recovery rates of a titanium dioxide nanoparticle sample (around 60 nm in size) spiked into two simple matrices (MilliQ water and MQ water with 0.02% SDS).
The following figure shows the results of three replicates of digested and not-digested spiked samples.

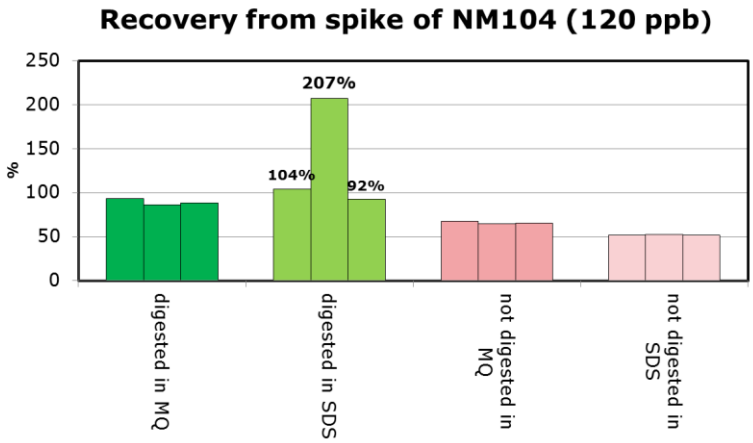

Figure S2. Plot of Ti recovery percentages, determined by ICP-MS, of TiO_2 NP dispersed in Milli Q water (MQ) or 2% SDS upon strong acidic digestion (digestion) or simple dilution (not digested).

The data indicate that:

Strong acidic and fluoride attack and digestion of Titanium increase the recovery rate.

There is a risk of contamination and "memory-effect" in the digestion process, as the special Teflon-made vials (needed for the fluoride attack) are very expensive and very difficult to clean.

We tried to develop an alternative digestion protocol using disposable tubes and milder digestion step on hot block. The light digestion protocol illustrated below allows the use of disposable tubes and avoids the risk of fraction contamination during preparation. It must be noticed that this risk is high due to the small concentration of the titanium in the fractions.

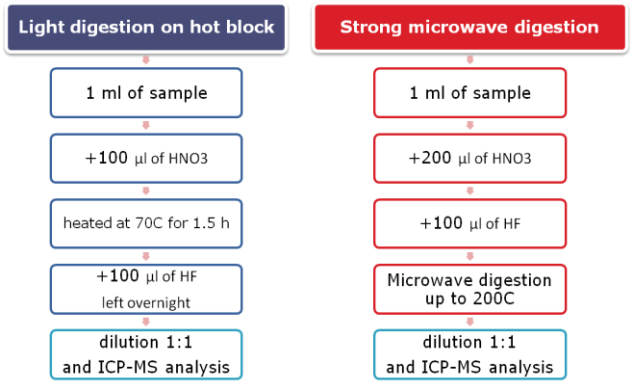

Figure S3. Comparison of protocols for ICP-MS analysis.

The comparison of the two methods (light and strong digestions) are given below and indicate that, while the strong digestion produced a recovery of 103% in SDS and 89% in water on

average, the light digestion recovery was below 50% and therefore does not represent a valuable alternative to microwave digestion since it is no better than simple dilution.

4.7. References

1. Calzolai, L., D. Gilliland, and F. Rossi, *Measuring nanoparticles size distribution in food and consumer products: a review.* Food Additives & Contaminants: Part A, 2012. **29**(8): p. 1183-1193.
2. Schmid, O. and T. Stoeger, *Surface area is the biologically most effective dose metric for acute nanoparticle toxicity in the lung.* Journal of Aerosol Science, 2016. **99**: p. 133-143.
3. Sager, T., C. Kommineni, and V. Castranova, *Pulmonary response to intratracheal instillation of ultrafine versus fine titanium dioxide: Role of surface area.* Part Fibre Toxicol., 2008. **5**.
4. *Regulation (EC) No 1223/2009 of the European Parliament and of the Council of 30 November 2009 on cosmetic products*, in *Official Journal of the European Union*.
5. Qu, H., et al., *Importance of material matching in the calibration of asymmetric flow field-flow fractionation: material specificity and nanoparticle surface coating effects on retention time.* Journal of Nanoparticle Research, 2016. **18**(10): p. 292.
6. Calzolai, L., et al., *Separation and characterization of gold nanoparticle mixtures by flow-field-flow fractionation.* J Chromatogr A, 2011. **1218**(27): p. 4234-9.

5. Chapter III

Inverse supercritical fluid extraction as a sample preparation method for the analysis of the nanoparticle content in sunscreen agents

David Müller[1,2], Stefano Cattaneo[1], Florian Meier[3], Roland Welz[3], Tjerk de Vries[4], Meital Portugal-Cohen[5], Diana C. António[6], Claudia Cascio[6], Luigi Calzolai[6], Douglas Gilliland[6], Andrew de Mello[2]

[1] Centre Suisse d'Electronique et de Microtechnique (CSEM), Bahnhofstrasse 1, 7302 Landquart, Switzerland

[2]Institute for Chemical and Bioengineering, Department for Chemistry and Applied Biosciences, ETH Zürich, Vladimir-Prelog-Weg 1, 8093 Zürich, Switzerland

[3]Postnova Analytics GmbH, Max-Planck-Str. 14, 86899 Landsberg am Lech, Germany

[4]Feyecon Carbon Dioxide Technologies, Rijnkade 17a, 1382 GS Weesp, The Netherlands

[5]AHAVA Dead Sea Laboratories, 1 Arava Street, 70150 Lod, Israel

[6]European Commission – Joint Research Centre, IHCP, via E. Fermi 2749 I, 21027 Ispra (VA), Italy

Journal of Chromatography A, Volume 1440, 1 April 2016, Pages 31–36
doi: 10.1016/j.chroma.2016.02.060

5.1. Abstract

We demonstrate the use of inverse supercritical carbon dioxide ($scCO_2$) extraction as a novel method of sample preparation for the analysis of complex nanoparticle-containing samples, in our case a model sunscreen agent with titanium dioxide nanoparticles. The sample was prepared for analysis in a simplified process using a lab scale supercritical fluid extraction system. The residual material was easily dispersed in an aqueous solution and analyzed by Asymmetrical Flow Field-Flow Fractionation (AF4) hyphenated with UV- and Multi-Angle Light Scattering detection. The obtained results allowed an unambiguous determination of the presence of nanoparticles within the sample, with almost no background from the matrix itself, and showed that the size distribution of the nanoparticles is essentially maintained.

These results are especially relevant in view of recently introduced regulatory requirements concerning the labelling of nanoparticle-containing products. The novel sample preparation method is potentially applicable to commercial sunscreens or other emulsion-based cosmetic products and has important ecological advantages over currently used sample preparation techniques involving organic solvents.

Keywords: sample preparation; supercritical carbon dioxide; nanoparticle separation; inverse supercritical fluid extraction; field flow fractionation.

5.2. Introduction

Today, a growing number of consumer products make use of the unique physical and chemical properties of nanomaterials. As the number of such products increases, the ability to thoroughly characterize their properties and functionality becomes critical. In particular, the recent regulatory efforts concerning the labeling of nanoparticle-containing consumer products, e.g., the EU regulations on cosmetics [1] and food [2], call for the development of simple and robust sample preparation protocols enabling a reliable detection and quantification of nanoparticulate ingredients in complex matrices [3–5]. This problem is especially challenging in case of emulsion-based consumer products such as cosmetics, which often consist of complex multicomponent matrices [6]. Commercially available sunscreen formulations for example usually contain more than 20 ingredients with different functions and physicochemical properties. Moreover, such viscous samples cannot be directly injected into an analytical system, and need to be liquefied prior to analysis. Commonly applied sample preparation protocols include chemical treatments using organic solvents [7–11]. Such complex processes are both time-consuming and have a considerable environmental impact due to the extensive use of organic solvents of which many are ecologically harmful [12–14]. The generalization and simplification of sample preparation workflows, as well as the reduced usage of organic solvents, is therefore likely to have a significant impact on the utility of analyses of nanoparticle-containing samples.

To this end, we herein report the use of inverse supercritical fluid extraction (inverse SFE) [14–18], a more ecological and simpler sample preparation method based on the use of supercritical fluids. For our application we selected supercritical carbon dioxide ($scCO_2$), as many of the chemical excipients found in large numbers in emulsion-based cosmetic products

are of a fatty and non-polar nature and therefore exhibit a high solubility in CO_2. Furthermore, $scCO_2$ is chemically inert [18], nontoxic, nonflammable [19], and it is well-known for its application in SFE processes, where it is commonly used to extract small and/or non-polar molecules from natural materials under very mild conditions [20–23]. Besides the extraction of essential oils from herbs and spices [24,25], the most prominent application of SFE is the removal of caffeine from coffee beans [26,27]. The process has also been employed for the extraction and analysis of antioxidants, preservatives and sunscreen agents in cosmetics [28,29]. In these applications, however, the SFE is used to dissolve and extract the analyte from the matrix. In this work, inverse SFE is used as a sample treatment to simplify the matrix by removing unwanted components, thus keeping the target nanomaterials in the residual sample. Inverse SFE has also been studied for over twenty years. To date, it has primarily been used for the isolation of non-polar pharmaceutical formulations from polar analytes [14,16,17] and not for the pre-treatment of nanoparticle-containing samples. The minimal surface tension, low viscosities and gas-like diffusivities of $scCO_2$ allow for thorough sample penetration whilst maintaining the structure of the residual material [14]. Once the sample treatment is completed, the CO_2 is simply removed by lowering the pressure to below the critical threshold and returning to ambient conditions. The remaining material consists of the polar components (thickening agents) along with the nanoparticles that accordingly, can easily be rewet and subsequent dispersed in a direct manner. To demonstrate the potential utility of such a sample preparation process in the analysis of nanoparticle containing sunscreens, we integrated the $scCO_2$ treatment with Asymmetrical Flow Field-Flow Fractionation (AF4) hyphenated with UV and Multi-Angle Light Scattering (MALS) detection, and tested the method with a model sunscreen sample. The obtained findings were verified by Scanning Transmission Electron Microscopy (STEM) and Energy-Dispersive X-ray (EDX) analysis. Although the method is demonstrated using a model sunscreen matrix, we expect it to be applicable to commercial sunscreens or other emulsion-based cosmetic products, which include fatty additives with a high solubility in $scCO_2$.

5.3. Materials and Methods

5.3.1 Chemicals

5.3.1.1 Titanium dioxide nanoparticle samples

A titanium dioxide (TiO_2) -nanoparticle dispersion, AERODISP® W 740 X (40 % w/w, EVONIK Industries, Hanau, Germany) was diluted with ultrapure water (MilliQ, Billerica, USA). This was followed by addition of 0.2% (v/v) NovaChem (Postnova Analytics GmbH, Landsberg, Germany) to yield a final particle concentration of 0.2 mg / mL. NovaChem is a mixture of non-ionic and ionic detergents that helps to prevent particle agglomeration. Prior to analysis, the sample was placed in an ultrasonic bath (Sonorex Digital 10 P, Bandelin, Berlin, Germany) and sonicated at maximum power (320 W, 35 kHz) for 30 minutes to further reduce eventual particle agglomerates.

5.3.1.2 Model sunscreens

The novel sample preparation method was tested on two complex sunscreen model samples, one with and one without nanoparticles. The creams were produced separately, although both consisted of the following excipients: Avicel® PC611 (FMC Biopolymer, Brussels, Belgium), glycerin (Thai Oleochemicals Limited, Bangkok, Thailand), KELTROL® T (Bronson & Jacobs Pty Ltd, Villawood, NSW, Australia), potassium sorbate (APAC Chemical Corp., Arcadia, CA, USA) and ultrapure water (MilliQ, Billerica, USA) in the water phase and Antaron™ V216 (ISP Ltd., Tadworth, UK), Arlacel™ 165 (JEEN, Fairfield, NJ, USA), capric/caprilic triglycerine (HENKEL KGaA, Düsseldorf, Germany), cyclomethiocone (Momentive Amer Ind., Waterford, NY, USA), Emulsiphos® (Symrise, Holzminden, Germany), isostearyl isostearate (UNIQEMA Corp., New Castle, DE, USA), octyl palmitate (Eigenmann & Veronelli, Milano, Italy), stearyl alcohol (Temix International, Milano, Italy), TEGO® Care 450 (EVONIK Industries, Essen, Germany), Finsolv® TN (Innospec, Englewood, CO, USA) and tocopheryl acetate (BASF SE, Ludwigshafen, Germany) in the oil phase. Both phases were mixed independently for 15 minutes using a L4R Mixer (Silverson Machines Inc., East Longmeadow, MA, USA) at 6000 rpm before they were homogenized together for another 15 minutes using again the L4R at 6000 rpm. In the last step, Dow Corning® 1503 (Dow Corning Corporation, Midland, MI, USA), Euxyl® PE 9010 (Schülke & Mayr GmbH, Norderstedt, Germany) and 12.5 % w/w of a AERODISP® W 740 X TiO_2 nanoparticle dispersion (40% w/w, EVONIK Industries, Essen, Germany) were added to one

cream, resulting in a TiO_2 particle concentration of 5.0 % w/w, a concentration typically found in commercial sunscreens [9,30]. In the blank cream, the AERODISP® nanoparticles were replaced with corresponding amounts of ultrapure water (MilliQ, Billerica, USA). Both creams were homogenized again for 5 minutes at 4000 rpm, before they were filled into tubes and stored at room temperature.

5.3.2 Sample treatment

5.3.2.1 Extraction equipment

Extraction was performed using a lab scale supercritical fluid extraction system (Lab SFE 100ml, Separex, Champigneulles, France). The system was equipped with a high-pressure CO_2 pump, a pressure/flow regulating system, and a horizontally mounted 100 ml extraction vessel housed in a thermostated oven.

5.3.2.2 Supercritical CO_2 sample treatment

The model sunscreen (Figure 1A) was placed on a Teflon cartridge surrounded by a stainless steel holder (Figure 1B). The Teflon part contained a small recess resulting in a cavity with dimensions of 60 x 10 x 0.2 mm. To ensure that a reproducible sample volume was assayed, excess sunscreen was removed each time using a spatula. The Teflon cartridge was then removed from its holder (Figure 1C) and placed in the extraction vessel (100 mL, Separex, Champigneulles, France). The sample was then subjected to a constant $scCO_2$ flow of 100 g/min for 30 minutes at 40° C and 131 bars. The optimum parameters were selected by performing a series of measurements with varying processing times, temperatures and pressures. Less aggressive conditions (such as shorter processing times, lower temperatures and lower pressures) resulted in reduced extraction efficiencies of the fatty components, leading to reduced solubility in water, whilst harsher conditions led to more extensive particle aggregation and reduced reproducibility. The treated sample (Figure 1D) was then removed from the cartridge (Figure 1E) and dissolved in ultrapure water (MilliQ, Billerica, USA), to which 0.2% (v/v) NovaChem (Postnova Analytics GmbH, Landsberg am Lech, Germany)

was added until a concentration of less than 0.2 mg TiO_2 (related to a recovery of 100%) per mL of solvent (Figure 1F). Sample dilution is necessary to prevent overloading effects, which cause peak shifts and further advanced particle aggregation. Extractions for both creams (with and without nanoparticles) were performed in triplicate.

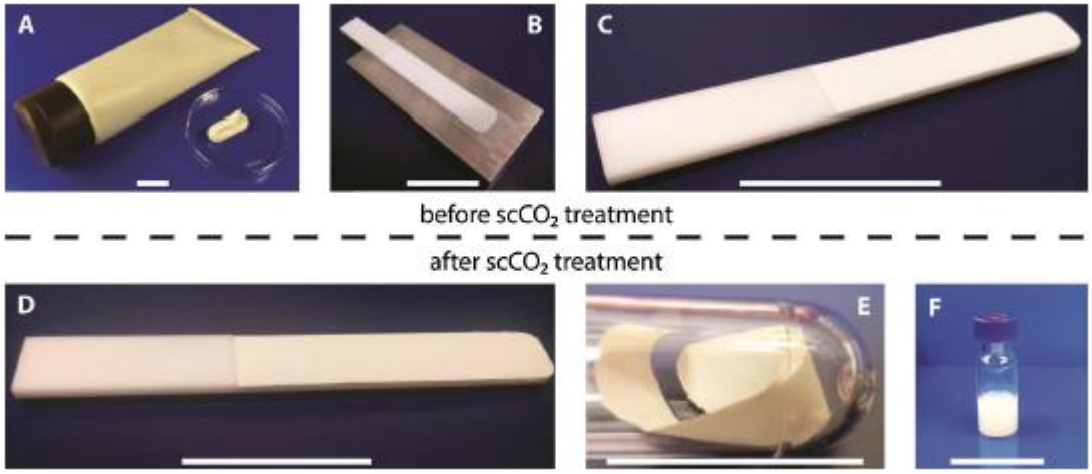

Figure 1. Model sunscreen at different stages before (A – C) and after (D – F) the supercritical CO_2 treatment. Scale bars are 25 mm. (A) The cream after being freshly dispensed from the tube. (B) Cream after deposition on the Teflon cartridge, held within the stainless steel holder. Excess cream is removed with a spatula to ensure a reproducible sample amount. (C) Teflon cartridge after being removed from the holder. The left side shows the handle of the cartridge, while the right (slightly shinier) side is the untreated, deposited cream. (D) After being processed by supercritical CO_2, the residual material has a darker, slightly beige color. (E) The sample is scraped off from the cartridge and stored in a plastic tube. (F) Before being processed by hyphenated AF4-UV-MALS, the residual material is re-dispersed in 0.2 % NovaChem solution.

5.3.3 Multi-detector asymmetrical flow field-flow fractionation

5.3.3.1 Instrumentation and carrier liquid

Sunscreen samples were analyzed using a commercially available AF4 system (AF2000 MF, Postnova Analytics GmbH (PN), Landsberg am Lech, Germany) incorporating an autosampler (PN5300), channel thermostat (PN4020), UV (PN3211) and Multi-Angle Light Scattering MALS (PN3621, 21 angles) detectors. The storage temperature in the autosampler

was set to 4°C and the channel thermostat was set to 25°C. UV detection was performed at 254 nm and the MALS detector provided the gyration radius of the particles exiting the AF4 separation cartridge (calculated with random coil model). The eluent was prepared using filtrated ultrapure water (MilliQ, Billerica, USA), to which 0.2 % (v/v) filtered NovaChem (Postnova Analytics GmbH, Landsberg am Lech, Germany) was added. An analytical AF4 cartridge (S-AF4-CHA-611) incorporating a 10 kDa regenerated cellulose membrane (Z-AF4_MM-612-10KD) and a 350 µm thick Mylar spacer was used for all measurements and the injection volume was always set to 20 µl. Separations and analysis were performed in triplicates for each of the sample. In order to compensate the baseline drifts, the UV data was corrected by subtracting a blank run signal measured after an injection of pure eluent. Data acquisition and MALS calculations were performed using the AF2000 Control Unit software (Postnova Analytics GmbH, Landsberg am Lech, Germany) and further evaluations (such as curve normalization) were performed using OriginPro 2015 (OriginLab Corporation, USA).

5.3.3.2 Elution profile

An optimized focusing and elution method was developed to ensure reproducible analysis. The focusing step of the selected elution profile was commenced with a 7 minute long injection flow of 0.2 mL/min and with a cross-flow of 1.4 mL/min. After a 30 second long transition time, elution started with a constant cross-flow of 1.4 mL/min for an additional 5 minutes, followed by an exponentially decreasing crossflow (exponent: 0.2), reaching a final value of 0.1 mL/min after 40 min, which was then maintained for 25 minutes. To ensure a stable signal, the detector flow rate was maintained at 0.5 mL/min, with the other flows adjusted accordingly.

5.3.4 Recovery rate and limit of detection/quantification

In addition to the size determination by MALS, quantitative data about the recovery of TiO_2 was gathered by measuring the area under the curve of the UV detector signal. With eight injections of different amounts of the pure AERODISP dispersion over 1.5 orders of magnitude, a value of 642.0 A.U. per µg TiO_2 was determined (Intercept: 0.58 (SE: 1.20), Slope: 642.01 (SE: 9.89), adj. R^2 of 0.998). To further focus on nanoparticulate TiO_2 and particles in the smaller sub-micron regime, a time range of 15 to 50 minutes of elution time was selected, corresponding to particles having their radius of gyration roughly between 20

and 160 nm. For the pure AERODIPS dispersion only 89.4 ± 3.6% (n = 3) of its content was measured in that time frame. This results in an expected signal of 574.0 ± 23.2 A.U. for this time frame per injected µg of TiO_2.

To only measure the TiO_2-related UV-absorption of our samples, a blank run with pure eluent was subtracted from the AERODISP run, whereas the separation of a nanoparticle-free sunscreen was subtracted from the runs with the nanoparticle-containing sunscreens. The recovery rate was then calculated based on the expected absorption corresponding to the amount of sunscreen originally deposited on the Teflon cartridge.

Determination of the signal-to-noise (S/N-) ratio was performed by comparing measured signals from the nanoparticle-containing sunscreens with those of nanoparticle-free cream samples (blank eluent runs were subtracted from both) and establishing the minimum concentration at which the analyte can be reliably detected. To mainly focus on nanoparticulate TiO_2, a fraction with an elution time between 15 and 35 minutes was selected, corresponding to particles having their radius of gyration roughly between 20 and 60 nm. A S/N-ratio of 3 is used for the limit of detection (LOD) and a S/N-ratio of 10 is used for the limit of quantification (LOQ).

5.3.5 Electron Microscopy

A droplet of sample was deposited on a copper grid covered by a thin carbon layer. The pure nanoparticle dispersion was then observed using a Transmission Electron Microscope (CM200 TEM, Philips, Eindhoven, The Netherlands). The $scCO_2$ treated samples were further analyzed with a Scanning Electron Transmission Microscope (Talos F200X, FEI, Hillsboro, OR, USA) equipped with an X-FEG and a Super-X EDS system for spectroscopic mapping.

5.4. Results and discussion

5.4.1 Hyphenated AF4-UV-MALS measurement

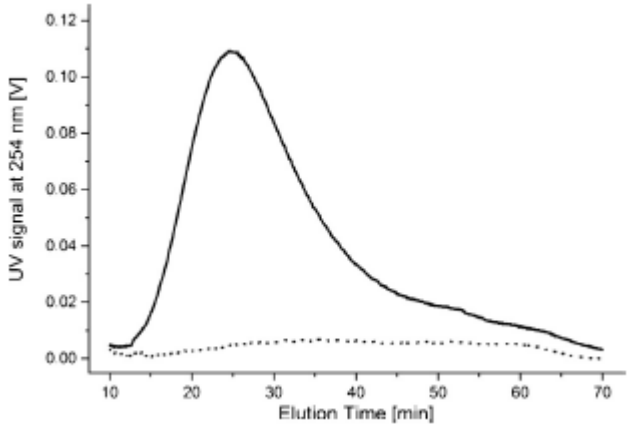

Figure 2. Elugrams of the model sunscreens with and without nanoparticles. The black solid line reports the analysis of the re-suspension of the $scCO_2$ treated sample with 5 % TiO_2 nanoparticles. A wide peak, indicating particles with a broad size distribution and hence eluting over an extended separation period, is evident. For the nanoparticle-free sample (black dotted line, also treated with $scCO_2$), no significant signal is detected over the complete separation cycle.

After sonication, the re-dispersed samples were directly injected into the AF4 system. As shown in Figure 2, the resulting UV curve allows an unambiguous distinction between the cream that contains nanoparticles (solid black line) and the nanoparticle-free sample (dotted black line). To investigate whether the sample preparation method induces a change in the size distribution of the nanoparticles, we compared the elugram and MALS data from a diluted dispersion of the pure AERODISP® nanoparticles to those obtained from the cream with nanoparticles after $scCO_2$ treatment and resuspension. To remove possible matrix effects, the UV signal of the $scCO_2$ treated blank cream was subtracted from that of the spiked cream. The resulting comparison (**Error! Reference source not found.**) shows that the original nanoparticle dispersion (dashed black line) elutes slightly earlier and with a narrower peak profile than the $scCO_2$-treated counterparts (gray band). At peak-maximum of the UV curve, this corresponded to an increase in radius of gyration from 32.9 nm (SD: 0.3 nm) in the pure dispersion to 34.0 nm (SD: 1.2 nm) in the $scCO_2$-treated model cream. Beside the slight shift of the UV peak, the main difference between the signal of the treated and the untreated nanoparticles are some large agglomerates with gyration radii in the range of several hundred nanometers (mainly between 40 and 60 minutes), that were observed in the $scCO_2$-treated sample only. It is known that the presence of organic acids can diminish the suspension stability of TiO_2 nanoparticles [31] and that such acids can be formed in the presence of water and $scCO_2$ [32]. However, it is also possible that the agglomeration occurred during one of

the preceding steps in the sample life cycle (manufacturing/homogenization or storage) and is not necessarily due to the $scCO_2$ sample treatment. The particle radii of gyration extracted from the MALS measurements of the three $scCO_2$ treated samples are all within the red band in **Error! Reference source not found.** and, considering the expected measurement uncertainty, are consistent with the data from the pure AERODISP® nanoparticles (red dashed line). This confirms that the $scCO_2$ treatment does not have a significant impact on the overall relationship between size and elution time, indicating that the interaction between the particles and the membrane/eluent has not been significantly altered.

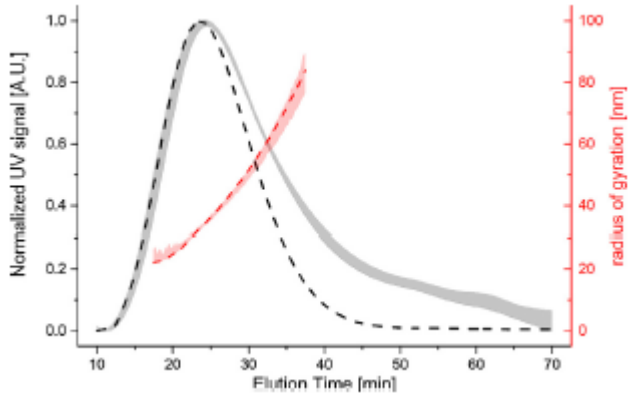

Figure 3. UV curves (black) and MALS measurements (red) of the pure nanoparticle dispersion and the $scCO_2$ processed model sunscreen with nanoparticles. For both measurements, the dashed lines represent the data from pure AERODISP dispersion, whereas the data from triplicate measurements of the $scCO_2$ treated samples are combined in a band. The UV signal of the AERODISP nanoparticle dispersion elutes slightly earlier and with a narrower peak profile than the $scCO_2$-treated counterparts. Besides this, the main difference between the measurements is the presence of large agglomerates in the treated samples, having gyration radii in the range of several hundred nanometers (mainly between 40 and 60 minutes). Such agglomerates might occur during the sample pre-treatment or during one of the preceding steps in the sample life cycle.

5.4.2 Electron microscopy and particle analysis

To confirm that the detected signal in the processed model sunscreen originates from titanium dioxide nanoparticles, a sample fraction (taken at the maximum of the UV-peak) was further investigated using Transmission Electron Microscopy (TEM). Figure 4A shows titanium dioxide nanoparticles from a diluted AERODISP® W 740 X TiO_2 dispersion. The

nanoparticles have a distinct, particle-like morphology with a relatively broad size distribution consistent with the data obtained from MALS. The contrast between the particles and the amorphous carbon sample grid is strong and allows for easy imaging using classical TEM. The nanoparticles that remain after the $scCO_2$ sample treatment however could not be imaged with classical TEM, likely due to remaining water-soluble cream-components significantly decreasing the overall contrast. Using an Energy-Dispersive X-ray (EDX) detector, we specifically mapped the sample for the spectroscopic signal of titanium (Figure 4B). Further mapping for the oxygen content resulted in an overlapping signal (Figure 4C), confirming the presence of TiO_2. While the titanium mapping shows a distinctive particle boundary, the oxygen signal appears to be more diffuse, extending beyond the particles. This may partially originate from polar organic materials in the cream that remain after the $scCO_2$ extraction process. However, the main contribution to this background signal in the oxygen map is caused by the thin carbon-layer of the TEM grid, which is slightly oxidizing under ambient air conditions. This is a known contamination that cannot be prevented in a simple manner. To retrieve the morphological form of the $scCO_2$-treated particles, a High-Angle Annular Dark-Field (HAADF) detector was used, which is especially sensitive towards elements with a high atomic number. Employing this detector with the Scanning Transmission Electron Microscope (STEM) for imaging, the particles could be imaged as shown in Figure 4D. An overlay of both EDX-maps and the HAADF-image (Figure 4E) therefore confirmed that the particles detected in the processed sunscreen are indeed titanium dioxide nanoparticles, and that their morphological structure is preserved throughout the analytical procedure.

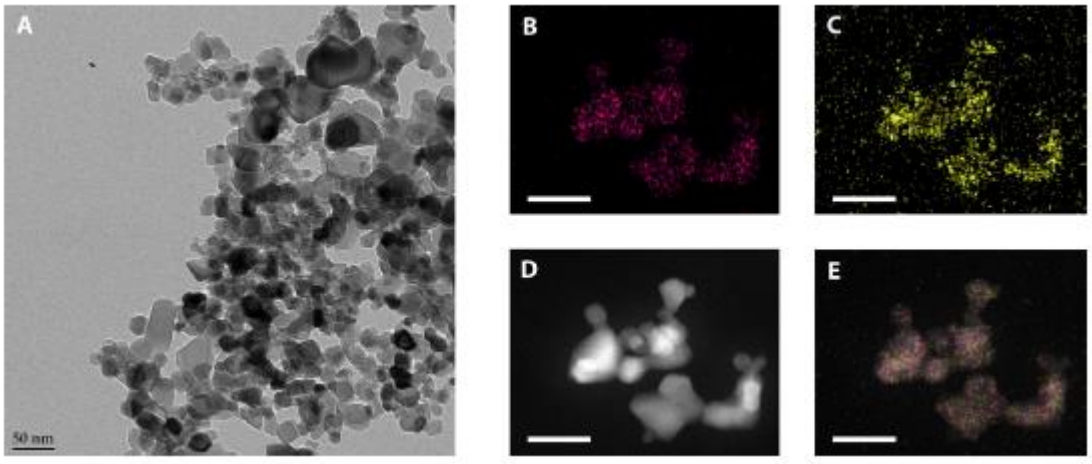

Figure 4. Transmission electron microscopy images of the untreated suspension (A) and STEM-EDX chemical mapping as well as HAADF images of the $scCO_2$-treated TiO_2

nanoparticles (B-E). Scale bars are 50 nm. (A) TEM micrograph of the diluted AERODISP dispersion, indicating a broad particle size distribution. The STEM-EDX maps show the elemental content of (B) titanium and (C) oxygen. (D) STEM image of the $scCO_2$-treated nanoparticles, taken with a high-angle annular dark field (HAADF) detector. (E) Overlay of the STEM-EDX maps of oxygen and titanium with the STEM-HAADF image of the same section. The precise overlay clearly demonstrates that the nanoparticles are indeed titanium dioxide nanoparticles. The main contribution to the background signal in the oxygen map is caused by the thin carbon-layer of the TEM grid, which is slightly oxidizing under ambient air conditions.

5.4.3 Recovery rate and limit of detection/quantification

For the evaluation of the recovery rate, the eluting TiO_2 of the three $scCO_2$-treated samples with nanoparticles was quantified using the conditions described in the Experimental section. The percentage recovery based on the mass of cream deposited on the cartridge, the dilution of the sample during resuspension and the total injection amount at the separation, was calculated. Recoveries (n = 3) of the three samples were 51.2 ± 2.1 %, 48.0 ± 2 %, and 52.2 ± 2.3 %, resulting in an overall recovery of 50.2 ± 4.2 %.This certainly leaves room for improvement, but is also significantly higher than what has been previously reported, e.g. for the extraction with organic solvents and tip sonication (8.14 – 21.47 % in case of Ref. [9]).
The LOD for a single injection of 20 µl was found to be 0.6 µg of TiO_2 (30 µg/mL), corresponding to a LOQ of 2.0 µg (0.1 mg/mL). The later approximately corresponds to a TiO_2 content of 0.5% (w/w) in the original sunscreen. This limits are well below the TiO_2 concentrations typically used in commercial sunscreen samples [9,30].

5.5. Conclusions

Prior research has demonstrated a variety of different sample pre-treatment methods for sunscreens and other consumer products containing nanoparticles, which are used to prepare them for subsequent analysis of the nanoparticle characteristics. Regrettably, most of these techniques suffer from the need to involve several working steps, which may impact the accuracy of the nanoparticle analysis. Furthermore, these techniques use large amounts of

commonly aggressive and expensive chemicals, which have consequences for both operator safety and environmental sustainability.

In this work, we have presented a sample preparation method based on an inverse supercritical fluid extraction treatment that can be executed in a simple manner, and where the safe and non-toxic properties of CO_2 result in the elimination of ecological drawbacks, health hazards and associated disposal costs [14]. After treatment, the residual material can be easily re-dispersed in an aqueous solution and directly analyzed. Using AF4-UV-MALS, we confirmed the applicability of the $scCO_2$ method for the analysis of multicomponent and fatty samples in order to determine their nanoparticle content. The measurements were verified by STEM and EDX analysis. The results demonstrated that the presence of nanoparticles in a model sunscreen can be precisely determined, that a good recovery rate of roughly 50% of the particles of interest can be achieved and that the size distribution of those nanoparticles is essentially maintained. Compared to the original nanoparticle dispersion, an increase in larger particles / agglomerates was observed in the $scCO_2$-treated samples. This slight agglomeration might be caused by the sample treatment itself, but might also have occurred previously, e.g. during homogenization or storage. Overall, however, the size and morphology of the treated nanomaterials are found to be very similar to the original suspension, which is especially relevant in view of the recent regulatory requirements for nanoparticle containing cosmetics. Although the method is demonstrated using a model sunscreen matrix, we expect it to be applicable to commercial sunscreens or other emulsion-based cosmetic products.

Acknowledgments

This work was supported by the European Commission 7th Framework Programme (project SMART-NANO, NMP4-SE-2012-280779). Furthermore, the authors acknowledge the support of the Scientific Center for Optical and Electron Microscopy (ScopeM) at the Swiss Federal Institute of Technology ETHZ.

5.6. References

1. EC, REGULATION (EC) No 1223/2009 on cosmetic products, Off. J. Eur. Union. (2009) 59–209.
2. EC, REGULATION (EU) No 1169/2011 on the provision of food information to

consumers, Off. J. Eur. Union. (2011) 18–63.

3. A. Ulrich, S. Losert, N. Bendixen, A. Al-Kattan, H. Hagendorfer, B. Nowack, et al., Critical aspects of sample handling for direct nanoparticle analysis and analytical challenges using asymmetric field flow fractionation in a multi-detector approach, J. Anal. At. Spectrom. 27 (2012) 1120. doi:10.1039/c2ja30024a.
4. K. Loeschner, J. Navratilova, C. Købler, K. Mølhave, S. Wagner, F. Von Der Kammer, et al., Detection and characterization of silver nanoparticles in chicken meat by asymmetric flow field flow fractionation with detection by conventional or single particle ICP-MS, Anal. Bioanal. Chem. 405 (2013) 8185–8195. doi:10.1007/s00216-013-7228-z.
5. S. Wagner, S. Legros, K. Loeschner, J. Liu, J. Navratilova, R. Grombe, et al., First steps towards a generic sample preparation scheme for inorganic engineered nanoparticles in a complex matrix for detection, characterization, and quantification by asymmetric flow-field flow fractionation coupled to multi-angle light scattering and , J. Anal. At. Spectrom. 00 (2015) 1–11. doi:10.1039/C4JA00471J.
6. L. Calzolai, D. Gilliland, F. Rossi, Measuring nanoparticles size distribution in food and consumer products: a review, Food Addit. Contam. Part A. 29 (2012) 1183–1193. doi:10.1080/19440049.2012.689777.
7. C. Contado, A. Pagnoni, TiO_2 nano- and micro-particles in commercial foundation creams: Field Flow-Fractionation techniques together with ICP-AES and SQW Voltammetry for their characterization, Anal. Methods. 2 (2010) 1112–1124. doi:10.1039/c0ay00205d.
8. A. Samontha, J. Shiowatana, A. Siripinyanond, Particle size characterization of titanium dioxide in sunscreen products using sedimentation field-flow fractionation-inductively coupled plasma-mass spectrometry., Anal. Bioanal. Chem. 399 (2011) 973–978. doi:10.1007/s00216-010-4298-z.
9. C. Contado, A. Pagnoni, TiO_2 in commercial sunscreen lotion: flow field-flow fractionation and ICP-AES together for size analysis., Anal. Chem. 80 (2008) 7594–608. doi:10.1021/ac8012626.
10. R. Dunford, A. Salinaro, L. Cai, N. Serpone, S. Horikoshi, H. Hidaka, et al., Chemical oxidation and DNA damage catalysed by inorganic sunscreen ingredients, FEBS Lett. 418 (1997) 87–90. doi:10.1016/S0014-5793(97)01356-2.
11. Z. a. Lewicka, A.F. Benedetto, D.N. Benoit, W.W. Yu, J.D. Fortner, V.L. Colvin, The structure, composition, and dimensions of TiO_2 and ZnO nanomaterials in commercial

sunscreens, J. Nanoparticle Res. 13 (2011) 3607–3617. doi:10.1007/s11051-011-0438-4.

12. C. Capello, U. Fischer, K. Hungerbu, What is a green solvent ? A comprehensive framework for the environmental assessment of solvents, Green Chem. 9 (2007) 927–934. doi:10.1039/b617536h.
13. J.O. Metzger, Solvent-Free Organic Syntheses, Angew. Chem. Int. Ed. Engl. 37 (1998) 2975–2978.
14. W.N. Moore, L.T. Taylor, Analytical inverse supercritical fluid extraction of polar pharmaceutical compounds from cream and ointment matrices, J. Pharm. Biomed. Anal. 12 (1994) 1227–1232.
15. A.L. Howard, M.C. Shah, P. Ip, A. Brooks, J. Thompson, T. Taylor, Use of Supercritical Fluid Extraction for Sample Preparation of Sustained-Release Felodipine Tablets, (1994) 1537–1542.
16. D.C. Messer, L.T. Taylor, Inverse Analytical Supercritical Fluid Extraction of Zovirax Ointment 5 %, Anal. Chem. 66 (1994) 1591–1592.
17. R.A. Almodo, R.A. Rodrı, Inverse supercritical extraction of acetaminophen from suppositories, J. Pharm. Biomed. Anal. 17 (1998) 89–93.
18. S. Scalia, S. Simeoni, Assay of Xanthene Dyes in Lipsticks by Inverse Supercritical fluid Extraction and HPLC, Chromatographia. 53 (2001) 490–494.
19. G. Kaupp, Reactions in Supercritical Carbon Dioxide, Angew. Chem. Int. Ed. Engl. 33 (1994) 1452–1455.
20. D.P. Ndiomu, C.F. Simpson, Some Applications of Supercritical Fluid Extraction, Anal. Chim. Acta. 213 (1988) 237–243.
21. S.B. Hawthorne, Analytical-Scale Supercritical Fluid Extraction, Anal. Chem. 62 (1990) 633–642.
22. H. Engelhardt, J. Zapp, P. Kolla, Sample Preparation by Supercritical Fluid Extraction in Environmental Food and Polymer Analysis, Chromatographia. 32 (1991) 527–537.
23. E. Reverchon, I. De Marco, Supercritical fluid extraction and fractionation of natural matter, J. Supercrit. Fluids. 38 (2006) 146–166. doi:10.1016/j.supflu.2006.03.020.
24. M. Goto, M. Sato, T. Hirose, Extraction of peppermint oil by supercritical carbon dioxide, J. Chem. Eng. Japan. 26 (1993) 401–407. doi:10.1252/jcej.26.401.
25. B.C. Roy, M. Goto, T. Hirose, Extraction of Ginger Oil with Supercritical Carbon Dioxide: Experiments and Modeling, Ind. Eng. Chem. Res. 35 (1996) 607–612. doi:10.1021/ie950357p.

26. H. Peker, M. Srinivasan, J. Smith, B. McCoy, Caffeine extraction rates from coffee beans with supercritical carbon dioxide, AIChE J. 38 (1992) 761–770. doi:10.1002/aic.690380513.
27. J. Tello, M. Viguera, L. Calvo, Extraction of caffeine from Robusta coffee (Coffea canephora var. Robusta) husks using supercritical carbon dioxide, J. Supercrit. Fluids. 59 (2011) 53–60. doi:10.1016/j.supflu.2011.07.018.
28. M.R. Lee, C.Y. Lin, Z.G. Li, T.F. Tsai, Simultaneous analysis of antioxidants and preservatives in cosmetics by supercritical fluid extraction combined with liquid chromatography-mass spectrometry, J. Chromatogr. A. 1120 (2006) 244–251. doi:10.1016/j.chroma.2006.01.075.
29. S. Scalia, Determination of sunscreen agents in cosmetic products by supercritical fluid extraction and high-performance liquid chromatography., J. Chromatogr. A. 870 (2000) 199–205.
30. A. Weir, P. Westerhoff, L. Fabricius, N. von Goetz, Titanium dioxide Nanoparticles in Food and Personal Care Products, Env. Sci Ttechnol. 46 (2012) 2242–2250. doi:10.1021/es204168d.Titanium.
31. J.M. Pettibone, D.M. Cwiertny, M. Scherer, V.H. Grassian, Adsorption of Organic Acids on TiO_2 Nanoparticles: Effects of pH, Nanoparticle Size, and Nanoparticle Aggregation, Langmuir. 24 (2008) 6659–6667.
32. Y.S. Choi, S. Nešić, Determining the corrosive potential of CO2 transport pipeline in high pCO2-water environments, Int. J. Greenh. Gas Control. 5 (2011) 788–797. doi:10.1016/j.ijggc.2010.11.008.

6. Chapter IV

Characterization of Silver Nanoparticles-Alginate conplexes by combined Size Separation and Size Measurement Techniques

Diana C. António[ac], Claudia Cascio[b], Douglas Gilliland[a], António J. A. Nogueira[c], François Rossi[a], Luigi Calzolai [a]

[a] European Commission – DG Joint Research Centre, Via E. Fermi 2749, 21027 Ispra (VA), Italy

[b] formerly, European Commission – DG Joint Research Centre, Via E. Fermi 2749, 21027 Ispra (VA), Italy

[c] Depatamento de Biologia & CESAM, Universidade de Aveiro, Portugal

Biointerphases, Volume 11 (4), 16 December 2016
doi: 10.1116/1.4972112

6.1. Abstract

The detection and quantification of nanoparticles is a complex issue due to the need to combine "classical" identification and quantification of the constituent material, with the accurate determination of the size of submicrometer objects, usually well below the optical diffraction limit. In this work, the authors show that one of the most used analytical methods for silver nanoparticles, asymmetric flow field-flow fractionation, can be strongly influenced by the presence of dissolved organic matter (such as alginate) and lead to potentially misleading results. The authors explain the anomalies in the separation process and show a very general way forward based on the combination of size separation and size measurement techniques. This combination of techniques results in more robust AF4-based methods for the sizing of silver nanoparticles in environmental conditions and could be generally applied to the sizing of nanoparticles in complex matrices.

6.2. Introduction

Nanotechnology-based products are increasingly being available to consumers in different application areas, ranging from paint and inks to cosmetics and medicines. In particular, silver nanoparticles (AgNP) are used in consumer products due to their antimicrobial properties [1]. Products containing silver nanoparticles have been shown to release AgNP during their normal use [2,3] and ultimately end up in the environment. Nanoparticles can be difficult to characterize due to the need to both identify (and quantify) the constituent material(s) and to measure their size, usually well below the optical diffraction limit. Due to the increased relevance of nanotechnology-based products on the market, the European Commission has proposed a definition of what constitutes a "nanomaterial." This definition is based on the determination of the number-based particle size distribution (PSD) [4]. The determination of the particle size distribution of nanometer sized objects is even more difficult when measuring engineered nanoparticles in complex matrices [5] and especially nanoparticles embedded in environmental matrices that may contain several other ingredients such as dissolved organic matter.

Asymmetric flow field flow fractionation (AF4) is a separation technique which can fractionate liquid dispersed particles as a function of their size. The technique is widely used to in the separation and characterization of nanoparticles [6], especially in complex matrices such as environmental and biological matrices. In ideal cases, it is possible to obtain the particle size distribution of unknown samples by converting the AF4 retention time to size by either using the AF4 theory or by performing a size calibration with nanoparticle standards of known size [7,8] or to determine the PSD of AgNP commercial products in simple matrices [9].

Alginic acid, also called algin or alginate, is an industrially relevant anionic polysaccharide which is commonly found in the cell walls of brown algae and in biofilms produced by some bacteria. This nonbranched molecule can be used as a model of dissolved environmental organic matter which is known to play a critical role in the behavior and environmental fate of AgNP [10].

As shown before [11], the behavior of AgNP in water is modified in the presence of dissolved organic matter such alginic acid and humic acid, another common component of dissolved organic matter in water. It was found that these two materials, although chemically distinct, produced similar changes in particle behavior.

In this work, we show that the presence of alginic acid a) can strongly influence the AF4 separation of AgNP and lead to errors when attempting to size AgNP based on AF4 retention time. We address the origin of the phenomenon and we show a very general solution based on the combination of the AF4 separation with online size measurement.

6.3. Experimental setup and methodology

6.3.1 Reagents

High purity sucrose and dodecane were used in centrifugal liquid sedimentation (CLS) analysis and ammonium carbonate and NaOH for preparation of the AF4 eluent. All these reagents were sourced from Sigma-Aldrich and were of analytical grade purity or better. Low viscosity alginate sodium salt (Sigma-Aldrich) was used as a model for dissolved organic matter. The alginate stock solutions used were freshly prepared daily in MilliQ water (Millipore Advantage System, Merck Millipore) without further purification. Citrate stabilized AgNPs with nominal size of 60 nm and concentration of 20 µg/mL were purchased from Sigma-Aldrich and stored away from light at 4 _C in airtight glass vials.

6.3.2 Samples preparation

Aliquots of the AgNP stock solution were diluted in MilliQ water from the nominal concentration of 20 µg/ml to a final concentration of either 0.5 µg/mL for AF4 analysis or 5 µg/mL, for CLS measurements. For AgNPalginate complexed samples analysis, alginate was added to a solution containing 0.5 or 5 µg/mL AgNP, for CLS and AF4 analyses, respectively, at final concentrations ranging from 2 to 4 µg/mL. Alginate stock solution was prepared in MilliQ water at a concentration of 10 µg/mL and immediately mixed with the silver nanoparticles at concentrations ranging from 2 to 4 µg/mL. Mixtures were equilibrated at RT, with constant agitation for 1 h before analysis.

6.3.3 Instruments

The size of the as-supplied AgNPs and their complexes with alginate were measured with dynamic light scattering (DLS) and CLS instruments.

A Zetasizer model Nano-ZS instrument by Malvern was used to perform DLS particle size measurements. Batch DLS measurements were performed in PMMA disposable cuvettes using a backscatter reading angle (173˚) while measurements under flow conditions were done using a Hellma Quartz Suprasil 3mm flow-through cuvette adjusted to 3.90mm measurement position and attenuator of 11. The same instrument was used to measure the zeta potential of particle solution using disposable capillary cells. In all cases, the sample cell temperature was set to 25˚C.

CLS measurements were performed with a disk centrifuge photosedimentometer DC2400UHR by CPS Instruments, Inc. The instrument was operated at 22 000 rpm and samples were injected into an 8%–24% sucrose gradient.

6.3.4 Asymmetric flow field flow fractionation

AF4 analysis was performed in an AF2000 MT Multiflow FFF system with an on-line UV-Vis detector (Postnova Analytics). The chosen elution protocol was based on the method described by Geiss [7] for separation of different sized AgNP. The AF4 channel had a 280mm long separation channel, with a 350 µm spacer. A 10 kDa cut off membrane of regenerated cellulose and a 100 µL injection loop were used. Two types of elution buffer were used for AF4 analysis: low ionic strength solution of MQ water adjusted to pH 9.7 (50 µM NaOH) and higher ionic strength solutions containing various concentrations of ammonium carbonate (1–0.1mM) and pH 9.1. Elution buffers were freshly prepared in MilliQ water and degassed in an ultrasonic bath before use. All samples were analyzed under the following elution conditions: 0.5 mL/min injection flow; 0.2 mL/min tip flow for 5 min; 1.3 mL/min focus flow; and a linear decrease of the cross flow from 1 to 0.1 mL/min over 35 min. The UV detector wavelength was set to 430 nm, corresponding to the maximum of the surface plasmon resonance band for 60 nm AgNP.

6.4. Results and Discussion

To assess the impact of environmentally relevant materials on the AF4 separation profile of AgNP, we have studied the separation of AgNP in the presence of alginic acid. Alginic acid (Fig.1) is an anionic polysaccharide formed by units of 1–4 linked b-D mannuronic acid and a-L gluconic acid with a pKa around 3.5 and thus negatively charged at neutral pH. It is widely present in water environment and has a key role in the formation of biofilms that protect algae and bacteria from adverse environmental conditions [12].

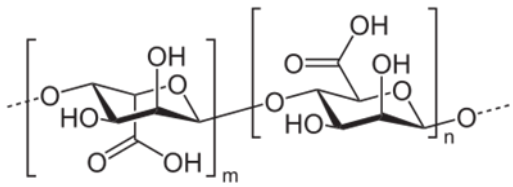

Figure 1. Chemical structure of alginate

When citrate stabilized AgNP are mixed with low amounts of alginic acid, they form stable complexes with no sign of aggregation, as shown by the lack of any large aggregation peak in the DLS data measured in batch mode [Fig. 2(b)]. Figure 2(a) shows the CLS data for AgNP free and in the presence of increasing amounts of alginic acid.

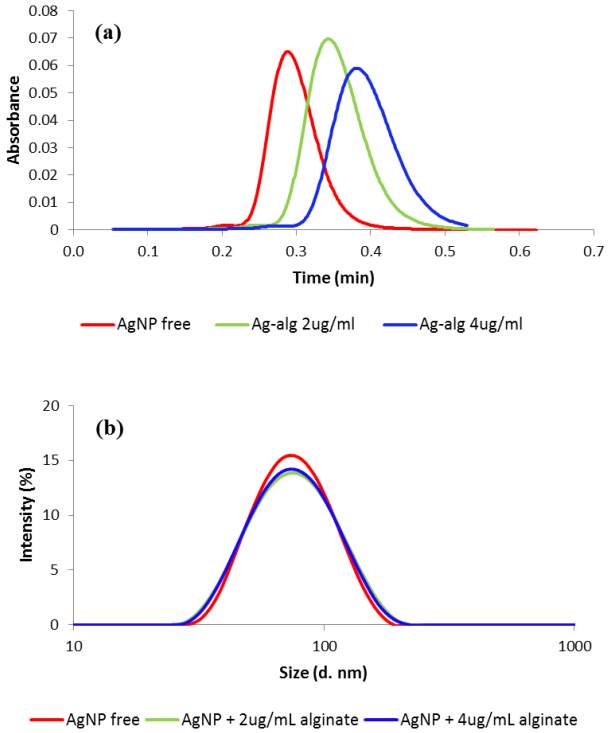

Figure 2. Characterization of AgNP-alginate complexes. (a) CLS spectra for 60nm AgNP, free (red), incubated with 2 µg/mL of alginic acid (green), and 4 µg/mL alginic acid (blue). (b) DLS data of the same samples.

The CLS data shown in Fig. 2(a) report the detector signal intensity versus time needed for each sample to reach the detector under the influence of the centrifugal field. These raw data are usually converted to the "standard" intensity versus size plot [13] (shown in supplementary material, Fig. S1) [18], provided that the density of the sample is known. As it is evident from Fig. 2(a), the time needed for AgNP-alginate samples to reach the detector is longer than that of free AgNP. In addition, the CLS peaks of AgNP-alginate samples have a slightly wider distribution when compared to free AgNP. In centrifugal liquid sedimentation, the movement of particles inside the centrifugal field depends (in first approximation) on the particle size and density. Thus, the increased time needed to reach the detector for the AgNP-alginate samples can be due to a decrease in the size and/or in the density of the particles.

The dynamic light scattering measurements of the different samples are shown in Fig. 2(b) and Table S1 (supplementary material). The data indicate that the size of AgNPalginate samples are indistinguishable (in the experimental error typical of batch-mode DLS) from the free AgNP and there are no large aggregates. In fact, the DLS intensity size distribution is extremely sensitive to large particles and the presence of even 1% large agglomerates would

result in a clear peak in the DLS particle size distribution. We also measured the zeta (ζ) potential of the different samples to check if the addition of the alginic acid changed the stability of silver nanoparticles colloid suspension. The results (reported in Table S2, supplementary material) show that the f-potential of AgNP-alginate samples are highly negatively charged (-50 mV and -48 mV following the addition of 2 μg/mL and 4μg/mL of alginate, respectively), thus confirming the colloidal stability of the systems.

The CLS data indicate the presence of an alginate layer around silver nanoparticles, thus forming AgNP-alginate complexes. In fact, the size of AgNP-alginate sample does not significantly change (AF4-DLS data of Fig. 4 suggest only a very small size increase) compared to free AgNP, while the layer of alginic acid (density 0.9976 g/mL) lowers the overall density of the AgNP-alginate complex. Thus, the lower density particles need longer time to reach the CLS detector [Fig. 2(a)].

Flow field flow fractionation can very efficiently separate complex mixtures of nanoparticles and the retention time from the AF4 separation channel can be used to estimate the size of the different components of polydispersed samples. Figure 3(a) shows the AF4 fractogram of a mixture of AgNP of 20, 40, 60, and 100 nm. The retention time (T_R = Tpeak – Tvoid) of each particle is a funtion of the size of the particles as shown in figure S2 (supplementary material). Fitting of the experimental data with power function of the type Size = a x T_R^b results in the following equation:

Eq. 1: Size = 0.595 x T_R1.637

With a R2 of 0.992. Where T_R is the retention time of each peak, and "Size" is the diameter of the particle.

The AF4 separation of free AgNP 60 nm [figure 3(b), black curve] gives a retention time of 16.9 min that, using Eq. 1, results in a measured size of 60.8 nm, well in agreement with expectations. Repeating the same separation for the AgNP-alginate gives a quite different AF4 fractogram [figure 3(b), red line]. Using Eq. 1 the measured retention time of 9.55 min translates to a size of 23.9 nm for the AgNP-alginate complex, which is much smaller than the size of 60 nm for the starting free AgNP.

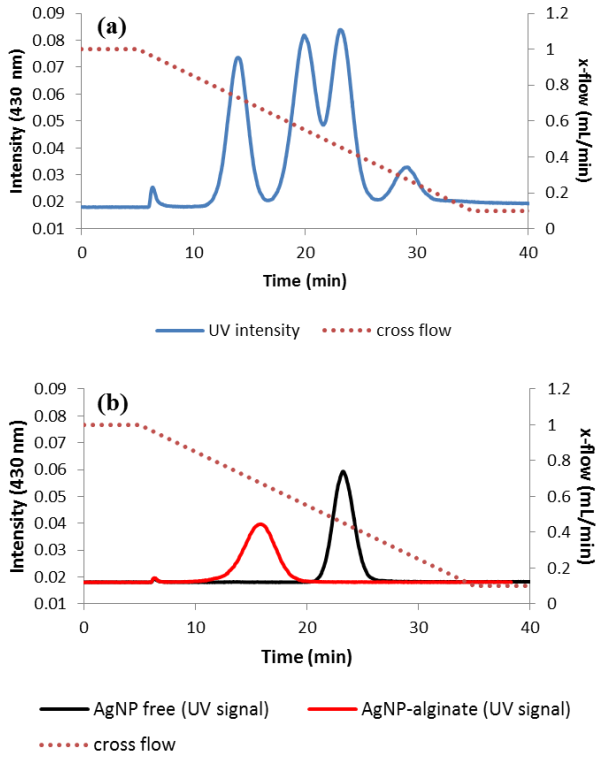

Figure 3. AF4 separation of AgNP and AgNP-alginate complexes. The cross flow program used is reported as a dotted red line on the right scale. (a) Mixture of AgNP 20, 40, 60, 100 nm. (b) AgNP 60 nm free (black) and AgNP – alginate sample with 5 µg/mL AgNP and 2 µg/mL alginate (red).

The smaller calculated size for AgNP-alginate complex could be due to AgNP oxidation and release of ionic silver with subsequent reduction in size (even if it seems unlikely) or to an anomalous AF4 separation process. In fact, there are reports in the literature that charge repulsive interaction of particles with one another and also with the AF4 semipermeable membrane lead to a decrease of the apparent hydrodynamic size [14].

An elegant and robust solution for the accurate measurement of the size of AgNP-alginate complex would be to couple the AF4 separation with an online size measurement technique. Two of the most used online systems for achieving this are multiangle light scattering (MALS) and DLS. Both techniques have advantages and disadvantages and when combined together, they also give additional information on the geometry of the particles (shape factor) in addition to their size [15]. In the case of silver nanoparticles only DLS can be used to sizing, as MALS does not give correct results in the case of plasmonic systems such as silver and gold nanoparticles.

Figure 4 shows the results of AF4-DLS measurement for free AgNP and AgNP-alginate complexes obtained by coupling the output from the AF4 system with a flow cell in the DLS instrument. The online measurement of the hydrodynamic diameter (Z-average, measured at the maximum intensity of the UV-Vis detector) gives a value of 71 nm for the AgNP-alginate complex [Fig. 4(b)] and 69 nm for free AgNP [Fig. 4(a)]. The increase in size from the free AgNP to the AgNP-alginate sample is in the experimental error of the AF4-DLS measurements.

The results show that the size of the AgNP complex is much closer to the size of the free AgNP than the results obtained by using the AF4 exit time and suggest that the AF4 separation is somehow distorted by charge repulsion forces.

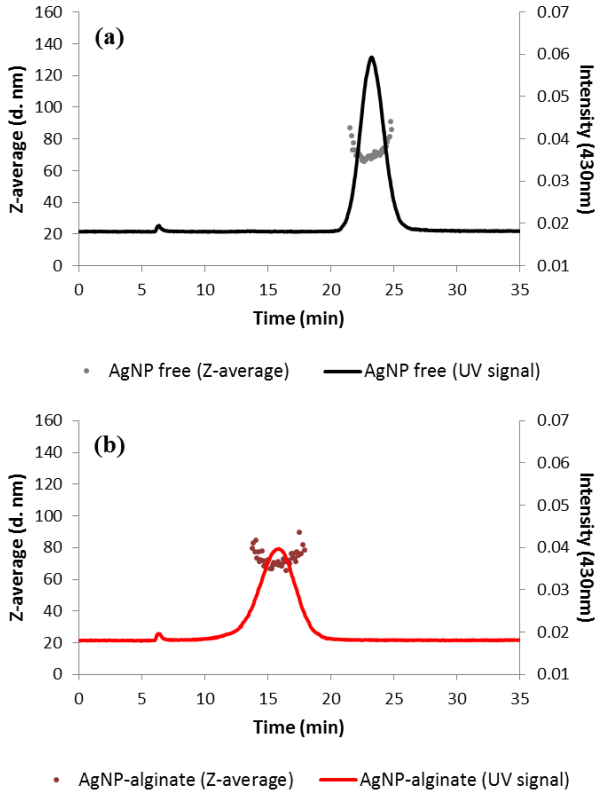

Figure 4. AF4-DLS fractograms of (a) AgNP free and (b) AgNP-alginate. The intensity of the detector at 430 nm is reported on the right hand scale and the Z-average of the particles on the left scale for the AgNP-alginate complex (500 ng/mL Ag : 2 µg/mL alginate), in red, and the free AgNP (500 ng/mL), in black.

The results show that the AF4-DLS measurements can provide the accurate size (and even the particle size distribution) for silver nanoparticles in complex with alginate without any major optimization in the experimental parameters used for the AF4 separation. This method does not require any calibration with well-defined size standards and is independent of the different electrostatic forces that can affect the AF4 separation process when the nanoparticles surface is modified by either chemical functionalization, attachment of ligands (as in the above case with formation of AgNP-alginate complexes), or coating of the AF4 membrane (for example, by some components of environmental matrices). The main limitation of the AF4-DLS method is related to the sensitivity of the DLS online detector. Due to the dependency of the DLS scattering intensity on the sixth power of the particle diameter, small particles tend to give quite lower intensities compared to larger ones, and thus, the size measurement with online DLS can become unreliable.

To experimentally reduce the charge repulsion forces leading to the anomalous AF4 separation, we repeated some of the AF4 measurements with different elution buffers. In fact, one of the most general approaches for reducing electrostatic forces between analytes and charged membranes is to increase the ionic strength by the addition of salts or buffers [8,16,17]. We have tested this by using different concentrations of ammonium carbonate, which provides both a basic pH between 8.5 and 9.0 and high ionic strength. Figure 5 shows the results of the AF4 separation of the AgNP-alginate sample in the presence of increasing concentrations of ammonium carbonate in the carrier solvent. As shown previously, with no ammonium carbonate in the solvent, AgNP-alginate complex exits much earlier (figure 5, blue trace) than expected (figure 5, free AgNP, cyan trace).

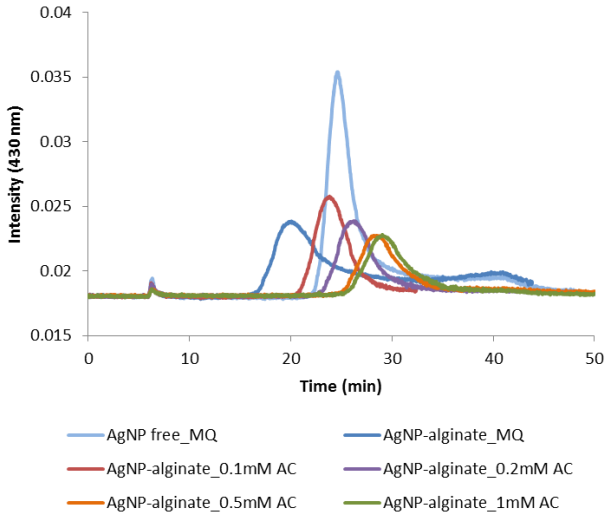

Figure 5. AF4 fractograms of AgNP free (cyan) and AgNP–alginate complexes with variable concentrations of ammonium carbonate: 0 (dark blue), 0.1mM (red), 0.2 mM (violet), 0.5 mM (orange), and 1 mM (green).

When some ionic buffer is added the retention time from the AF4 tends to be much closer to that obtained for free AgNP; with 0.2 mM carbonate buffer the retention time of free AgNP and AgNP-alginate samples are almost the same. Higher concentrations of carbonate lead to an increase of the retention time and probably cause also some additional loss of sample during the AF4 separation as shown by the reduced area of the AF4 peaks (figure 5, orange and green traces for 0.5 and 1 mM carbonate).

6.5. Conclusions

Flow field flow fractionation is a very powerful and flexible method to separate nanoparticles and it can be used to estimate the size of silver nanoparticles using calibration techniques with samples of known size. Our results show that this method has to be used with the great care when the calibrating nanoparticles have different surface properties. In fact, the formation of silver-NP–alginate complexes (in conditions mimicking environmentally relevant conditions) can lead to quite misleading results due to electrostatic repulsion forces. In particular, this is very important when silver nanoparticles form complexes with dissolved organic matter, such as alginic acid. Similar considerations will be probably also very important in the case of

AgNP functionalized with different ligands which may alter the surface properties of the particles which, in turn, modify the elution time by changing the interactions with the membrane.

The coupling of AF4 with a sizing technique, such as DLS, provides a more general and robust method for the sizing of AgNP in environmental conditions, as we have shown for AgNP-alginate systems. The AF4-DLS method is quite general and easy to set up and should be possible to use it for different types of nanoparticles forming complexes with a wide range of molecules.

6.6. Supplementary material

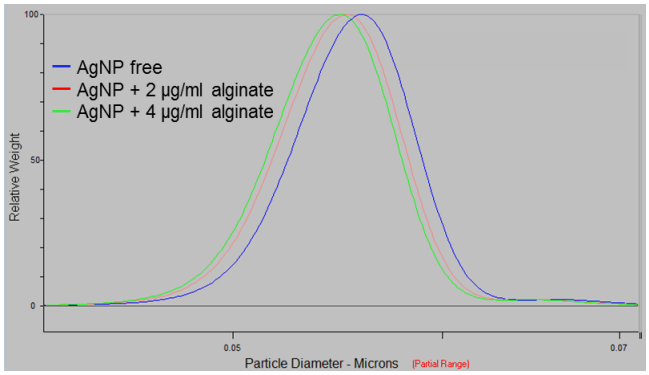

Figure S1. "Standard" CLS data plotting showing the sample size distribution (as diameter) *v.s* signal intensity (plotted in relative weight).

Table S1. Size determination (Z-average) of AgNP samples by dynamic light scattering with respective polydispersive index (PDI).

Sample	Z-average	PDI
AgNP free	69	0.13
AgNP + 2ug/mL alginate	68	0.15
AgNP + 4ug/mL alginate	68	0.14

Table S2. Zeta potential of the mixture AgNP-alginic acid, measured with a Malvern instrument.

Sample	ζ-potential (mV)
AgNP free	-50
AgNP + 2µg/ml alginate	-50
AgNP + 3µg/ml alginate	-50
AgNP + 4µg/ml alginate	-48
4µg/ml alginate	-11

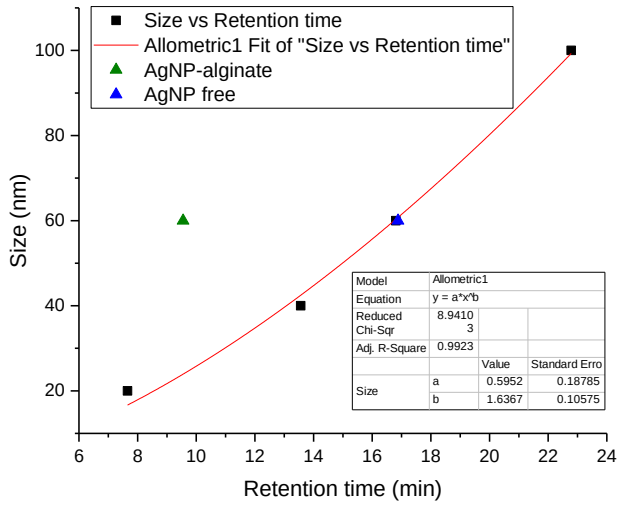

Figure S2. Plot of nominal size *v.s* AF4 retention time for AgNP mixture of 20, 40, 60 and 100 nm (black square bullets) and corresponding non-linear fitting (red line). Retention time for 60 nm AgNP free (blue triangle) and AgNP-alginate complex (green triangle) were plotted on top of the fitted data.

6.7. References

1. C. Levard, E. M. Hotze, G. V. Lowry and G. E. Brown, Environmental Science & Technology 46(13): 6900-6914 (2012).
2. T. M. Benn and P. Westerhoff, Environmental Science & Technology 42(11): 4133-4139 (2008).

3. R. Kaegi, B. Sinnet, S. Zuleeg, H. Hagendorfer, E. Mueller, R. Vonbank, M. Boller and M. Burkhardt, Environmental Pollution 158(9): 2900-2905 (2010).
4. Regulation (EU) No 1169/2011 of the European Parliament and of the Council (25 October 2011).
5. L. Calzolai, D. Gilliland and F. Rossi, Food Additives & Contaminants: Part A 29(8): 1183-1193 (2012).
6. L. Calzolai, D. Gilliland, C. P. Garcia and F. Rossi, Journal of Chromatography A 1218(27): 4234-4239 (2011).
7. O. Geiss, C. Cascio, D. Gilliland, F. Franchini and J. Barrero-Moreno, Journal of Chromatography A 1321(0): 100-108 (2013).
8. K. Loeschner, J. Navratilova, S. Legros, S. Wagner, R. Grombe, J. Snell, F. von der Kammer and E. H. Larsen, Journal of Chromatography A 1272(0): 116-125 (2013).
9. C. Cascio, O. Geiss, F. Franchini, I. Ojea-Jimenez, F. Rossi, D. Gilliland and L. Calzolai, Journal of Analytical Atomic Spectrometry 30(6): 1255-1265 (2015).
10. G. R. Aiken, H. Hsu-Kim and J. N. Ryan, Environmental Science & Technology 45(8): 3196-3201 (2011).
11. D. C. António, C. Cascio, Ž. Jakšić, D. Jurašin, D. M. Lyons, A. J. A. Nogueira, F. Rossi and L. Calzolai, Marine Environmental Research 111: 162-169 (2015).
12. Boyd and A. M. Chakrabarty, Journal of Industrial Microbiology 15(3): 162-168 (1995).
13. R. Capomaccio, I. Ojea Jimenez, P. Colpo, D. Gilliland, G. Ceccone, F. Rossi and L. Calzolai, Nanoscale 7(42): 17653-17657 (2015).
14. N. M. Thang, H. Geckeis, J. I. Kim and H. P. Beck, Colloids and Surfaces A: Physicochemical and Engineering Aspects 181(1–3): 289-301 (2001).
15. P. Iavicoli, P. Urbán, A. Bella, M. G. Ryadnov, F. Rossi and L. Calzolai, Journal of Chromatography A 1422: 260-269 (2015).
16. K.-G. Wahlund, Journal of Chromatography A 1287(0): 97-112 (2013).
17. J. R. Runyon, M. Ulmius and L. Nilsson, Colloids and Surfaces A: Physicochemical and Engineering Aspects 442(0): 25-33 (2014).
18. See supplementary material at http://dx.doi.org/10.1116/1.4972112 for CLS plot, DLS data in batch mode and zeta potential values.

7. Chapter V

Assessing silver nanoparticles behaviour in artificial seawater by mean of AF4 and spICP-MS

D.C. António[ab], C.Cascio [1a], Ž. Jakšić[c], D. Jurašin[d], D. M. Lyons[c], A. J. A. Nogueira[b], F. Rossi[a], L. Calzolai[a]

[a]European Commission - Joint Research Centre, Institute for Health and Consumer Protection, T.P. 203, Via E. Fermi 2749, 21027 Ispra (VA), Italy

[b]Departamento de Biologia & CESAM, Universidade de Aveiro, Aveiro, Portugal

[c]Center for Marine Research, Ruđer Bošković Institute, Giordano Paliage 5, 52210 Rovinj, Croatia

[d]Division of Physical Chemistry, Ruđer Bošković Institute, Bijenička cesta 54, 10000 Zagreb, Croatia

[1]Present address: RIKILT Wageningen UR, Institute of Food Safety, P.O. Box 230, NL-6700 AE Wageningen, The Netherlands

Marine Environmental Research, Volume 111, Pages 162–169, October 2015
doi: 10.1016/j.marenvres.2015.05.006

7.1. Abstract

The use of nanotechnology-based products is constantly increasing and there are concerns about the fate and effect on the aquatic environment of antimicrobial products such as silver nanoparticles (AgNP). By combining different characterization techniques (asymmetric flow field-flow fractionation, single particle ICP-MS, UV-Vis) we show that it is possible to assess in detail the agglomeration process of AgNP in artificial seawater. In particular we show that the presence of alginate or humic acid differentially affects the kinetic of the agglomeration process. This study provides an experimental methodology for the in-depth analysis of the fate and behaviour of silver nanoparticles in the aquatic environment.

7.2. Introduction

The production and use of nanotechnology-based products is constantly increasing in different market sectors. Silver nanoparticles (AgNP) are widely used nanomaterials due to the well-known antimicrobial properties of silver. Silver nanoparticles can be found in a variety of consumer products: from medical devices or wound bandages, to water purification systems, to socks and textiles. It is estimated that AgNP have a median worldwide production of around 55 tons per year [1].

The increased use of these products with antimicrobial properties and their poorly understood behaviour and toxicity may pose a threat to human health and environment. The potential impact of silver-containing products is a concern extensively debated in literature both in the field of human health [2, 3] and environment [4, 5]. Overall, direct exposure effects are only part of the potential nano-silver toxicity. In fact, during product use and end-of-life phase AgNP may be released into waste water systems and they could potentially reach the different aquatic environments. Several works have attempted to determine the stability of AgNP in natural systems. Kaegi's group [6], for instance, showed that AgNP are quickly converted to insoluble chemical forms (such as Ag_2S) in waste water treatment plants. However, silver speciation depends also on the composition of the nanoparticles surface and not every environment will be as sulphur rich as water treatment plants; thus the persistence of AgNP in the aquatic environment and their potential impact must be taken into account. Light, temperature, ionic strength, oxygenation, total surface area and presence of organic matter are some of the factors that can affect both AgNP agglomeration, aggregation and oxidative release of Ag^+ ions, influencing AgNP toxic potential [7-10].

Dissolved organic matter (DOM) is expected to play an important role on AgNP behaviour in the environment as it could form a more or less stable corona around the nanoparticles, thus potentially changing the chemical properties of the nanoparticle surface. For example, it has been shown that AgNP size distribution can vary in the presence of humic substances [11]. In addition, alginate has been shown to influence nanoparticles agglomeration kinetics on a concentration-dependent manner [12]. Humic acid and alginate are two components of DOM, which can be present in the aquatic environment at variable concentrations depending on factors such as algal bloom or anthropogenic impairment, due to soil leaching [13].

The availability of methods for the proper detection and measurement of NP is a key aspect for understanding the fate and behaviour of NP in the environment. Several techniques are available that can provide information on the physico-chemical characteristics of AgNP, but

nanoparticles need to be evaluated and analysed with extreme care [14-16]. In this study we focused on evaluating the behaviour of AgNP entering coastal water systems. In order to assess the behaviour of AgNP in the marine environment we have studied the agglomeration properties of AgNP in artificial seawater (ASW) in the presence of dissolved organic matter as a function of time. Changes related to size, and AgNP stability in dispersion, were followed by UV-Vis spectroscopy, dynamic light scattering (DLS), centrifugal liquid sedimentation (CLS), asymmetric flow field flow fractionation (AF4), and single particle inductive coupled plasma mass spectrometry (spICP-MS). UV-Vis spectroscopy is used to evaluate the agglomeration process of metallic nanoparticles, such as AgNP, exploiting their specific surface plasmon resonance properties [17, 18]. DLS has been widely employed to assess the stability of colloidal systems in solution [19, 20] However, nanoparticle separation, by means of flow field-flow fractionation, and sizing by spICP-MS, have been shown to be the most sensitive techniques available for AgNP characterization [21]. By using a combination of those techniques we have shown that it is possible to accurately follow the agglomeration process of AgNP as a function of water salinity, temperature and the presence of organic matter.

7.3. Materials and Methods

7.3.1 Reagents

Citrate stabilized silver nanoparticles (nominal size 60±4 nm and 0.02±5% mg/mL concentration) were purchased from Sigma-Aldrich. AgNP were handled under nitrogen flow, stored at 4°C and protected from exposure to natural light. NIST gold nanoparticles RM8013 (with a declared TEM diameter of 56.0±0.5 nm and Au mass fraction of 51.86 ±0.64 µg/g) were used for the determination of transport efficiency into the plasma for spICP-MS as in [22]. Silver stock for ICP-MS was 1000 mg/L in 2% nitric acid (Absolute Standards, INC., Hamden USA). De-ionized ultrapure water (DI) from a Millipore Advantage system (Merck Millipore) was used in this study. Artificial seawater was prepared by dissolution of sea salts (Sigma-Aldrich) in de-ionized water. Sea salts are an artificial salt mixture resembling the composition of oceanic dissolved salts, with a chloride content of 19.3 g/L. Low viscosity sodium alginate from brown algae and humic acid sodium salt (Sigma-Aldrich) were used as

organic matter. Alginate and humic acid were freshly prepared before each experiment by dispersing them in ultrapure de-ionized water before mixing with the other components of the final samples, without further purification steps. Test samples were kept in closed vials. For CLS analysis, sucrose purchased from Sigma-Aldrich was used to prepare a sucrose gradient, capped with dodecane (CPS Instruments).

7.3.2 Instruments

For the kinetic study the following instruments were used: two spectrometers, model Thermo Nicolet Evolution 300 (Thermo Fisher Scientific, Inc.) and UV-1800 (Shimadzu Corp.); Malvern Zetasizer Nano-ZS (Malvern Instruments), and disc centrifuge photosedimentometer DC2400UHR (CPS Instruments). Long term incubated samples were analysed by an Agilent 7700x Inductively Coupled Plasma-Mass Spectrometry and an AF2000 MT Multiflow FFF system with an on-line connected UV-Vis detector (Postnova Analytics).

7.3.2.1 Incubations and kinetics studies

AgNP were tested at a constant nominal concentration of 0.5 mg/L dispersed in ultrapure or in ASW, exposed to natural or artificial (13 hours light and 11 hours dark) light cycle and with constant shaking (100 rpm). Incubation was performed in parallel at 14ºC and room temperature, at close to zero ionic strength and with 3.2% w/v sea salts in de-ionized water. Finally, the presence of 2 mg/L alginate or humic acid (HA) in the system, with and without prior equilibration time, was tested. Equilibration consisted or incubation of AgNP with alginate or humic acid for 2 days in non-salty conditions prior to final dilution.

Samples were collected at various time points during the incubation process for determination of: i) localised surface plasmon resonance (LSPR) band; ii) particles size distribution; and iii) particles average size and polydispersivity index.

LSPR was determined based on the full absorption spectra, in the 300-700 nm wavelength range, by UV-Vis spectrometry. Quartz cuvettes were used to minimize unspecific signal. CLS gives information regarding the particle hydrodynamic radius, based on sample density. The instrument was operated at 22000prm and samples were injected into an 8-24% sucrose gradient. DLS measurements were performed at a backscatter angle of 173º in PMMA

cuvettes. UV-Vis spectroscopy data fitting was performed with *Origin Pro 7.5* software and *Visual MINTEQ* (KTH, Sweden), an open source software, was used to evaluate the dissolution rate of silver species in both systems, at low and high ionic strength.
After 2 days incubation, sample aliquots were taken for analysis by mean of i) AF4/UV-Vis and ii) single particles ICP-MS for size evaluation.

7.3.2.2 Asymmetric Flow Field Flow Fractionation

Samples were analyzed on an AF4 system (Postnova Analytics) coupled to a UV detector, based on the method previously optimized for size fractionation of citrate stabilized AgNP from 20 up to100 nm described by Geiss [23], varying the injected volume in order to compensate for the low concentration. Briefly, a 280 mm long separation channel, with a 350 µm spacer and a 10 kDa cut off membrane of regenerated cellulose and a 100 µL injection loop were used. The semipermeable membrane allows the flow of the solvent of the cross flow, while retaining particles. The selected pore size allows the particles separation by hydrodynamic size with minimal particles retention/loss.
Degassed water, with pH adjusted to 9.7 by addition of NaOH, was used as carrier and freshly prepared each day. All samples were analysed under the following elution conditions: 0.5 mL/min injection flow; 0.2 mL/min tip flow for 5 min; 1.3 mL/min focus flow; and a linear decrease of the cross flow from 1 to 0.1 mL/min over 35 min. The UV detector wavelength was set to 430 nm, corresponding to the maximum of the LSPR band for 60 nm AgNP.

7.3.2.3 spICP-MS analysis

Single particle ICP-MS is an application of ICP-MS that allows the sizing of silver nanoparticles generally bigger than 20nm. The methods used for spICP-MS analysis was described by RIKILT and details can be found in [24]. An ICP-MS equipped with a micromist nebuliser, a quartz Scott spray chamber, quartz torch and platinum cones was used. The ICP-MS was operated in Time Resolved Analysis mode with integration time of 3 ms. The sample was introduced via a peristaltic pump, and the flow of sample introduction was monitored all along the run with a flow meter. Monitored signals were 107 for Ag and 197 for Au. A typical scan consisted of 18750 data points. Plasma transport efficiency was determined by using 60 nm AuNP (RM8013) NIST at a concentration of 24 ng/L as described in [22]. ICP-MS was

tuned with our standard procedure; silver ionic calibration was run along with samples (6 points in the range 0-1 µg/L) in single particle mode. Sample preparation, consisting of a number of serial dilutions in ultrapure water was undertaken gravimetrically. Intensity variations over the time were recorded and final data exported as counts per seconds *versus* time. Exported .csv files were processed using the available Single Particle Calculation Tool developed by RIKILT (http://www.wageningenur.nl/en/show/Single-Particle-Calculation-tool.htm). Quality control calibration curve was run twice during the analysis and ultrapure water sample was run in between each sample in order to monitor the presence of memory effect and baseline drift. Moreover 60 nm AgNP citrate stabilised (Sigma Aldrich) were analysed every day to monitor sizing performance. Samples were analysed in duplicate.

7.4. Results and Discussion

Silver nanoparticles of a nominal size of 60 nm were preliminary characterized by TEM, CLS, DLS, UV-Vis spectroscopy and ICP-MS. The total silver concentration was 16.0 ± 0.4 mg/L (as determined by ICP-MS) and indicates a lower total content of silver with respect to the declared value of 20 mg/L. The starting material was shown to be monodispersed, with a diameter of 53.4±6.6 nm (measured by CLS), a hydrodynamic diameter (measured by DLS) of 67 nm and polydispersivity index of 0.12, and a median diameter of 55 nm as measured by spICP-MS (see Figure 2.A). Compared to the producer measured diameter (by TEM) of 60 ±4 nm, these results indicate that the results obtained from CLS and spICP-MS tend to slightly underestimate the size, while DLS tends to overestimate it. Discrepancies in the determined diameter by DLS and CLS are consistent with the inherent measurement principle of the two techniques and have been already reported and explained elsewhere (Cascio, Gilliland et al. 2014). Further details are reported in Figure S1 and Table S1 of supplementary information.

Overall, these results indicate that even if the four different techniques used different principles and measure somewhat different sizes (for example the hydrodynamic diameter in solution for DLS versus the diameter in vacuum for TEM) their results can be compared in the case of monodispersed nanoparticle samples.

The stability of silver nanoparticles in the presence of dissolved organic matter (DOM) was first analysed in salt free water. To this end the model DOM alginate was mixed with AgNP and incubated for two days using temperature, photoperiod and temperature similar to those

used for culturing marine organisms (see materials and methods). Figure 1 shows the results of the AF4/UV-Vis separation and analysis for the free AgNP (Figure 1.A) and AgNP mixed with alginate at 2 mg/L concentration (Figure 1.B) at time zero and after two days of incubation in de-ionized water.

The data shows that both free and alginate-complexed AgNP are very stable in de-ionized water over 2 days of incubation in environmental condition without formation of agglomerates or larger particles. In fact, the AF4 technique separates particles based on their size so an increase in size and/or the formation of larger agglomerates should increase the retention time from the separation channel. As shown in Figure 1.B the retention time of AgNP-alginate complexes (at both zero time and 2 days of incubation) is shorter than that of free AgNP. A shorter retention time would imply (under normal AF4 separation conditions) a smaller size for AgNP-alginate complexes. On the other hand, spICP-MS and CPS data (Figure 2) and DLS data (Figure 6), for free AgNP and AgNP-alginate samples in de-ionized water indicate that size distribution of the complex does not change compared to the free particles. This apparent paradox can be explained by a modified electrostatic interaction of the highly negatively charged AgNP-alginate complex with the semipermeable membrane (also negatively charged) of the AF4 separation cartridge due to the presence of alginate layer. Variation on retention times due to electrostatic repulsion has been recently demonstrated for PVP-stabilized silver nanoparticles [25].

A clear evidence of alginate coating the AgNP can be seen in the measured Z-potential of the particles that changes from -59 mV for the AgNP to -69 mV for the AgNP-alginate sample (data not shown). This increase in negative charge indicates that the highly negatively-charged alginate interacts with AgNP and could explain the reduction of AF4 retention time. In fact, the increased electrostatic repulsion between the negatively charged membrane and the highly negatively charged complex would lead to a reduction of the retention time.

The data on the AF4 separation of AgNP-alginate at different incubation times (Figure 1.B) also suggest that the interaction of alginate with silver nanoparticles is a quite slow kinetic process and this effect should be taken into consideration in the experimental design.

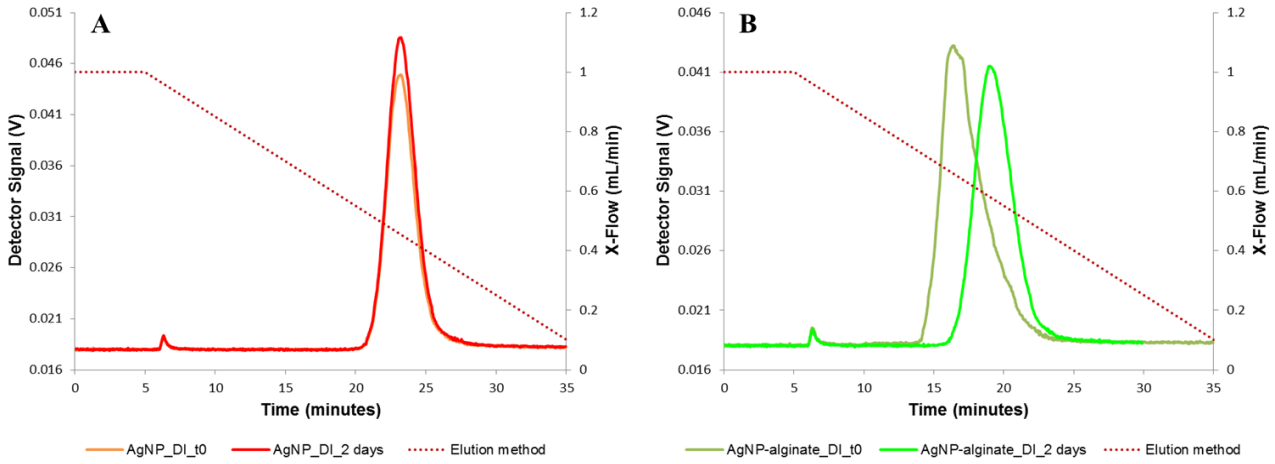

Figure 1. UV-Vis signal of A) free AgNP and B) AgNP-alginate complex at time zero and after two days of incubation in de-ionized water (DI), acquired by AF4/UV-Vis analysis (UV-Vis detector signal at 430 nm on left hand scale). Red dashed line represents the elution method used (applied cross-flow on the secondary y scale).

Single particle ICP-MS is able to determine PSD of metallic nanoparticles based on number; Figure 2.A-B shows such measurements for free and complex AgNP after 2 days incubation in de-ionized water. SpICP-MS by its nature is able to essentially size only the metallic core of the AgNP-alginate complex and therefore it does not provide evidence of alterations of the size of AgNP in the presence of alginate. The data indicate that both samples are quite stable over 2 days of incubation with no difference between the free AgNP and the ones in complex with alginate; distributions had a median of 55 nm that fits quite well with the value of 52 nm of the CLS number-based distribution (Figure 2.C).

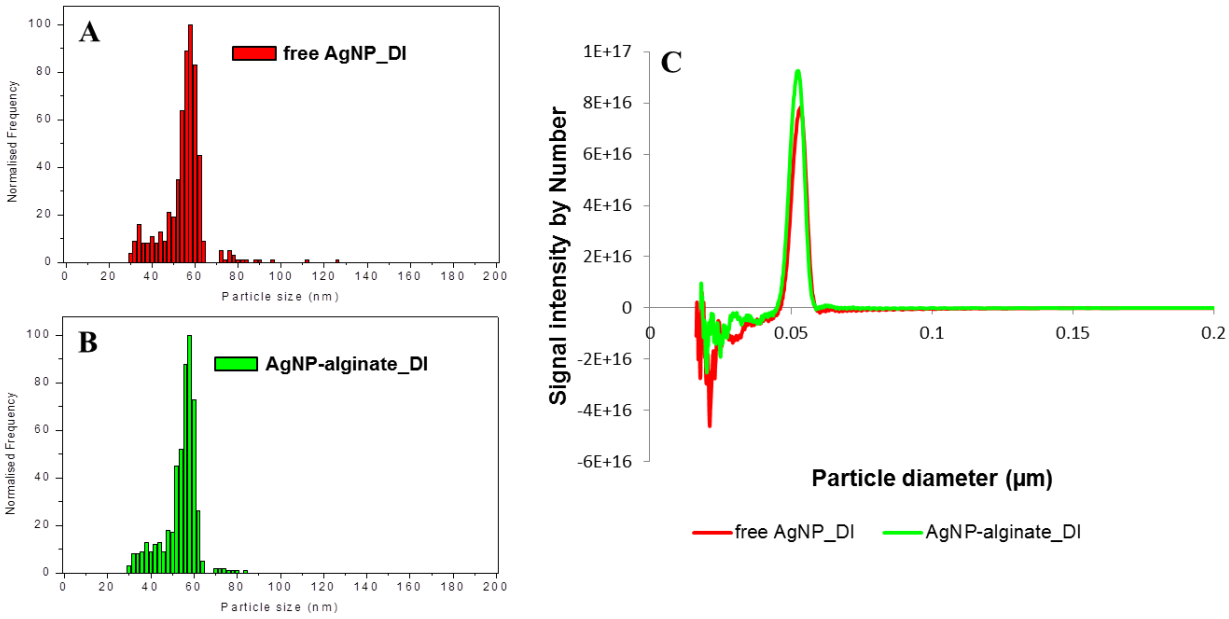

Figure 2. AgNP size distribution of A) free AgNP and B) AgNP-alginate complex after 2 days incubation at 14°C in de-ionized water (DI), measured by spICP-MS. C) Particle distribution, by number, of free AgNP (red) and AgNP-alginate complex (green), corresponding to the data points of A and B, acquired by centrifugal liquid sedimentation.

While the tested particles were very stable in de-ionized water, their stability in salt water could be quite different, where the high ionic strength could severely destabilize the colloidal system. To test stability and agglomeration behaviour of AgNP in salt water and the effect of alginate, AgNP samples were incubated in ASW with and without alginate over 2 days. In most of the tested conditions, AgNP could not be detected after two days of incubation in ASW. The direct mixture of the sample constituents or pre-incubating the particles with alginate has no effect on the measured signal.

AgNP were detected only when mixed with alginate and kept at 14°C, as shown in Figure 3.A. Even in this case (AgNP mixed with alginate, in ASW for 2 days at 14°C) the AF4 elugram shows a weak peak exiting the separation channel at very low cross-flow rates, suggesting the presence of low amounts of AgNP that are much larger than the original ones. These initial results suggest that AgNP agglomerate and sediment in salt water and that the presence of alginate can help in stabilizing the colloidal system. Single particle ICP-MS analysis confirmed the presence of residual and polydispersed AgNP for the samples where AF4/UV-Vis signal was detectable (data not shown). Because of the precipitation process, the number of particles in dispersion decreased as compared to the original samples along with a

much wider particle size distribution ranging from 30 nm, up to 120 nm and with a median value of 58 nm.

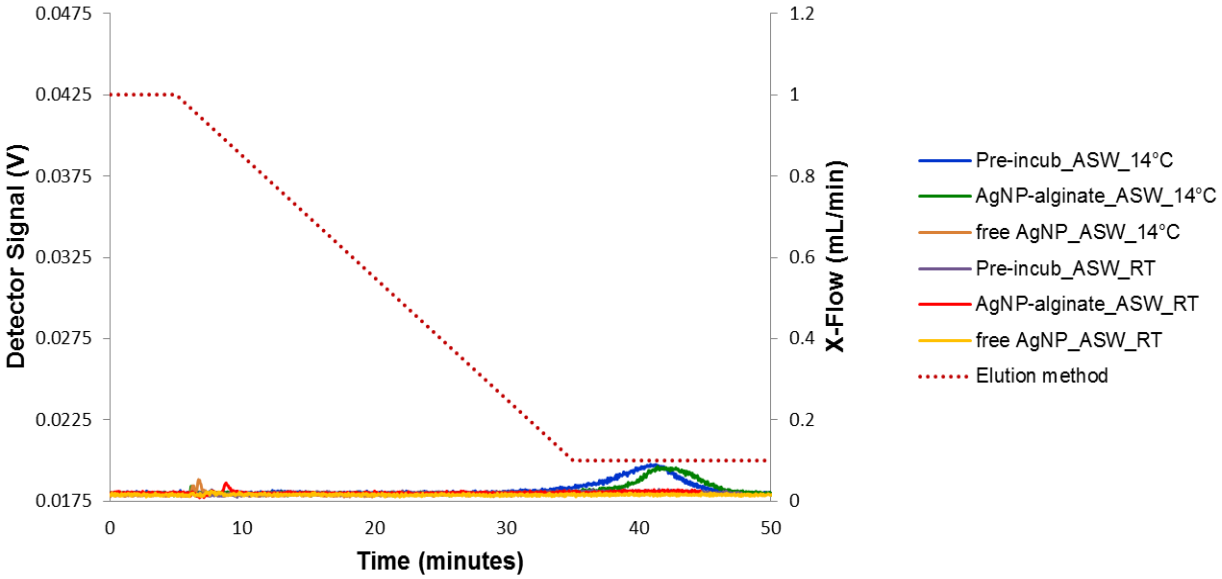

Figure 3. AF4-UV-Vis signal of free AgNP and AgNP-alginate samples incubated 2 days in ASW, either with pre-incubation (Pre-incub_ASW) or without (AgNP-alginate_ASW), at room temperature (RT) or at 14°C. Data were acquired by AF4/UV-Vis analysis. Red dashed line represents the cross flow elution profile used.

To study in more detail the kinetic of the agglomeration process, we took advantage of the localised surface plasmon resonance of silver nanoparticles. AgNP have a characteristic band in the visible region in the 400-450 nm wavelength range, whose intensity and wavelength maximum is concentration and size dependent. A typical spectrum of 60 nm AgNP is shown in the supplementary information (Figure S2), while bigger particles would shift the band to longer wavelengths and the surface plasma resonance band would eventually disappear for particles larger than around 120 nm. The measurement of the UV-Vis spectra is much faster than a complete AF4 run and thus allows the early steps of the agglomeration process to be followed. Figure 4 shows that AgNP (either free or in the presence of alginate) are quite stable in de-ionized water (as already concluded from the initial experiments using AF4 analysis after 2 days incubation, see Figure 1). On the contrary, AgNP in ASW tend to lose the LSPR band in just around 2 hours. In the case of AgNP in the presence of alginate there is

a reduction in the intensity of the LSPR band, but not a complete disappearance as in the case for free AgNP. This indicates that the presence of alginate slows down the agglomeration/precipitation process that takes place in ASW. Our data is in agreement with Delay's group study on AgNP destabilization process at increased ionic strength, where presence of NOM promoted NP coating and stabilization [26].

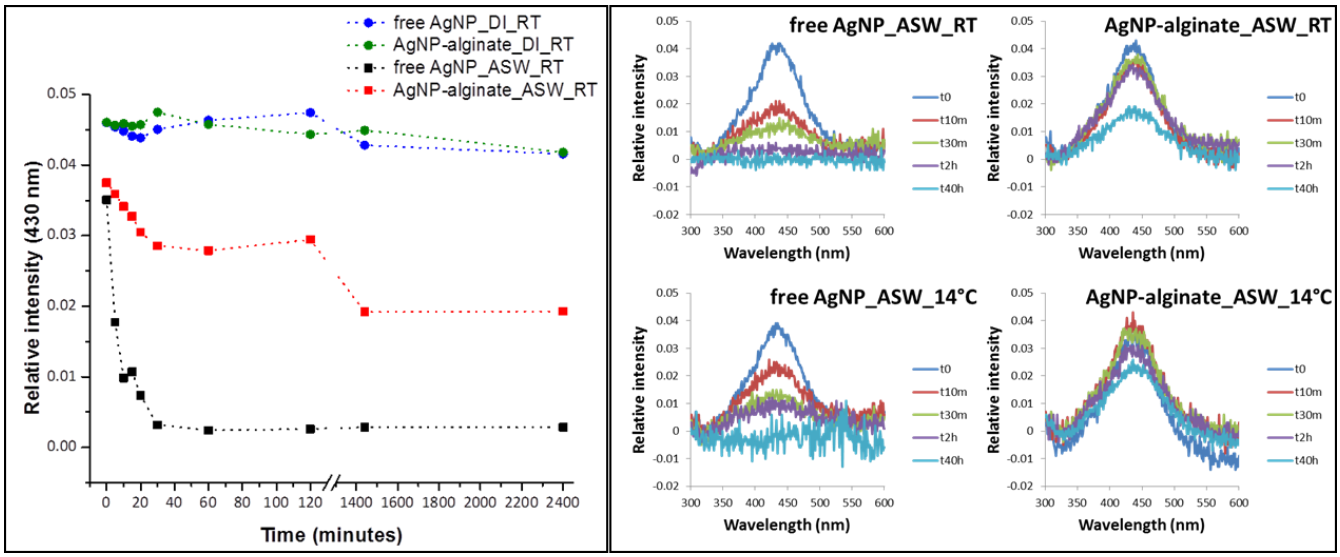

Figure 4. Left panel shows UV-Vis data plotted as relative intensity at 430 nm versus incubation time of free AgNP and AgNP-alginate complexed samples incubated in de-ionized and ASW, at room temperature (RT). Time is plotted on a nonlinear scale. Right panel shows a comparison of the UV-Vis spectra of free AgNP in ASW (left) and AgNP-alginate complex in ASW (right) over the 2 days, both at RT (top) and at 14°C (bottom).

The initial data of the agglomeration process (in the time scale from 0 to 60 minutes were fitted to a single exponential decay model $y = A_1 * e^{(-x/t1)} + y_0$ (Figure 5) with R^2 values of 0.96 for both free AgNP and AgNP-alginate system, with t_1 equal to 7±1 m^{-1} and 20±5 m^{-1}, respectively. The data clearly show that the presence of alginate slows down the agglomeration of silver nanoparticles in salt water. The time constants obtained above will depend on the exact composition of the dispersing media, but they could be useful for comparing the relative stability of AgNP with different functionalization or coating dispersed in the same specific media.

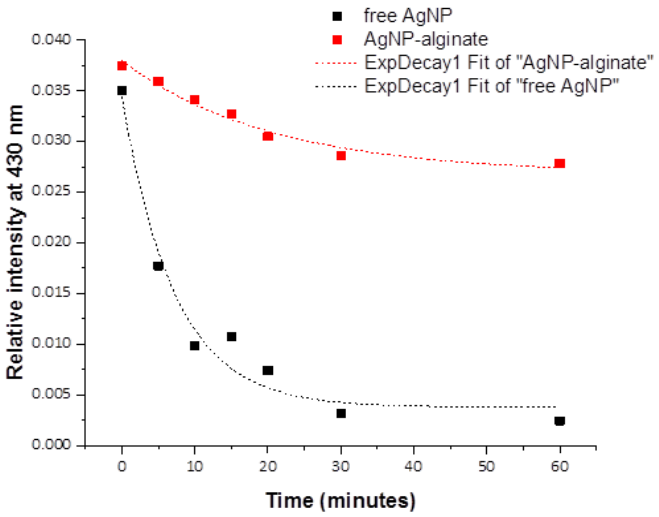

Figure 5. A) Relative signal intensity variation with time, at 430 nm, of free AgNP (black) and AgNP-alginate complexed sample (red), incubated at room temperature in ASW. Dashed lines show the exponential fitting model applied.

To obtain more detailed information on the changes in size of AgNP during the agglomeration/precipitation process DLS and spICP-MS can provide relatively fast nanoparticle size measurement. Figure 6 shows the Z-average diameter measured for different samples as a function of incubation time. Even if the data has to be treated carefully, due to the well-known inability of DLS to properly measure the particle size distribution of polydisperse samples in the presence of just a few percent of large particles [27] there is a clear general trend that indicated the increase presence of large AgNP in salt water.

A more robust assessment of the particle size distribution in the early stage of the agglomeration process can be obtained by spICP-MS. Figure 6. C and D show the PSD obtained by spICP-MS for free AgNP and AgNP-alginate, respectively, in ASW after 10 minutes of incubation. Without the protective effect of alginate, ASW cause the appearance of a second population centred at 75 nm, in addition to the main AgNP population at 55 nm. The spICP-MS measurement after 48 hours incubation showed a lower data quality with a reduced number of detectable peaks and a wider particle size distribution (data not shown).

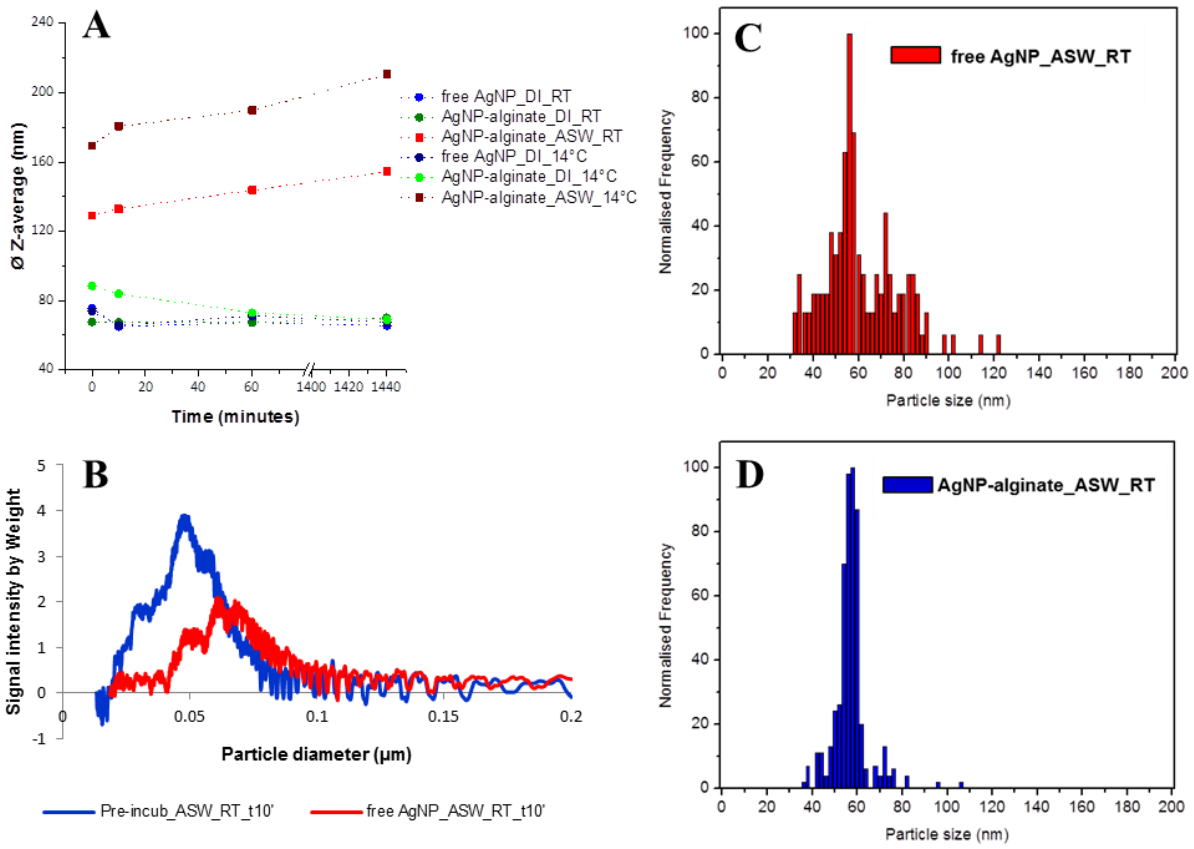

Figure 6. A) Average NP diameter measured by DLS, plotted by incubation time. B) Particle distribution, by weight, of free AgNP (red) and AgNP-alginate complex (blue), acquired by CLS. Size distribution, obtained by spICP-MS, of C) free AgNP and D) AgNP-alginate incubated 10 minutes in ASW.

Dissolved organic matter can contain different components in addition to alginate, in particular humic substances are one of the most common DOM in aquatic environments. As a proxy for this class of DOM, and for comparison with the AgNP-alginate complex, the effect of humic acid (HA) on AgNP behaviour in ASW was also tested by following the kinetics of agglomeration by UV-Vis spectroscopy and DLS. Figure 7 shows the UV-Vis and DLS data for AgNP in the presence of humic acid in deionized water and in ASW, together with data of free AgNP in ASW as control. The results show that AgNP-HA samples are relatively stable in deionized water, while in ASW both free AgNP and AgNP-HA complexes show significantly reduced LSPR of silver nanoparticles (Figure 7.A), with the largest decrease in intensity occurring for the free AgNP. Figure 7.B shows the fitting of UV-Vis intensities to a single exponential decay. The non-linear least square fitting analysis results in coefficients of

determination (R^2) of 0.97 for free AgNP and 0.86 for the AgNP-humic acid system, with time constants equal to 12±2 m^{-1} and 30±11 m^{-1}, respectively. These results show the qualitatively similar behaviour of this system compared to the AgNP-alginate system in ASW. The comparison of the time constants for the agglomeration process for the AgNP-humic acid, 30 m^{-1}, with that of 20 m^{-1} for the AgNP-alginate system suggest a slightly greater stabilization action of humic acid compared to alginate, in the initial part of the process.

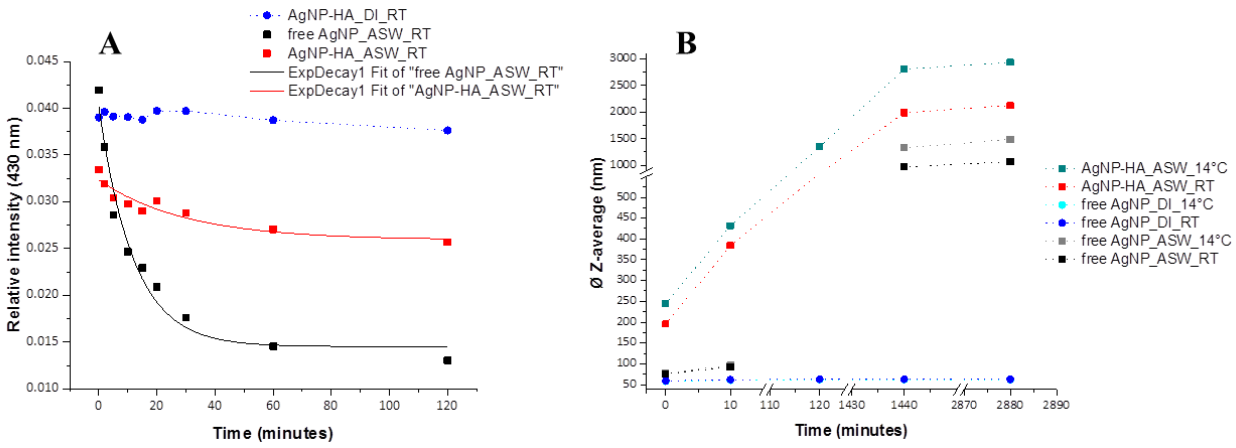

Figure 7. Agglomeration process of the AgNP-HA system. A) UV-Vis intensity of LSPR band at 430 nm vs. incubation time at room temperature of AgNP-HA in de-ionized water (blue), AgNP-HA in seawater (red) and free AgNP in seawater (black). Black and red lines show the exponential decay fitting model applied to free and complexed AgNP in ASW, respectively. C) Z-average values from DLS measurement of free and complexed AgNP in seawater (squares) and de-ionized water (circles) both at room temperature and at 14°C.

The agglomeration of AgNP in ASW is confirmed by DLS measurements, shown in Figure 7.C, independently of the incubation temperature. AgNP-HA complex in de-ionized water showed constant hydrodynamic diameters over the course of the experiment, in both temperature conditions. Samples in salty water showed increased Z-average values accompanied by increased polidispersivity values, indicative of agglomeration process. The data obtained by DLS for humic acid-containing samples is consistent with the data collected for alginate-containing samples. It is clear that such systems are complex and care should be taken in interpreting DLS data considering its tendency to omit small particle size distributions due to a strong scattering signal from large [27].

7.5. Conclusions

In this study we have developed an experimental approach to study the agglomeration process of silver nanoparticles in water as a function of key environmental parameters, such as temperature, dissolved organic matter and salinity under realistic testing conditions of light cycle and agitation. The use of complementary techniques has allowed us to gain in-depth insights of the agglomeration process at different time scales. The use of the localised plasmon resonance band of AgNP allowed us to obtain information on the time-dependent destabilization of AgNP, while the use of spICP-MS, CLS and AF4 permitted the measurement of particle size distribution at longer incubation times. In particular, we have shown that in marine waters silver nanoparticle agglomerates quite quickly, while they are reasonably stable in de-ionized water. Thus the presence of dissolved organic matter stabilizes AgNP in marine water compared to free AgNP and in addition the DOM coating of the nanoparticles may change the interaction with living organisms.

Natural systems are more complex than those studied here; in particular heteroaggregation processes, wide ranges of salinity, and variable amounts of DOM can influence the aggregation process of AgNP and thus their relative importance should be carefully evaluated. To this end, this study provides an experimental methodology for the in-depth analysis of the complex behaviour of silver nanoparticles and it will be important for the proper analysis of the fate of AgNP in the aquatic environment.

Acknowledgements

The work leading to these results has received funding from the FP7 program of the European Union under the SMARTNANO consortium (contract number FP7-NMP-2011-SME-5-280779). We would also like to thank the contribution of Dr. Hugues Crutzen.

7.6. Supplementary information

7.6.1 AgNP characterization

Silver nanoparticles (AgNP) were characterized in terms of size, dispersion and optical properties. AgNP size was determined by Centrifugal Liquid Sedimentation (CPS) and Dynamic Light Scattering (DLS), as explained on the manuscript. The dispersion (polydispersity index, PdI) was measured by DLS and the maximum absorption wavelength (λ) was determined by UV-Vis spectroscopy. Transmission Electron Microscopy (TEM) was used to visually evaluate AgNP characteristics (Fig S1). Nanoparticles were spotted on C-Cu grids and dried at 4°C before to analysis. Total silver concentration on the stock solution was measured by ICP-MS, after dilution in 1% nitric acid, revealing to be 20% less in mass. ICP-MS measurements were performed with an Agilent ICP-MS 7700x (Agilent Technologies, Santa Clara, USA) equipped with platinum sampling and skimmer cones, MicroMist quartz nebuliser and a quartz Scott spray chamber. Argon was used as carrier gas and He as a collision gas in a Octopole Reaction System (ORS). The ICP-MS was operated in full quantification mode. Rhodium in1% nitric acid was added on-line as internal standard (ISTD), via a t-tube mounted before the nebuliser pump. Monitored signals included masses 107 and 109 for Ag and 103 for Rh, isotope 107 on collision cell mode was used for quantification. A total of 6 silver concentration standards (plus blank) were prepared in 2% nitric acid in the range 0.2-50 µg/L. Calibration curves were read twice during the run. A total of five procedural blanks were analysed during the run. Table S1 summarizes characterization data both for size and mass.

Table S1: List of tested nanoparticles and accessed information on size, dispersivity and wavelength for maximum absorbance.

Sample	Size (nm)				PdI	Absorption λ (nm)	Ag concentration (mg/L)	
	Declared*	CPS[&]	spICP-MS[#]	DLS[^]			Declared	Measured (ICP-MS)
AgNP (Sigma)	60 ±4	53.4±6.6	55	67.02±0.99	0.123±0.01	430	20 ±1	16 ±0.37

* Size based on TEM, declared by the supplier (Sigma-Aldrich); [&] median of the particle size distribution based on weight; ^ Zeta average; [#] Median of the particle size distribution based on number

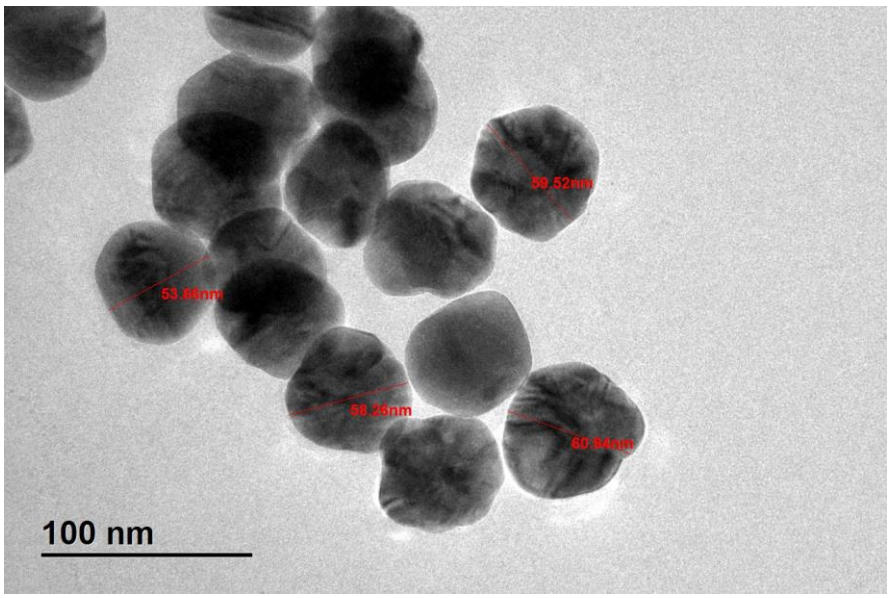

Figure S1. TEM image of 60 nm AgNP citrate stabilized from Sigma.

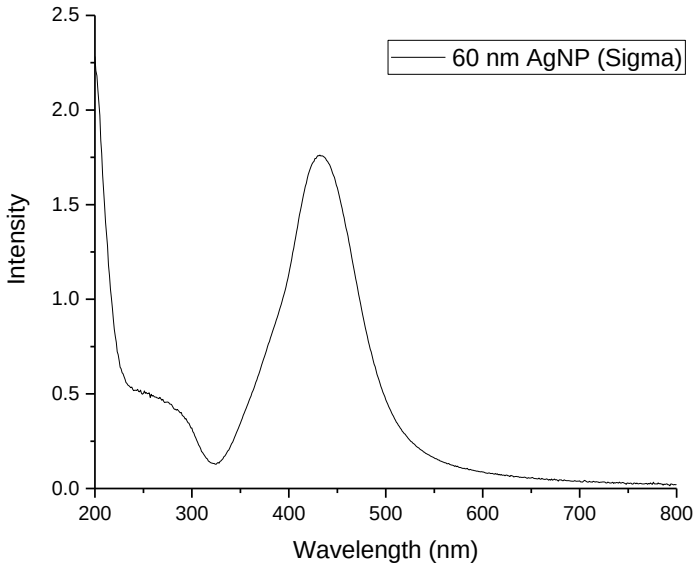

Figure S2. UV-Vis spectra of 60 nm AgNP citrate stabilized from Sigma.

7.7. References

1. Piccinno, F., et al., *Industrial production quantities and uses of ten engineered nanomaterials in Europe and the world.* Journal of Nanoparticle Research, 2012. **14**(9): p. 1-11.

2. Tay, C.Y., et al., *Back to Basics: Exploiting the Innate Physico-chemical Characteristics of Nanomaterials for Biomedical Applications.* Advanced Functional Materials, 2014. **24**(38): p. 5936-5955.
3. Setyawati, M.I., et al., *The influence of lysosomal stability of silver nanomaterials on their toxicity to human cells.* Biomaterials, 2014. **35**(25): p. 6707-6715.
4. Klaine, S.J., et al., *Nanomaterials in the environment: Behavior, fate, bioavailability, and effects.* Environmental Toxicology and Chemistry, 2008. **27**(9): p. 1825-1851.
5. Fabrega, J., et al., *Silver nanoparticles: behaviour and effects in the aquatic environment.* Environment international, 2011. **37**(2): p. 517-531.
6. Kaegi, R., et al., *Behavior of Metallic Silver Nanoparticles in a Pilot Wastewater Treatment Plant.* Environmental Science & Technology, 2011. **45**(9): p. 3902-3908.
7. Liu, J., et al., *Controlled Release of Biologically Active Silver from Nanosilver Surfaces.* ACS Nano, 2010. **4**(11): p. 6903-6913.
8. Xiu, Z.-m., et al., *Negligible particle-specific antibacterial activity of silver nanoparticles.* Nano Letters, 2012. **12**(8): p. 4271-4275.
9. Dobias, J. and R. Bernier-Latmani, *Silver Release from Silver Nanoparticles in Natural Waters.* Environmental Science & Technology, 2013. **47**(9): p. 4140-4146.
10. Sharma, V.K., et al., *Organic-coated silver nanoparticles in biological and environmental conditions: Fate, stability and toxicity.* Advances in Colloid and Interface Science, 2014. **204**(0): p. 15-34.
11. Cumberland, S.A. and J.R. Lead, *Particle size distributions of silver nanoparticles at environmentally relevant conditions.* Journal of Chromatography A, 2009. **1216**(52): p. 9099-9105.
12. Loosli, F., P. Le Coustumer, and S. Stoll, *Impact of alginate concentration on the stability of agglomerates made of TiO2 engineered nanoparticles: Water hardness and pH effects.* Journal of Nanoparticle Research, 2015. **17**(1): p. 1-9.
13. Hong, H., et al., *Characterization of dissolved organic matter under contrasting hydrologic regimes in a subtropical watershed using PARAFAC model.* Biogeochemistry, 2012. **109**(1-3): p. 163-174.
14. Calzolai, L., D. Gilliland, and F. Rossi, *Measuring nanoparticles size distribution in food and consumer products: a review.* Food Additives & Contaminants: Part A, 2012. **29**(8): p. 1183-1193.
15. Cascio, C., et al., *Critical Experimental Evaluation of Key Methods to Detect, Size and Quantify Nanoparticulate Silver.* Analytical Chemistry, 2014. **86**(24): p. 12143-12151.

16. Cascio, C., et al., *Detection, quantification and derivation of number size distribution of silver nanoparticles in antimicrobial consumer products.* Journal of Analytical Atomic Spectrometry, 2015.
17. Chambers, B.A., et al., *Effects of Chloride and Ionic Strength on Physical Morphology, Dissolution, and Bacterial Toxicity of Silver Nanoparticles.* Environmental Science & Technology, 2013. **48**(1): p. 761-769.
18. Ostermeyer, A.-K., et al., *Influence of Bovine Serum Albumin and Alginate on Silver Nanoparticle Dissolution and Toxicity to Nitrosomonas europaea.* Environmental Science & Technology, 2013. **47**(24): p. 14403-14410.
19. He, D., M.W. Bligh, and T.D. Waite, *Effects of Aggregate Structure on the Dissolution Kinetics of Citrate-Stabilized Silver Nanoparticles.* Environmental Science & Technology, 2013. **47**(16): p. 9148-9156.
20. Keller, A.A., et al., *Stability and Aggregation of Metal Oxide Nanoparticles in Natural Aqueous Matrices.* Environmental Science & Technology, 2010. **44**(6): p. 1962-1967.
21. Mitrano, D.M., et al., *Silver nanoparticle characterization using single particle ICP-MS (SP-ICP-MS) and asymmetrical flow field flow fractionation ICP-MS (AF4-ICP-MS).* Journal of Analytical Atomic Spectrometry, 2012. **27**(7): p. 1131-1142.
22. Peters, R.B., et al., *Development and validation of single particle ICP-MS for sizing and quantitative determination of nano-silver in chicken meat.* Analytical and Bioanalytical Chemistry, 2014. **406**(16): p. 3875-3885.
23. Geiss, O., et al., *Size and mass determination of silver nanoparticles in an aqueous matrix using asymmetric flow field flow fractionation coupled to inductively coupled plasma mass spectrometer and ultraviolet–visible detectors.* Journal of Chromatography A, 2013. **1321**(0): p. 100-108.
24. Linsinger, T.J., R. Peters, and S. Weigel, *International interlaboratory study for sizing and quantification of Ag nanoparticles in food simulants by single-particle ICPMS.* Analytical and Bioanalytical Chemistry, 2014. **406**(16): p. 3835-3843.
25. Loeschner, K., et al., *Optimization and evaluation of asymmetric flow field-flow fractionation of silver nanoparticles.* Journal of Chromatography A, 2013. **1272**(0): p. 116-125.
26. Delay, M., et al., *Interactions and stability of silver nanoparticles in the aqueous phase: Influence of natural organic matter (NOM) and ionic strength.* Journal of Chromatography A, 2011. **1218**(27): p. 4206-4212.

27. Calzolai, L., et al., *Separation and characterization of gold nanoparticle mixtures by flow-field-flow fractionation.* Journal of Chromatography A, 2011. **1218**(27): p. 4234-4239.

8. Chapter VI

Detection of Silver Nanoparticles inside Marine Diatom *Thalassiosira pseudonana* by Electron Microscopy and Focused Ion Beam

César Pascual García[a] Alina D. Burchardt [bc], Raquel N. Carvalho[b], Douglas Gilliland[a], Diana C. António[ad], François Rossi[a] and Teresa Lettieri[b]

[a] European Commission - Joint Research Centre, Institute for Health and Consumer Protection, T.P. 203, Via E. Fermi 2749, 21027 Ispra (VA), Italy

[b] European Commission - Joint Research Centre, Institute for Environment and Sustainability, T.P. 121, Via E. Fermi 2749, 21027 Ispra (VA), Italy

[c] FU-Berlin, Fachbereich Biologie, Chemie, Pharmazie, Takustr. 3, 14195 Berlin, Germany

[d] Departamento de Biologia & CESAM, Universidade de Aveiro, Aveiro, Portugal

PLoS One, Volume 9(5): e960785, 5 May 2014

doi:10.1371/journal.pone.0096078

8.1. Abstract

In the following article an electron/ion microscopy study will be presented which investigates the uptake of silver nanoparticles (AgNPs) by the marine diatom *Thalassiosira pseudonana*, a primary producer aquatic species. This organism has a characteristic silica exoskeleton that may represent a barrier for the uptake of some chemical pollutants, including nanoparticles (NPs), but that presents a technical challenge when attempting to use electron-microscopy (EM) methods to study NP uptake. Here we present a convenient method to detect the NPs interacting with the diatom cell. It is based on a fixation procedure involving critical point drying which, without prior slicing of the cell, allows its inspection using transmission electron microscopy. Employing a combination of electron and ion microscopy techniques to selectively cut the cell where the NPs were detected, we are able to demonstrate and visualize for the first time the presence of AgNPs inside the cell membrane.

8.2. Introduction

Diatoms play a major role in the earth's carbon cycle fixing about 40% of the total carbon in oceans and serve as the base of the marine food chain [1]. They are ubiquitously distributed in all aquatic ecosystems and have been used for many years as ecological indicators [2]–[4]. More recently, diatoms have also been studied as non-model organisms to investigate the mechanism of toxicity of chemical pollutants at a molecular level [5]–[7]. Given the increasing relevance of engineered nanomaterials worldwide and their uncontrolled release into the environment there is a rapidly growing concern about the potential toxicological impact on many aquatic organisms including small autotrophs such as diatoms. Among the various classes of nanomaterials present in commercial products silver nanoparticles (AgNPs) represent one of the most commonly used due to their highly efficient antibacterial properties. Common examples of their use include biocidal additives, silver impregnated antibacterial materials, and disinfectants. Nanoparticle incorporation has been reported in various cell types such as algae [8], nematode [9], fish [10], [11] and human mesenchymal stem cells [12]although the uptake mechanisms and affected intracellular pathways are still under investigation. Previous research has suggested that the toxicity of AgNPs to microorganisms is due to the release of Ag ions into the media [13], [14]. In a recent study of time-dependent cellular growth, we reported how exposure to both AgNPs and silver nitrate ($AgNO_3$) could inhibit the growth of diatoms and cyanobacteria. The data suggested that the toxicity for the biota was the result of a combination of effects from both the AgNPs and the released silver ions [15].

The unique morphology of diatoms with their silica outer shell represents a particular challenge for the study of AgNPs internalization. The marine diatom *Thalassiosira pseudonana* used in our studies is characterized by a cylindrical shell consisting of two valves joined by girdle bands-features which have been widely characterized by techniques like scanning electron microscopy (SEM) or atomic force microscopy (AFM) [16], [17]. The silica outer shell is assembled in an intricate three-dimensional pattern of nanopores leaving a considerable surface open for the interaction of the cell with its environment, including the transport of nutrients or even environmental pollutants. The diffusion of particles through the diatom outer shell has been shown to depend not only on the overall surface of the cell but also on the size of the pores and the tortuosity of the path [18]. Thus, the intricate three-dimensional structure likely represents a natural filter for the flow of larger molecules and nanomaterials such as NPs.

A number of metal NPs have unique plasmon-resonant optical scattering properties that can be used to localize them inside microorganisms using optical microscopy [19]. The identification and localization of intracellular gold NPs has been possible with advanced methods such as Raman or hyperspectral confocal microscopy [20], [21]. The detection of the characteristic plasmonic signature of silver NPs in the diatom/AgNPs system provided indications that a similar situation may be occurring in this system [22]. Unfortunately, more precise localisation of NPs in cells is not possible by optical microscopy because of the fundamental limitations in resolution imposed by the wavelength of the incident light.

Recently, study using a combination of optical and AFM methods showed the interaction of NPs with diatom cells [22]. They demonstrated evidence that nanometer scale structural changes to cell morphology can be induced by AgNPs and inferred the internalization of AgNPs into the cell following the observation of coagulation of the internal cell material. Unfortunately, the application of AFM is restricted to the study of the outer shell and thus the presence of NPs inside could not be visualized with submicron resolution.

Transmission electron microscopy (TEM) has been employed to image the interaction of polydispersed AgNPs with the bacteria *Ochromonas danica* and *Pseudomonas putida* [8], [23]. This methodology involves the preparation of cell slices with a thickness of around 100 nm making the study of whole cell morphology difficult since consecutive sequences of microtome slices must be imaged if a complete tomography of the cell is to be achieved. SEM instrumentation, when compared to TEM, is generally simpler and more accessible and this has been widely employed to characterize the external morphology of diatoms [24], [25]. Furthermore, SEM in combination with X-ray spectroscopy can provide very good resolution of the morphology as well as the spatial distribution of the atomic elements in diatoms [26]. To target the inside of the diatom SEM can also be used in combination with ion-abrasion employing a focused ion beam (FIB) [24]. When suitably automated this method allows the 3D reconstruction of organic tissues with a good results in terms of depth versus resolution [27]. The principle problem of TEM microtome and FIB 3D reconstruction methods is that the processes of cell cutting is relatively slow and this is further compounded by the fact that the position of the NPs in a sample fixed with resins is *a priori* unknown, so finding the sections of interest occurs by trial and error or by a long systematic series of cuts.

Recently, we have presented a convenient method of using electron and ion microscopy [28],[29] to study the interactions of metal NPs with cells grown in suspension. The method, based on cell preparation by critical point drying, was able to detect NPs down

to 5 nm in the cells and to distinguish between genuine uptake/internalization and mere interactions between the particles and the membrane surface. In our studies, we used this technique to investigate the internalization of the AgNPs in the marine diatom *T. pseudonana*. The original method was adapted to use diatoms as a way to adequately preserve the shape of the organism while, at the same time, ensuring the necessary transparency for the electron microscopy study in transmission mode.

In our procedure the localisation of the NPs in the diatom was based on the comparison of the signals from the transmitted and scattered electrons. In this way the NPs which were detected in transmission but not with SEM mode were below the surface. To confirm their presence inside the cytoplasm of the diatoms we applied FIB milling to visualize inside the cell. The silver content of nanoparticles was verified in our experiments using electron dispersion X-ray signal (EDX). To our knowledge this is the first time that it has been possible to show the presence of AgNPs actually inside the cytoplasm of the marine diatoms.

8.3. Materials and Methods

8.3.1 Materials

All experiments were carried out using maltose-stabilized nanoparticles in an aqueous suspension. Chemicals used for diatom culture media were purchased from Sigma-Aldrich. Silver nitrate ($AgNO_3$) (99.9%), ammonium hydroxide (5N in H_2O), D-(+)-maltose monohydrate (98%), sodium borohydride (98%) were purchased from Sigma-Aldrich and used without any further purification.

Synthesis of Silver Nanoparticles

AgNPs were prepared via a modified Tollens process in which the complex cation $[Ag(NH_3)_2]^+$is reduced to form silver metal nanoparticles through chemical reduction by sugars as described previously [15]. The particle size distribution in the resulting AgNPs dispersion was analyzed by Centrifugal Liquid Sedimentation (CLS) [31] and Scanning Electron Microscopy (SEM). According to the particle number distribution, the sample was polydispersed with size distribution between 5 and 120 nm (data shown in supporting information).

8.3.2 Diatom Culture

T. pseudonana (strain CCMP 1335) was purchased as axenic culture from the Provasoli-Guillard National Center for Culture of Marine Phytoplankton (CCMP, West Boothbay Harbour, Maine, USA). Diatom cultures were kept in artificial sea water (ASW)-f/2 medium [32], [33] at 14°C under a diurnal light cycle of 13 h light and 11 h darkness and continuous shaking at 100 rpm. Cell density and cell growth were calculated as published previously [34].

Exposure of Diatom Cultures to AgNPs

In order to test the uptake of AgNPs, diatoms were exposed to silver nanoparticles at a concentration of 50 µM in ASW-f/2 medium. Diatom cells were cultured at an initial cell density of 0.75×10^6 cells/mL in 20 mL batch cultures. After 24 h, the nanoparticles were added to the culture just before the light cycle started and then incubated for 48 h.

8.3.3 Sample preparation for electron microscopy

The cell preparation for electron microscopy consisted in a standard, single cell chemical fixation [24], [35] followed by critical point drying. After incubation with AgNPs, $20-50\times10^6$cells were harvested and fixed by adding glutaraldehyde at a concentration of 2.5% for 30 min at 4°C. The cells were pelleted and washed with distilled water. The cell pellet was then post-fixed with 2% OsO_4 for 20 min, centrifuged and washed again with water. The OsO_4 was used to fix the lipidic structures in the cell [36]. All the centrifugation steps were performed at 2500×g for 5 min.

After cell fixation, a sequential solvent exchange was done using increasing concentrations of ethanol in water (25, 50, 75, 90 and 100%). After each solvent exchange, the cells were incubated for 5 min followed by centrifugation at 2500×g for 5 min. The final pellet was placed in a vial with a porous lid and CO_2 critical point drying performed. Ethanol was exchanged by liquid CO_2 at 5°C and 50 bar using several rinsing steps in an EMITEC critical point dryer. The pressure was increased in the closed volume, raising it to the critical point of CO_2 by increasing the temperature. The pressure was then gradually decreased to ambient level over a period of one hour. The final product was a fine black powder containing the cells. Each of the samples was then transferred into individual grids of 300 µm mesh copper coated with graphite for support.

8.3.4 Scanning electron microscopy and EDX analysis

A double beam scanning electron microscope FEI-NOVA 600i NANOLAB equipped with FIB and a gas injector (GIS) with platinum precursor was used for SEM analysis. The system was equipped with traditional secondary and in-lens detectors as well as X-ray analyser for Energy-Dispersive X-ray Spectroscopy sensitive to carbon and other higher atomic weight elements. A scanning transmission electron microscopy (STEM) detector was used for transmitted electrons.

In order to study the cell-NPs interaction, the cells were firstly scanned in the transmission mode to detect AgNPs using 30 keV acceleration voltage (HV) which was the maximum possible in our scanning microscope. Although traditional TEM instrumentation provides acceleration voltages up to 300 keV in our case we compared STEM images at 30 keV with TEM images taken with a JEOL JEM 2100 TEM microscope at 200 keV (see Figure S3). As would be expected, the contrast and resolution of TEM images were superior to that of STEM but the main information necessary to detect AgNPs was equivalent. After identifying the position of the NPs, the surface of the cell was explored using low accelerating voltages (5 keV) to avoid signals coming from deep intracellular structures. For those cells with insufficient electrical grounding (enough contact with the electrical conductive grid support), it was necessary to raise the energy to 25 keV to visualize the diatom surface, even though at this energy some signal from below the surface was observed. However, even when using an accelerating voltage of 25 keV the position of the surface bound NPs was recognizable using the SEM mode.

In those cases when NPs detected in transmission mode could not be found at the surface, a search for NPs inside the cell was initiated in that region by performing a cut using focused ion beam (FIB) milling. Before starting the cut, the region of the cell containing the NPs was protected by depositing a metallic layer on top of the cell using Pt-GIS activated with the electron gun to avoid a curtain effect [37]. The rest of the milling procedure was made following the method already described in [28]. EDX image maps were treated using the open software program Image-J [38] for noise reduction using a Gaussian Spatial filter (see supplementary information).

8.4. Results

8.4.1 Surface analysis of Thalassiosira pseudonana exposed to AgNPs

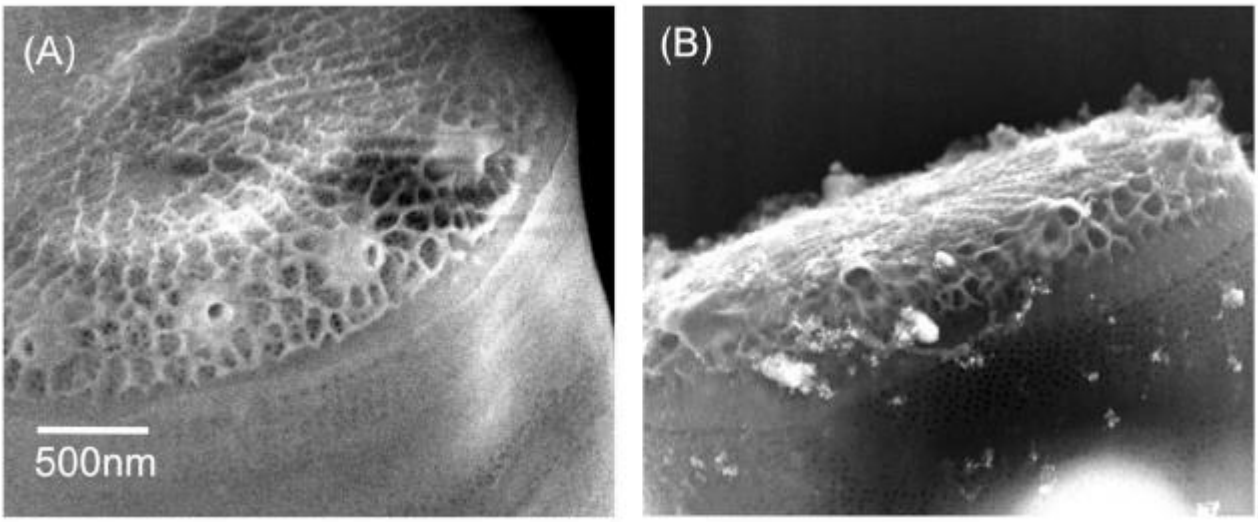

Figure 1. Scanning electron microscope images of the nanostructured pores in the shell of two diatoms corresponding to the control (A) and AgNPs exposed (B) samples respectively (scale bar common in both pictures).

Diatom cells exposed to AgNPs were analyzed by SEM. Figure 1A shows a representative image of the diatom external frustule belonging to the control (sample incubated without NPs) using classical SEM imaging of electrons originating mostly from the first few nanometers at the diatom surface. The untreated diatom cells showed nanopores with an average diameter of 20±3 nm (n=81) while the larger pores in the valve (portulae) had an external diameter of 72±19 nm (n=10). The values are consistent with those reported previously by Hildebrand et al. 2006[16]. Figure 1B shows NPs attached to the surface of a diatom of the exposed sample. Agglomerated and dispersed AgNPs of different sizes were found on the surface of the valves and the girdle band (Figure 1B) with the latter being often associated with organic material. No noticeable morphological changes were detected in the size and shape of the diatoms when exposed to the AgNPs. Additionally, the pore sizes of the diatoms in both the untreated and exposed cells showed similar values.

Figure 2 shows the silver NPs detection scheme. The NPs were detected at the surface using scattered and secondary electrons in SEM mode (Figure 2A). The cell was also inspected in

transmission mode with 30 keV (Figure 2B). The comparison of these two images shows where the NPs were localized. In the case of this cell, all the NPs found were at the surface. Transmission images like the one in Figure 2B allow us also to visualize the dimensions of the cytoplasm of the cell compared to the silica shell. We noticed a shrinkage of the cells of approximately 60% (estimation based on imaging shown in Figure S2), similar to other values in literature of cells treated with critical point drying [30]. The silver content of the NPs was further confirmed with EDX. Figure 2C shows the carbon (blue), silicon (yellow) and silver (red) maps, which correspond to the position of organic matter, the diatom shell and AgNPs respectively.

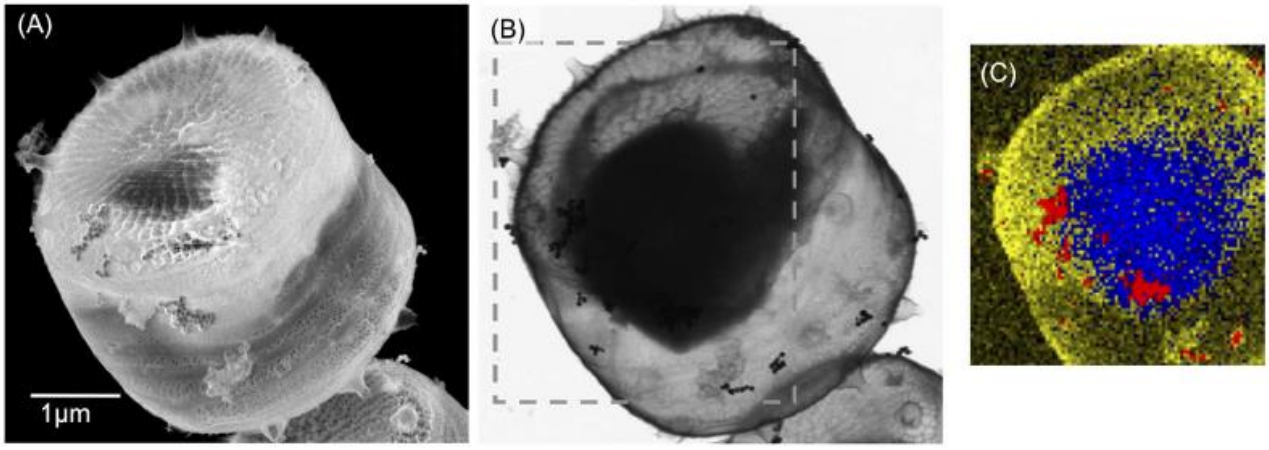

Figure 2. Scanning electron microscope images of a diatom exposed to AgNPs using the signal from the surface (A) and in transmission (B). (C) shows the EDX map of carbon (blue), silicon (yellow) and silver (red) of the area indicated by the dashed squares in (B) assigned to the organic part, the exoskeleton and AgNPs respectively (scale bar common to the pictures (A) and (B)).

8.4.2 Uptake of AgNPs

In order to study the fate of the NPs, we analyzed several diatom cells using the same approach described for the cell in Figure 2. Traditional SEM and STEM analyses of a representative diatom are shown in Figure 3 A and B, respectively. At low voltages (5 keV,Figure 3A), the signal reveals the details from the surface of the diatom. AgNPs standing outside the valve are detected in this way while the membrane and internal compartments

were not visible. By contrast, using STEM at 30 keV it was possible to visualize the inner part of the diatom (Figure 3B) and screen the AgNPs in the cell that were not visible at the surface.Figures 3 C and D show an enlargement of the dashed area in Figures 3 A and B. These images were used for the localization of AgNPs. It was possible to assign the NPs to the diatom surface whenever the NPs were visible in both SEM and STEM images (e.g. see the blue arrow in Figures 3 C and D). However, some NPs were only visible in transmission mode (e.g. NPs pointed by the red arrow in Figure 3D) and were likely inside the diatom shell. These cells were selected as candidates for further analysis on NP uptake.

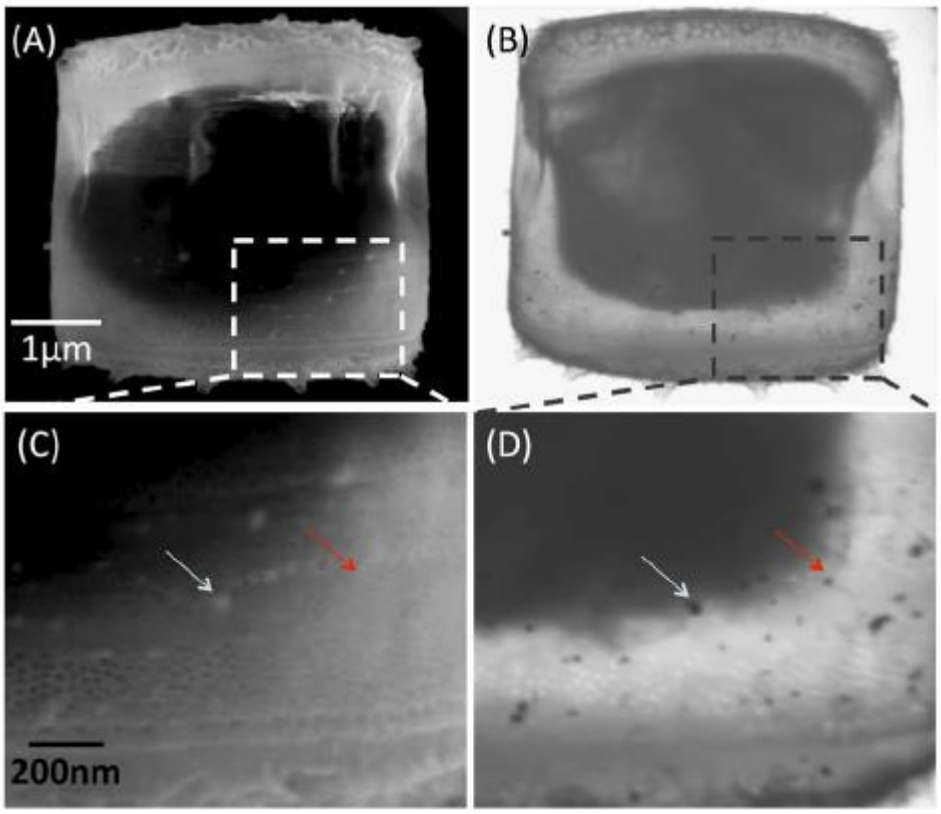

Figure 3. Scanning electron microscope images of a second diatom exposed to AgNPs, using the signals from the surface (A) and in transmission (B). (C) and (D) show magnifications of the same area of the cell indicated with the dashed squares, where it is possible to detect NPs in the surface (i.e. blue arrow) or potential internalized particles (i.e. red arrow) (scale bars common to pictures (A), (B) and (C), (D) respectively).

8.4.3 Intracellular analysis of AgNPs

To confirm the uptake and the intracellular location of silver nanoparticles, a cross-cut was performed by milling into the cell in the region where the comparison between surface and transmission images indicated the presence of NPs inside the shell of the diatom. Figure 4 illustrates a cut of the cell shown in Figure 3 done for intracellular inspection. The section was performed at the level of the cytoplasm. The platinum stripe, deposited to avoid the curtain effect during the milling process, can be seen in Figure 4A shadowed with blue. Figure 4B shows the section of the cell after the cut, while the enlargement of the cytoplasmic region is shown in Figure 4C. Some of the brighter spots localized in this picture reveal higher scattering cross sections that could indicate higher density atoms related to a silver content. Figures 4 D and E show the Ag and Os EDX maps respectively over the secondary electron signal obtained with the EDX detector. Since osmium had been used for cell fixation (see Material and Methods), the homogeneous distribution over the cytoplasm shown in Figure 4E was as expected. In contrast to this, the Ag distribution was heterogeneous (see Figure 4D), with certain areas being exceptionally dense, and matching the brighter areas in Figure 4C indicated by a red arrow. The EDX point spectra analysis in this region was compared to the background (red and blue squares in Figure 4D respectively) and plotted in Figure 4F. The elemental analysis of the cell by EDX showed signals for C, N, O, Si, Os, S and Cl from the cell as well as Cu, Al, Pt and Ga identified as contaminant signals likely coming from the supporting grid, the microscope chamber, the protection layer and deposited Ga atoms during the ion milling process, respectively. The homogeneous distribution of Os in the EDX maps confirmed the overall distribution and also indicates that no Os agglomerates were formed during the fixative process. By analyzing the SEM images of the section and the EDX data we can correlate the studied high-density clusters in Figure 4C (pointed with the red arrow) to silver aggregates.

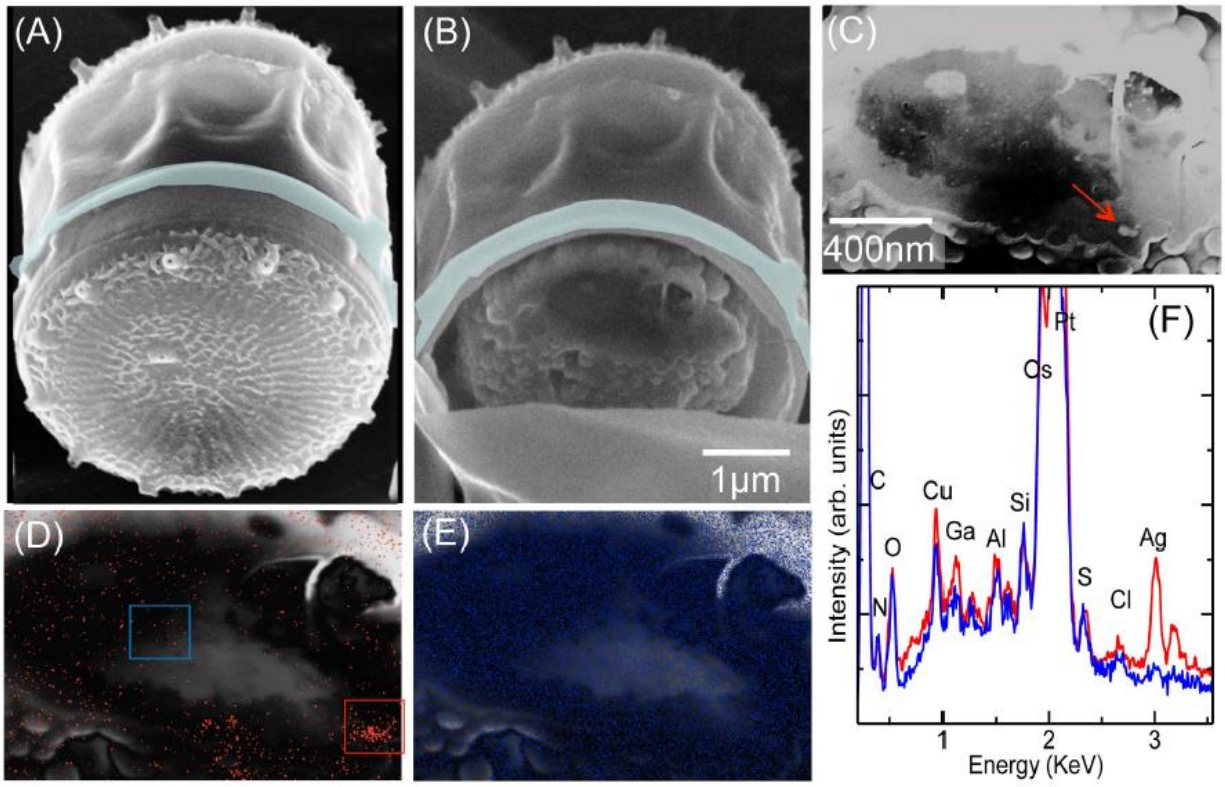

Figure 4. Sequence of the cut and detection of Ag content in the section from the same cell shown in Figure 3. (A), the cell after the deposition of the Pt protective layer. (B), the cell after the cut; (C) an enlargement of the section of the cell with an enhanced contrast. (D) and (E), the Ag and Os EDX maps respectively over the Secondary Electron signal collected by the EDX detector. (F) EDX spectra from the background (blue) and the bright spots (red) corresponding to the blue and red square area shown in the panel (D). The bright spots are also marked by the red arrow in panel (C).

These results could be reproduced in other cells (see Figures S5, S6). We performed different cuts in a total of 12 diatom cells. Bright spots inside the cytoplasm of the cell could be detected in seven of the cuts. These spots may be associated with Ag aggregates, although Ag EDX signal associated with them was detected only in five of the cells (a second example is shown in Figure S6). The emergence of bright spots without EDX signal could occur since the detection of X-rays is much less efficient than that of electrons, therefore there is a higher threshold for the detection of silver by EDX. In some cells we found neither Ag EDX signal nor bright spots corresponding to possible NPs, even when the comparison of the intact cell by SEM/STEM suggested that some of the NPs were located internally (e.g. in Figure S5H). The failure to detect Ag nanoparticles in the cuts may be partially explained either by the induced ion abrasion damage or by the displacement of the section due to charging effects.

8.5. Discussion

In this study, the intracellular uptake of AgNPs by the marine diatom *Thalassiosira pseudonana* was investigated by combining SEM/STEM/FIB. By correlating the surface and transmission signals, we demonstrate that it is possible to detect NPs that have crossed the outer silica shell and then, by using an ion beam to mill into the sample, we found evidence confirming the presence of internalized metal rich clusters. The Ag content of these clusters was demonstrated using EDX analysis. The combination of dual beam microscopy with EDX is a powerful strategy to analyze a precise smooth section [24], [39]. However, with the current SEM/FIB instrumentation, the FIB abrasion requires time-consuming processes to minimize damage in the organic material of the cell. Even using the method described here which minimizes the time for milling by allows the detection of regions of interest prior to the cut, we believe that SEM/FIB methods should be considered most suitable for studies on laboratory-cultured cells rather than for cells originating in the natural environment. In the latter case the concentration of AgNPs would general be much lower making its detection difficult.

While this study has shown the presence of internalized Ag clusters, determining the mechanism by which they may reach the cell interior is a much more complex issue and requires careful consideration of many aspects of the behavior of silver nanomaterials. Metallic AgNPs may not be chemically stable under common environmental conditions and can be easily oxidized, particularly when exposed to sources of light or, alternatively, may complex with naturally occurring organic ligands such as humic or fulvic acids. Similarly, silver in the ionic state can also be reactive and can complex with organic molecules [40] such as proteins or even be reduced back to the metallic state by mild reducing agents. Reactions can occur between ionic silver and sulfides or chlorides resulting in the formation of low solubility products such as AgCl and Ag_2S. In the case of AgCl the situation is further complicated as exposure to a high salinity environment may result in the formation of more soluble complex chlorides which can re-solubilize the Ag [15]. Many types of AgNPs are dependent on electrostatic repulsion for their colloidal stability and thus tend to aggregate in high ionic solutions such as seawater which effectively screens the charge on the particle leading to reduced repulsion and eventual coagulation due to van der Waals forces [41]. The

AgNPs in our culture could be detected attached to the cell surface of *T. pseudonana*, on the valve and girdle band. While AgNPs in a monodispersed form were observed, aggregates or clusters of AgNPs were also very common. The nanoparticles found attached to the diatom cells had a broad range of sizes, including sizes smaller than the pore diameters of the outer shell. The cell wall in the centric diatom *T. pseudonana* may be permeable to small particles entering through the naturally existing pores. Nevertheless, the mobility of molecules inside a diatom pore is affected not only by the diameter of the outer opening but also by the pore geometry across the shell structure [18]. Studies performed by Yang et al. would suggest that the diatom surface topography helps the diatoms to sort and filter the particles [42]. It is thus not certain what the size exclusion limit is for the entry of nanoparticles in *T. pseudonana*.

Another mechanism that would allow the crossing of the AgNPs through the cell wall was shown by Pletikapić and coauthors using atomic force microscopy [22]. The cell exoskeleton of diatoms is covered by an organic envelope essentially composed by polysaccharides and proteins [43], [44], [45]. AgNPs have shown high reactivity with these exopolymeric substances (EPS). Indeed the production of EPS is increased with the AgNPs exposure [46],[47]. Furthermore they showed that the mechanism of entrance of AgNPs through the cell wall of the marine diatoms *C. fusiformis and C. closterium* involved localized damage without disintegration of the cell wall. In our case, AgNPs also seemed to be preferentially associated with the organic content at the surface of the *T. pseudonana* although no damage was verified in the exoskeleton, AgNPs could potentially cross the shell barrier in a similar way to that in the study by Pletikapić and coauthors.

After crossing the outer-shell in diatoms, NPs must also cross the cellular membrane to reach the cytoplasm and the intracellular compartments. In our paper we have demonstrated the presence of Ag clusters inside the cytoplasm. In a previous paper the toxic effect of AgNPs exposure to *T. pseudonana* could be explained by a combination of integral AgNPs and other silver containing species that were released in the artificial seawater [15]. The observation of intracellular nanoparticulate silver in the present study could thus explain the contribution of AgNPs to the observed toxicity by providing a localized source for the release of silver ions in close vicinity to the molecular targets. However, the SEM images and detection of silver by EDX only provide static temporal information on the presence of high density silver clusters inside the diatom cells but do not provide all the information about the mechanism of uptake or the nature of the internalized silver. In fact, our data could be explained by an uptake of small silver nanoparticles but it cannot be excluded that these-high density silver signals

could arise from an uptake of free silver that subsequently precipitates and aggregates inside the cells.

In summary, we have shown a potentially attractive method for investigating the interaction of diatoms with AgNPs. We believe that its use in this study has begun to reveal more about the role of AgNPs in the toxicity of microorganisms and it shows a potential which could be exploited in further in-depth studies of their interaction with monodispersed AgNPs and ionic silver.

Acknowledgments

We thank Joaquin Pinto Grande for technical assistance and Luigi Calzolai for his suggestions and critical comments.

8.6. Supporting Information

8.6.1 Particle analysis

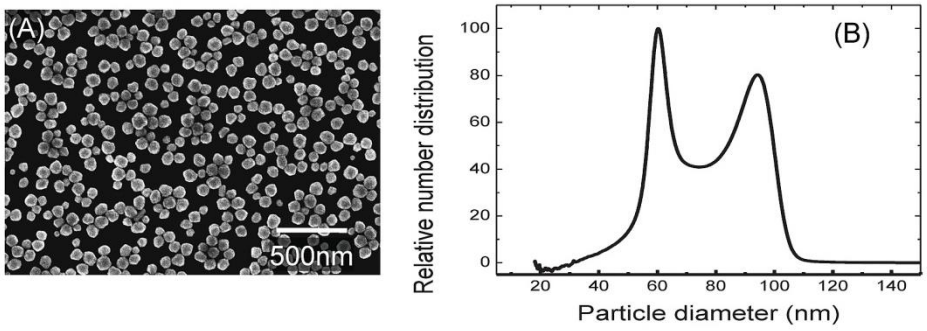

Figure S1. (A) SEM of the NPs used in the study. (B) Centrifuge Liquid Sedimentation analysis of the size of the AgNPs.

Particles were analyzed using CLS and SEM. Particles' diameters resulted less than 120 nm. Below 30 nm CLS reaches its limit of sensitivity and we cannot exclude particles of smaller size. For this reason we considered our nanoparticles as polydispersed AgNPs.

8.6.2 Control sample

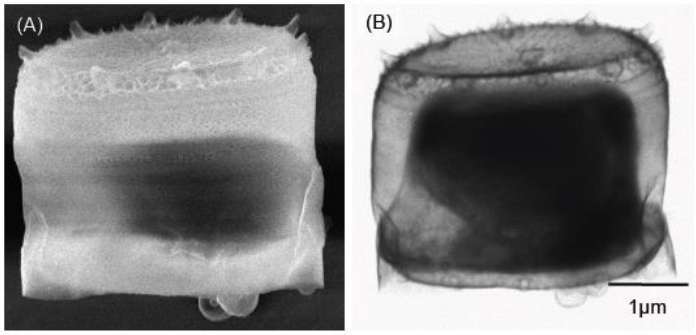

Figure S2. SEM images of one of the diatoms from the control sample using the signal from the surface (A) and in transmission (B) (common scale bar).

The control sample was prepared in the same way described in materials and methods without the incubation with AgNPs. The shrinkage of the cells was calculated from STEM images in Figures 3B and S2B using the ratio of the volume of the shell and cell-membrane. The shape used to estimate both volumes was a cylinder ($Lx2\pi(D/2)^2$), where L and D are the measured length and diameter of the diatom corresponding to the vertical and horizontal directions respectively in both pictures.

8.6.3 TEM Comparison

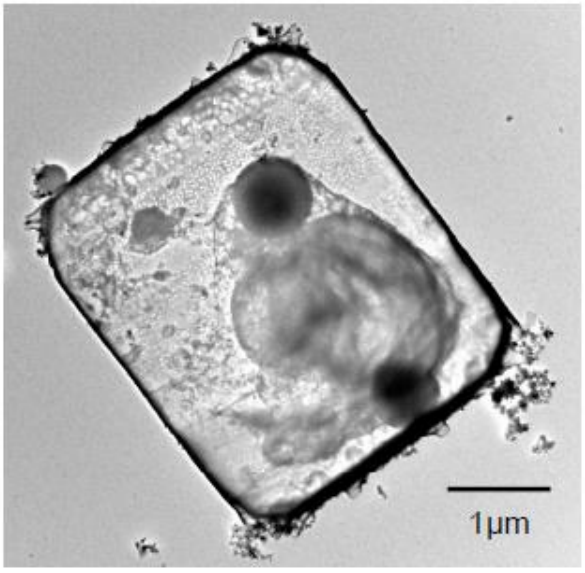

Figure S3. Transmission electron microscope (TEM) image performed with 200 keV HV.

Picture S3 shows a TEM image of a AgNP exposed diatom. The picture was made using a JEOL JEM 2100 TEM microscope at 200 keV (see Figure S3). We compared the STEM images at 30 keV with the ones at 200 keV from the TEM. The contrast and resolution of TEM images were superior to STEM, but the main information about the localization of NPs was equivalent. The higher contrast in TEM images allows a better recognition of organelles in the diatom.

8.6.4 Image processing

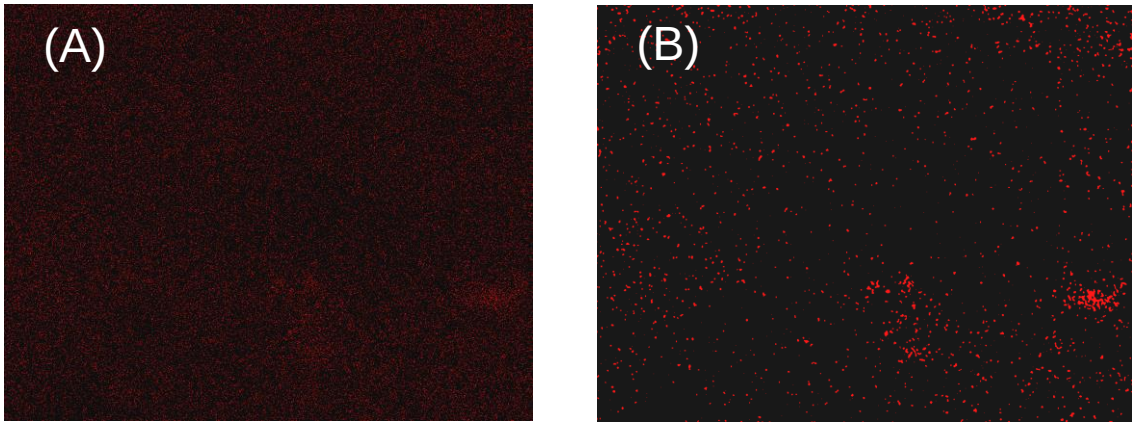

Figure S4. EDX Ag map before (A) and after (B) image processing using a Gaussian filter shown in the table S1.

Images were processed using open software Image-J using the convolve command.

Table S1. Kernel of the Spatial Gaussian filter used to deconvolve the EDX signal from Ag and Os inFigure 4.

0	1	2	1	0
1	3	5	3	1
2	5	9	5	2
1	3	5	3	1
0	1	2	1	0

8.6.5 Diatom FIB sections

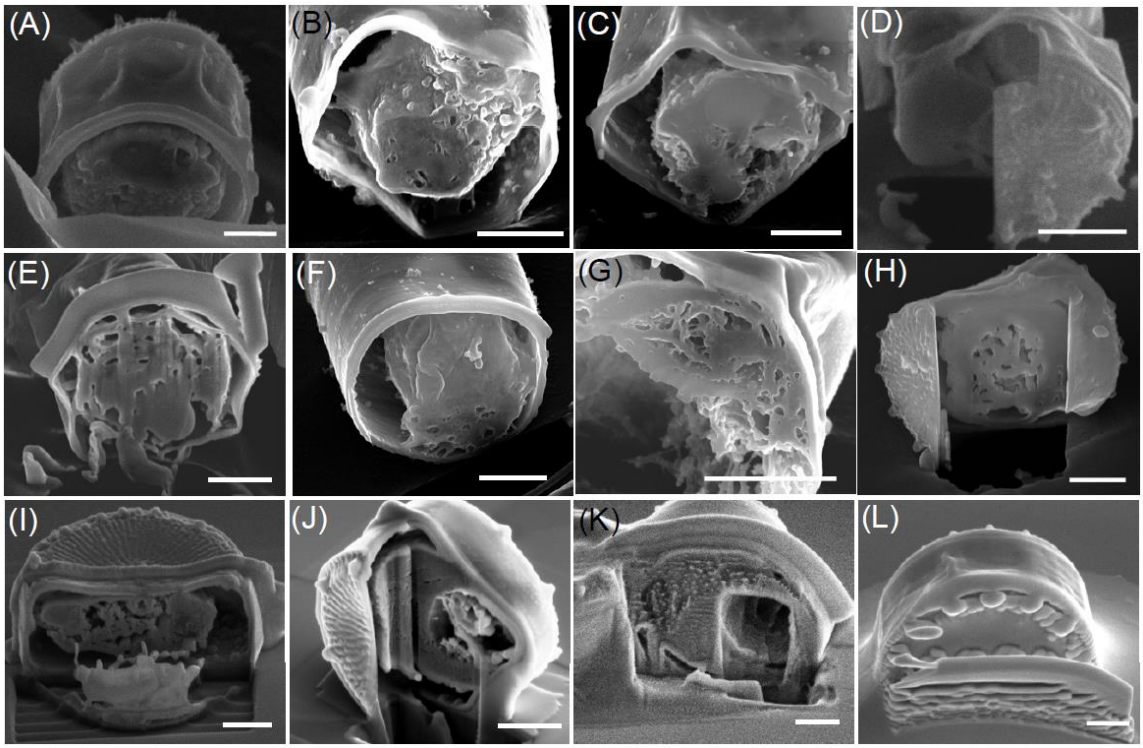

Figure S5. Electron microscope pictures of the total 12 cuts made in this study. Bright spots in the cytoplasm region of the section were found in a total of seven cases (A) to (G), while EDX signal associated with these spots were detected in five cases (A) to (E).

We performed different cuts in a total of 12 diatom cells. Bright spots inside the cytoplasm of the cell, associated with high density clusters could be detected seven of the cuts, while Ag EDX signal associated with some of these spots was detected in five of them (a second detailed example is shown in Figure S6, while for the other cuts the raw data are summarized in S7).

We attribute the fact that we see more bright spots than EDX signal to the higher cross section for electron-electron scattering than electron-X-rays scattering, and therefore there is a higher threshold for the detection of silver by EDX. In some cells no high density clusters or Ag EDX signal were visible inside the cell after the cut, even though the comparison of the intact cell by SEM/STEM suggested some of the NPs were not located at the surface. This could be partially explained by the introduction of damage by the ion abrasion, as evidenced by the detection of a curtain effect (the transport of material from the top of the cell). In these cases we did not detect neither silver nor the existence of high density spots.

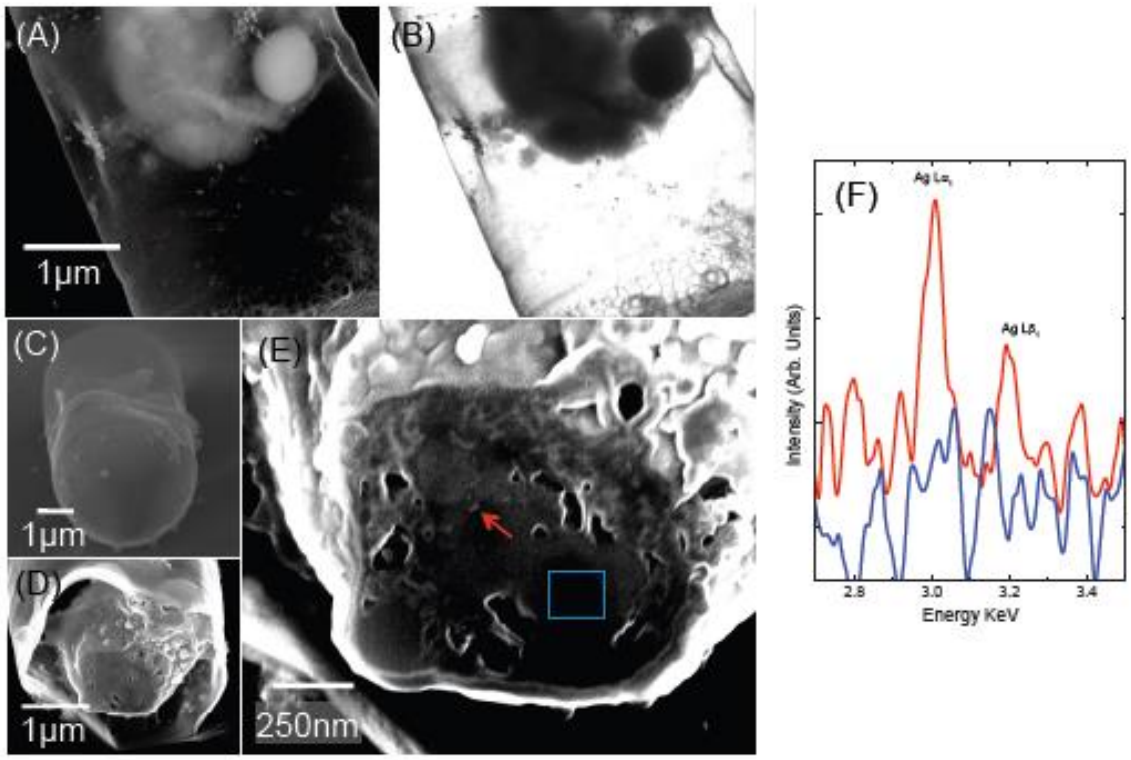

Figure S6. Sequence of the cut and detection of silver content into AgNP exposed diatom. (A) and (B) are scanning electron microscope images of the diatom incubated with AgNP using the signal from the surface and in transmission respectively (common scale bar). (C) shows the cell after the deposition of the Pt protective layer. (D) shows the cell after the cut while (E) shows an enlargement of the section of the cell with an enhanced contrast. (F) EDX spectra from the background (blue region in (E)) and from the bright spot marked with the red arrow in (E) are shown in blue and red respectively.

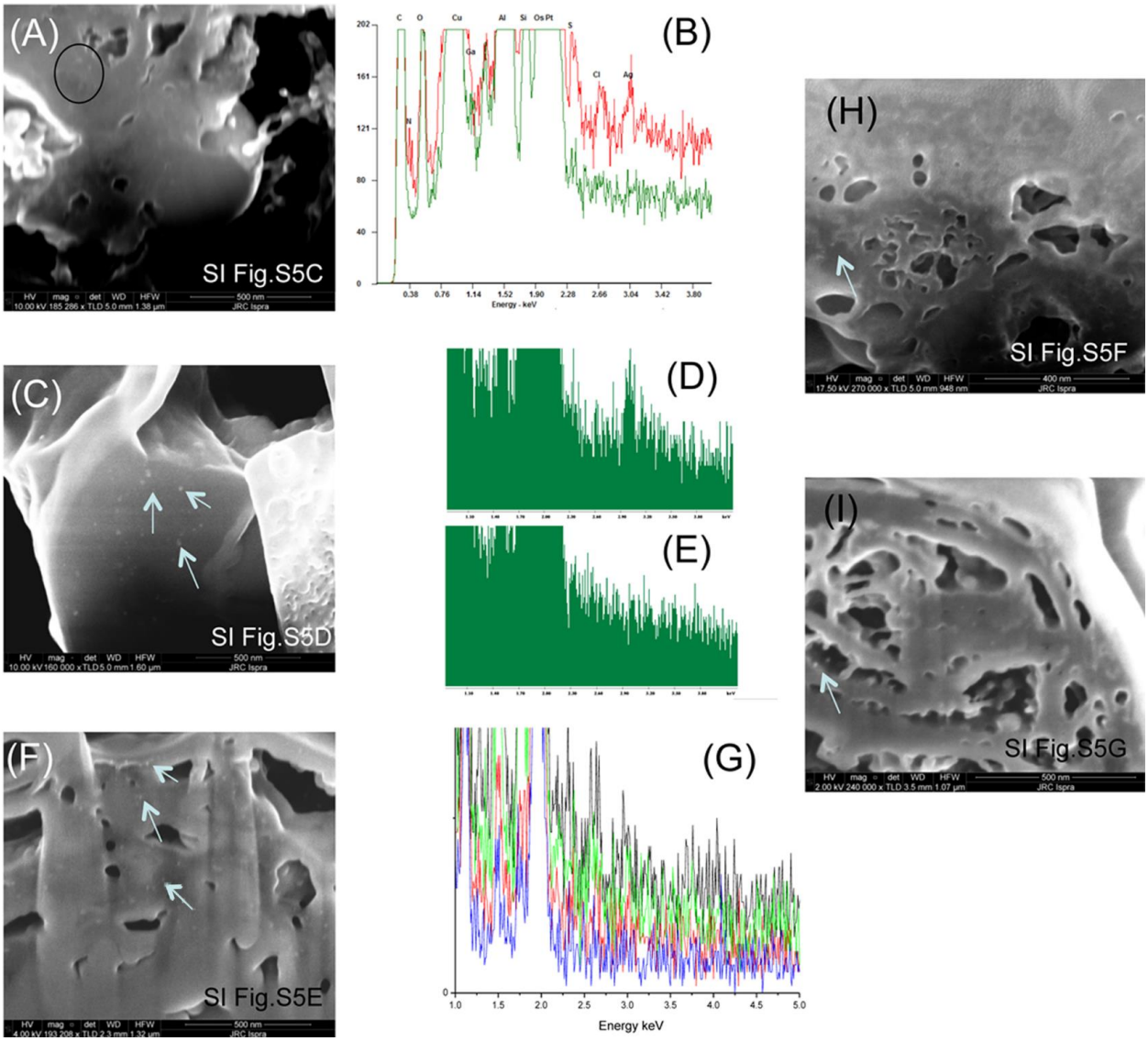

Figure S7. Microscope pictures of figures S5 C to E where Ag signal was detected by EDX (left column). In the middle column, raw EDX data from AgNP regions and background corresponding to each image on the left column. (B) Red line represents the EDX taken from the area indicated in (A), while the green line is the background from an arbitrary position in the cell. (D) represents the data from one of the areas with Ag signal shown in the image (C), while (E) is the background from the same cell. (G) EDX data from different Ag regions are represented with the black, green and red lines while the background is represented with the blue line. Right column: detection of bright spots interpreted as AgNP without EDX signal. Examples of AgNP are pointed out with bright blue arrows.

Detection of AgNP from figures S5 A and B are reported in details in figures 4 and S6 respectively.

8.7. References

1. Falciatore A, Bowler C (2002) Revealing the molecular secrets of marine diatoms. Annu Rev Plant Biol 53: 109–130.
2. Denys L (2004) Relation of abundance-weighted averages of diatom indicator values to measured environmental conditions in standing freshwaters. Ecological Indicators 4: 255–275.
3. Potapova M, Charles DF (2007) Diatom metrics for monitoring eutrophication in rivers of the United States. Ecological Indicators 7: 48–70.
4. Rovira L, Trobajo R, Ibanez C (2012) The use of diatom assemblages as ecological indicators in highly stratified estuaries and evaluation of existing diatom indices. Mar Pollut Bull 64: 500–511.
5. Carvalho RN, Burchardt AD, Sena F, Mariani G, Mueller A, et al. (2011) Gene biomarkers in diatom *Thalassiosira pseudonana* exposed to polycyclic aromatic hydrocarbons from contaminated marine surface sediments. Aquat Toxicol 101: 244–253.
6. Davis AK, Hildebrand M, Palenik B (2006) Gene expression induced by copper stress in the diatom *Thalassiosira pseudonana*. Eukaryot Cell 5: 1157–1168.
7. Wang MJ, Wang WX (2011) Cadmium sensitivity, uptake, subcellular distribution and thiol induction in a marine diatom: exposure to cadmium. Aquat Toxicol 101: 377–386.
8. Miao AJ, Luo Z, Chen CS, Chin WC, Santschi PH, et al. (2010) Intracellular uptake: a possible mechanism for silver engineered nanoparticle toxicity to a freshwater alga Ochromonas danica. PLoS One 5: 15196.
9. Meyer JN, Lord CA, Yang XY, Turner EA, Badireddy AR, et al. (2010) Intracellular uptake and associated toxicity of silver nanoparticles in *Caenorhabditis elegans*. Aquat Toxicol 100: 140–150.
10. Farkas J, Christian P, Gallego-Urrea JA, Roos N, Hassellov M, et al. (2010) Uptake and effects of manufactured silver nanoparticles in rainbow trout (*Oncorhynchus mykiss*) gill cells. Aquat Toxicol 101: 117–125.
11. Kwok KW, Auffan M, Badireddy AR, Nelson CM, Wiesner MR, et al. (2012) Uptake of silver nanoparticles and toxicity to early life stages of Japanese medaka (*Oryzias latipes*): Effect of coating materials. Aquat Toxicol 120–121: 59–66.

12. Greulich C, Diendorf J, Simon T, Eggeler G, Epple M, et al. (2011) Uptake and intracellular distribution of silver nanoparticles in human mesenchymal stem cells. Acta Biomater 7: 347–354.
13. Lok CN, Ho CM, Chen R, He QY, Yu W, et al. (2007) Silver nanoparticles: partial oxidation and antibacterial activities. J Bio Ionrg Chem 12 (4): 527–534.
14. Xiu Z-m, Zhang Q-b, Puppala HL, Colvin VL, Alvarez PJJ (2012) Negligible particle-specific antibacterial activity of silver nanoparticles. Nano Letters 12(8): 4271–4275.
15. Burchardt AD, Carvalho RN, Valente A, Nativo P, Gilliland D, et al. (2012) Effects of silver nanoparticles in diatom *Thalassiosira pseudonana* and cyanobacterium*Synechococcus* sp. Environ Sci Technol 46: 11336–11344.
16. Hildebrand M, York E, Kelz JI, Davis AK, Frigeri LG (2006) Nanoscale control of silica morphology and three-dimensional structure during diatom cell wall formation. J Mater Res 21: 2689–2698.
17. Losic D, Pillar RJ, Dilger T, Mitchell JG, Voelcker NH (2007) Atomic force microscopy (AFM) characterisation of the porous silica nanostructure of two centric diatoms. J Porous Mater 14: 61–69.
18. Bhatta H, Enderlein J, Rosengarten G (2009) Fluorescence correlation spectroscopy to study diffusion through diatom nanopores. J Nanosci Nanotechnol 9: 6760–6766.
19. Sharand AM, Braydich-Stolle LK, Shlager JJ, Dai L, Hussain SM (2008) Can silver nanoparticles be useful as potential biological labels? Nanotechnology 19: 235104.
20. Shah NB, Dong J, Bischof JC (2011) Cellular uptake and nanoscale localization of gold nanoparticles in cancer using label-free confocal Raman microscopy. Mol Pharm 8: 176–184.
21. Rocha A, Zhou Y, Kundu S, Gonzalez JM, BradleighVinson S, et al. (2011) In vivo observation of gold nanoparticles in the central nervous system of *Blaberus discoidalis*. J Nanobiotechnology 9: 5.
22. Pletikapić G, Žutić V, Vinković Vrček I, Svetličić V (2012) Atomic force microscopy characterization of silver nanoparticles interactions with marine diatom cells and extracellular polymeric substance. J Mol Recognit 25: 309–317.
23. Fabrega J, Renshaw JC, Lead JR (2009) Interactions of silver nanoparticles with*Pseudomonas putida* biofilms. Env Sci Tech 43: 9004–9009.
24. Hildebrand M, Kim S, Shi D, Scott K, Subramaniam S (2009) 3D imaging of diatoms with ion-abrasion scanning electron microscopy. J Struct Biol 166: 316–328.

25. Tesson B, Hildebrand M (2010) Dynamics of silica cell wall morphogenesis in the diatom *Cyclotella cryptica*: substructure formation and the role of microfilaments. J Struct Biol 169: 62–74.
26. Abramson L, Wirick S, Lee C, Jacobsen C, Brandes JA (2009) The use of soft X ray spectromicroscopy to investigate the distribution and composition of organic matter in a diatom frustule and a biomimetic analog. Deep-Sea Research Part II 56: 1369–1380.
27. Heymann JA, Hayles M, Gestmann I, Giannuzzi LA, Lich B, et al. (2006) Site-specific 3D imaging of cells and tissues with a dual beam microscope. J Struct Biol 155: 63–73.
28. García CP, Sumbayev V, Gilliland D, Yasinska IM, Gibbs BF, et al. (2013) Microscopic analysis of the interaction of gold nanoparticles with cells of the innate immune system. Sci Rep 3: 1623.
29. Sumbayev VV, Yasinska IM, García CP, Gilliland D, Lall GS, et al. (2013) Gold nanoparticles downregulate interleukin-1β-induced pro-inflammatory responses. Small 9: 472–477.
30. Gusnard D, Kirschner RH (1977) Cell and organelle shrinkage during preparation for scanning electron microscopy: effects of fixation, dehydration and critical point drying. J Microsc 110: 51–57.
31. Linsinger TPJ, Roebben G, Gilliland D, Calzolai L, Rossi F, et al. (2012) Requirements on measurements for the implementation of the European Commission definition of the term 'nanomaterial'. EUR 25404 EN Luxembourg.
32. Guillard RR, Ryther JH (1962) Studies of marine planktonic diatoms. I. *Cyclotella nana*Hustedt, and *Detonula confervacea* (Cleve) Gran. Can J Microbiol 8: 229–239.
33. Guillard RRL (1975) Culture of phytoplankton for feeding marine invertebrates. In: Smith WL, Chanley MH, editors. Culture of Marine Invertebrate Animals. New York: Plenum Press. pp. 26–60.
34. Bopp SK, Lettieri T (2007) Gene regulation in the marine diatom *Thalassiosira pseudonana* upon exposure to polycyclic aromatic hydrocarbons (PAHs). Gene 396: 293–302.
35. University of Alabama (2014) Fixation for SEM. Available:http://bama.ua.edu/~emlab/instructions/sem_fix.html. Accessed 2014 Apr 13.
36. Bozzola JJ, Russell LD (1999) Electron microscopy: Principles and techniques for biologists. Burlington, MA: Jones & Bartlett Learning. 670 p.

37. Drobne D, Milani M, Leser V, Tatti F (2007) Surface damage induced by FIB milling and imaging of biological samples is controllable. Microsc Res Tech 70: 895–903.
38. Schneider CA, Rasband WS, Eliceiri KW (2012) NIH Image to ImageJ: 25 years of image analysis. Nature Methods 9: 671–675.
39. Heymann JA, Shi D, Kim S, Bliss D, Milne JL, et al. (2009) 3D imaging of mammalian cells with ion-abrasion scanning electron microscopy. J Struct Biol 166: 1–7.
40. Levard C, Hotze EM, Lowry GV, Brown GE (2012) Environmental transformations of silver nanoparticles: impact on stability and toxicity. Environ Sci Technol 46: 6900–6914.
41. Stuart EJE, Rees NV, Cullen JT, Compton RG (2013) Direct electrochemical detection and sizing of silver nanoparticles in seawater media. Nanoscale 5: 174–177.
42. Yang W, Lopez PJ, Rosengarten G (2011) Diatoms: self-assembled silica nanostructures, and templates for bio/chemical sensors and biomimetic membranes. Analyst 136: 42–53.
43. Hecky RE, Mopper K, Kilham P, Degens ET (1973) The amino acid and sugar composition of diatom cell-walls. Marine biology 19: 323–331.
44. Hamm CE, Merkel R, Springer O, Jurkojc P, Maier C, et al. (2003) Architecture and material properties of diatom shells provide effective mechanical protection. Nature 20: 841–843.
45. Svetličić V, Žutić V, Pletikapić G, Mišić Radić T (2013) Marine polysaccaride networks and diatoms at the nanometric scale. Int J Mol Sci 14: 20064–20078.
46. Miao AJ, Schwehr KA, Xu C, Zhang SJ, Luo Z, et al. (2009) The algal toxicity of silver engineered nanoparticles and detoxification by exopolymeric substances. Environ Pollut 157: 3034–3041.
47. Navarro E, Piccapietra F, Wagner B, Marconi F, Kaegi R, et al. (2008) Toxicity of silver nanoparticles to *Chlamydomonas reinhardtii*. Environ Sci Technol 42: 8959–8964.

9. Chapter VII

Nanoparticle complexes detection and localization in microscale cells by Transmission Electron Microscopy tomography coupled with Energy-Dispersive X-ray Spectroscopy

Diana C. António[ab], Cesar Pascual Garcìa[c], Douglas Gilliland[a], Teresa Lettieri[d], António J. A. Nogueira[b], Luigi Calzolai[a*]

[a] European Commission - Joint Research Centre, Institute for Health and Consumer Protection, T.P. 203, Via E. Fermi 2749, 21027 Ispra (VA), Italy

[b] Departamento de Biologia & CESAM, universidade de Aveiro, Aveiro, Portugal

[c] formerly, European Commission - Joint Research Centre, Institute for Health and Consumer

[d] European Commission - Joint Research Centre, Institute for Environment and Sustainability, T.P. 270, Via E. Fermi 2749, 21027 Ispra (VA), Italy

Under preparation for submission.

9.1. Abstract

Toxicological studies related to uptake are often complemented by electron microscopy techniques. The most promising methods available for tissue localization are based on sample slicing, multiplying the number of sections to analyze per sample. Although promising, the production of such data sets is demanding and time consuming. In this study, we present an alternative which allows whole cell imaging without the need for sectioning. Cells are prepared for microscopy through a standard critical point drying method and imaged by transmission electron microscopy (TEM)-based tomography, reducing the complexity of sample preparation and data acquisition. The proposed sample preparation procedure is compatible both for TEM and scanning electron microscopy (SEM) analysis. We show the possibility to evaluate the distribution of metals inside the cells. As proof of concept, we exposed unicellular algal cells to metallic and ionic forms of silver and used the 3D-models to localize it inside the cells. Silver complexes bounded to the cell wall and near the cell organelles were determined.

9.2. Introduction

(Eco)toxicology is a high demanding field. Evaluation of endpoints is often based on imaging methods. Recently, the concern with introduction of nanomaterials in many consumer and health products has increased the call for (eco)toxicocogical analysis. Nanoparticle uptake is one of the many mechanisms which could lead to toxic effects. The search for clear and informative methods on the study of nanomaterials impact or mode of action (interaction with the membrane, uptake process, targeting, etc.) has turned nano-research towards microscopy-based approaches, other than molecular techniques. The choices are however limited once screening for elements with size ranges below 100 nm. For instance, optical microscopy, with a maximum resolution of 200 nm, cannot be considered. Fluorescent microscopy, an interesting method regarding the study of cell modifications, has its application limited to fluorescent nanoparticle such as quantum dots. However, many relevant nanomaterials used in food, heath or cosmetic industries are metallic, such as gold, silver, titanium or zinc NP. Such particles have plasmon resonant optical scattering properties which allow its detection by specific techniques such Raman or hyperspectral confocal microscopy [1, 2]. Once again, there are limitations to those methods regarding cell-NP relative localization. Atomic force microscopy (AFM) poses as a good alternative for NP detection and imaging in cells, with high sensitivity regarding NP internalization analysis [3]. This method however is limited to surface interaction. Nanoparticles targeting or intracellular localization are therefore not possible. Finally, electron microscopy techniques are another option to consider. Classic scanning electron microscopy (SEM) imaging can be used on NP uptake studies. As shown before, it is possible to follow the internalization of AuNP by monocytes [4], although, similarly to AFM studies, SEM analysis *per se* is confined to surface analysis. The use of appropriate cell treatment and scanning transmission electron microscopy (STEM) however allows the inspection of the cell interior as well. Coupled with focus ion beam (FIB), cell milling is possible on grid, where a region of interest, or a NP, is found [5]. Though the advantages of a complete study such as STEM-FIB analysis are interesting, the resolution power of the STEM is considerably lower than classical TEM, curtain effect can occur during sample process spoiling the work, and the amount of time required for such study is considerably high. The use of resin embedding or cryopreservation techniques is often used due to the quality of the recorded data. TEM visualization of samples prepared by ultramicrotomy allows the screening of the overall cell and the exact localization of the NP, though this fractionating technique multiplies the amount of grids to image, becoming

extremely demanding and time consuming. When working with unicellular organisms, the use of sample fixation methods and critical point drying (CPD), is an alternative sample preparation method suitable to be used both for SEM and TEM analysis. Through this method cell lipids and proteins are chemically fixed with glureraldehyde and osmium tetroxide, respectively, the sample is dehydrated with ethanol and this is replaced by CO_2, allowing the stability of the cell in vacuum conditions. The proposed sample imaging alternative, uses CPD treated samples to produce 3D tomography of single cells using TEM. TEM analysis has higher resolution and allows cell inspection with no need for sample fractionation. TEM-tomography technique allows whole cell imaging, in few steps, and 3D modelling suitable for NP localization study. The tomography consists on the acquisition of static images at each settled angle which are feed to a modelling software that makes a mathematical reconstruction of the cell in three dimensions. After tomography, EDX analysis can be performed at different angles to evaluate chemical distribution of several heavy elements in the sample (cell and surroundings). This approach was developed for micro-scale cells as microalgae. In this study we have used as model the marine diatom *Thalassiosira pseudonana*, chosen mainly due to its size and silica cell wall (shell). *T. pseudonana* is a unicellular organism of 4-5 µm in diameter [6]. The diatom shell consists on an intricate pattern of nanopores, working has a natural filter. The pores range from 20 to 70 nm in diameter [7] allowing the entrance of pollutants as NP. The rigidity and transparence of the shell helps imaging the cell content regardless cell content shrinkage or deformation, created upon sample preparation by critical point drying. On the context of this work, maltose stabilized AgNP were used to evaluate in cell distribution/localization. The toxicity of maltose stabilized AgNP over *T. pseudonana* has been previously reported [7].

9.3. Materials and Methods

9.3.1 Reagents

The silver nanoparticles were synthesized using maltose as stabilizer. Silver nitrate (AgNO3) (99.9%), ammonium hydroxide (5N in H2O); D-(+)-maltose monohydrate (98%) and sodium borohydride (98%), used for NP synthesis, were purchased from Sigma-Aldrich. Sea salts,

used to prepare diatom culture medium, were purchased from Sigma-Aldrich, and supplemental nutrients (F/2 medium kit) were purchased from the National Center for Marine Algae and Microbiota.

9.3.2 Silver nanoparticles synthesis and characterization

Silver nanoparticles were synthesized via a modified Tollens process, by chemically reducing the complex cation $[Ag(NH_3)_2]^+$ on maltose [8]. Freshly synthesized maltose-stabilized silver nanoparticles (mAgNP) were characterized by Centrifugal Liquid Sedimentation (CLS, figure S1).

9.3.3 Cell culture

An axenic culture of the diatom *T. pseudonana* (strain CCMP 1335) was purchased from the National Center for Marine Algae and Microbiota (NCMA, West Boothbay Harbour, Maine, USA). Cultures were maintained in 3.2% ASW-F/2 medium, at 14°C, under a diurnal light cycle of 13 h light and 11 h darkness and continuous shaking at 100 rpm. Cell density (n), in cells per milliliter, was calculated according to the following formula $n = [(culture\ OD_{450nm}) - (medium\ OD_{450nm}) + 0.0002] / 0.00000006$ [9].

9.3.4 Cell exposure

Cultures of 10^6 cells/mL were exposed to 50 µM mAgNP or to 10 µM $AgNO_3$ for 48 hours before harvesting. A culture lacking silver was prepared as negative control for uptake. Cultures of 20 mL were prepared in triplicate for each condition. Incubation started before diurnal light phase.

9.3.5 Samples preparation for TEM imaging

After incubation, 20-50 $x10^6$ cells were harvested and kept on ice. Cell pulls were immediately fixed with 2.5% gluteraldehyde and stained as published before [5]. Few exceptions were introduced: i) OsO_4 concentration, used for lipid fixation, was reduced to

half; ii) all centrifugation steps were performed at 580x g for 5 min, to avoid cell damage and iii) after lipid fixation, washing steps were performed using MilliQ water. After dehydration, the ethanol content was replaced by liquid CO_2, according to the CPD method. Sample powder was dispersed in few microliter of absolute ethanol, by gentle reflux, spotted into C-Cu coated grids, and left to dry overnight at 4˚C. Grid spotting was also tested by friction of the grid over the sample powder with similar results in terms of cell shape, however this method revealed high incidence of big cell aggregates, not suitable for tomography-based analysis.

9.3.6 Transmission electron microscopy and EDX analysis

Images were acquired using a JEOL JEM 2100 TEM microscope at 200 KeV. The system was equipped with a Quantax EDS (Bruker) for EDX analysis, with element spectral resolution and sensitivity down to carbon. Grids were mounted on a high tilt holder (EM-21311 HTR, JEOL) and TEM was fully aligned before sample screening. Once a single cell was found, far from the grid boarder, the optical path was assured to be aligned and a tomogram series was acquired with *SerialEM* software (Boulder Laboratory). Prior to image series acquisition, maximum allowed rotation is determined. High tilt holder allows rotation from -60º to 60º, and selected cells were imaged for at least 60º rotation amplitude. The software automatically corrects grid deviations, avoiding high shifting of the cell. One image was acquired at each rotational degree and autofocus was automatically applied at each two degrees. Afterwards, chemical mapping of the cells was performed with *ESPRIT* software (Bruker) for, at least, the neutral stage (zero angle). When sample degradation was not visible other chemical maps were acquired at higher tilt angels. Several elements were mapped simultaneously, including carbon, silicon, chlorine, silver and osmium.

9.3.7 Image processing and 3D reconstruction

Tomogram series were processed using *IMOD 4.5* software for alignment and reconstruction of a 3D model of the cells. Gold beads were not added to the samples, consequently, the image alignment was performed using a fiducialless approach for single axis samples. Images are visually inspected before analysis. Images were the cell is covered or were the grid spacers are evident are discarded from analysis. Manual correction of outlier was performed

in order to optimize the calculated model. Final reconstruction consists on a set of 3D points calculated based on the alignment all feed images. Hereafter, a rotational model and a series of Y stacks were available.
Cell model stacks were used for localization of the mapped elements in the cell.

9.4. Results and discussion

Maltose-stabilized AgNP were characterized by CLS revealing a monodispersed, according to the particle number distribution, with an average size of 14 nm (figure S1). Cell incorporation of mAgNP in *T. pseudonana* was previously described by Cesar and colleagues [5]. With a smaller size than the shell pores (20 to 72 nm), mAgNP were expected to be able to enter the diatom shell and interact with the cell membrane.
After 48 hours incubation cells were harvested and prepared for TEM analysis. At first cells were washed in PBS to remove any excess of particles, reducing false positive results due to displacement of free particles. A first fixation step with gluteraldehyde was used to block the cell metabolism, keeping the proteic structure of the cell, whereas a second fixation with OsO_4 was used to preserve the lipidic membranes. Secondary fixation was attempted with 1% and 2% osmium tetroxide showing no difference on the final results (data not shown). Substitution of water content by ethanol was performed in order to maximize CPD efficiency, as CO2 is not sufficiently miscible with water. The CPD removed the liquid content of the cell without major morphology losses, allowing the visualization of the whole cell with no need for further sample processing or tissue contrast improvements. Samples show good contrast and the detail of the shell structure and organelles content achieved is quite satisfactory. Disregarding the shrinkage of the organelles, common also to plant cells [10], we found CPD to be a successful preparation method. For diatoms, the sample preparation protocol, schematized in Figure 1, was found reproducible. Sample dispersion in 100% ethanol was attempted, for grid spotting, in comparison with physical attachment of the dry sample, by friction. Since samples were degassed in the sample holder, prior to mounting, the added ethanol evaporated with no hazardous effects to the sample or imaging process. In fact, cells dispersion on the grid was improved, with less cell aggregates visible. A good distribution of the cells in the grid is crucial for tomography since adjacent cells can cover the target cell at various tilt angles. Overlapped cells images can hardly be used for the model reconstruction.

Figure 1: Flow chart of the cell preparation procedure for EM analysis and TEM image of a cell exposed to 50 µM mAgNP, prepared accordingly.

The viability of this sample preparation method for SEM analysis on other type of cells had been proved by our group on an uptake study, showing the interaction of AuNP with THP-1 monocytes [4].

Reconstructions were made from the alignment of an average of 120 images per cell, in average. The fiducialess alignment revealed to be feasible, however the use of reference particles (fiducials) is expected to decrease the process complexity. Commercialy available grids with pre-spotted AuNP are therefore recommended. In such situation, additional EDX mapping of Au would allow differentiation of the reference particles from the studied ones. Furthermore, the reconstruction software allows removing reference particles from the final model.

Finalized cell models were clean and sharp enabling discrimination of the cell components as shown on figure 2.

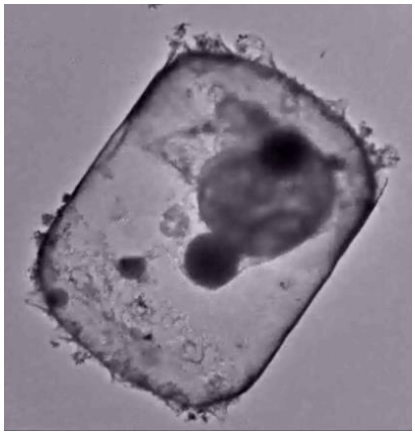

Figure 2: Capture of a computer tomography reconstruction of a cell exposed to AgNP.

With the reconstruction software, a full 3D model was produced and presented as a movie of the cell rotating on a central axis (see Movie S1). Moreover, the software allowed as well an inspection of the model stacks on the X/Y/Z axis.

Due to the destructive nature of the EDX analysis, chemical maps were recorded after acquisition of tomographic images. The damaging effect of the electron beam on the analyzed region enables the acquisition of data on a maximum of 3 tilt angles. Figure 3 shows the overlapping of the EDX maps of silver, silicon and carbon with the TEM image in bring field. The overlapping revealed the presence of silver clusters in several areas around the shell but also revealed two areas possibly inside the cell. To clarify the localization of these clusters, an inspection of the Z stacks was performed and silver clusters were found to be inside the shell. One of the clusters was found at the same level as the nucleus, supporting the thesis that it was inside the cell membrane. The second cluster on the other hand was found closer to the shell. Since the mapping of phosphorous is not possible with the available instrumentation, cell membrane was not imaged. Consequently, we could confirm only the passage of the silver through the shell pores, but not its internalization. However, the region demarked with a circle in figure 3 (bottom left image) is located at the same Z-stack as the cell organelles and the EDX map shows evidences of carbon overlapping. Full Z-stack reconstruction can be seen in supplementary information (Movie S2). Mapping of additional elements could provide further information on the silver interactions.

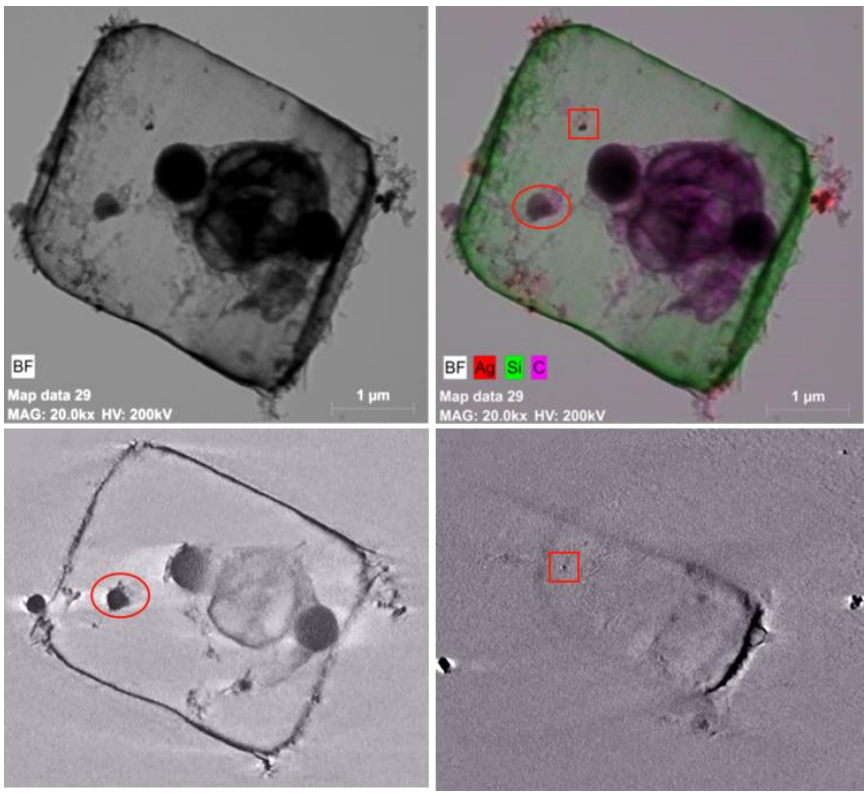

Figure 3: Bright field STEM image of a cell exposed to 50µM AgNP (top left) and the overlapped EDX maps (top right) for silver (red), silicon (green) and carbon (pink). Silicon content refers to the shell and carbon represents organic matter i.e. cell organelles. Metallic silver, corresponding to silver complexes or nanoparticles, appears in red. Silver clusters (red circle and square) were localized within the cell as evidenced by the image stacks (bottom). Cluster evidenced with red square appears on a top stack of the cell (bottom right) while the one with a circle appears on an intermediate stack (bottom left), at the level of the organelles (nucleus and chloroplasts).

Figure 4 reveals the presence of silver-chloride complexes. In marine samples, silver tends to complex with chloride [11], explaining the higher silver signal overlapping the material absorbed to the shell. Using this approach, interaction of silver with elements specific of a cell organelles can therefore be evaluated. For instance, it is known that iron is a key element on diatoms development and can be found in the frustule [12, 13]. Also manganese is mainly found in chloroplasts, being essential for superoxide dismutase activity and photoreaction II of photosynthesis [14, 15].

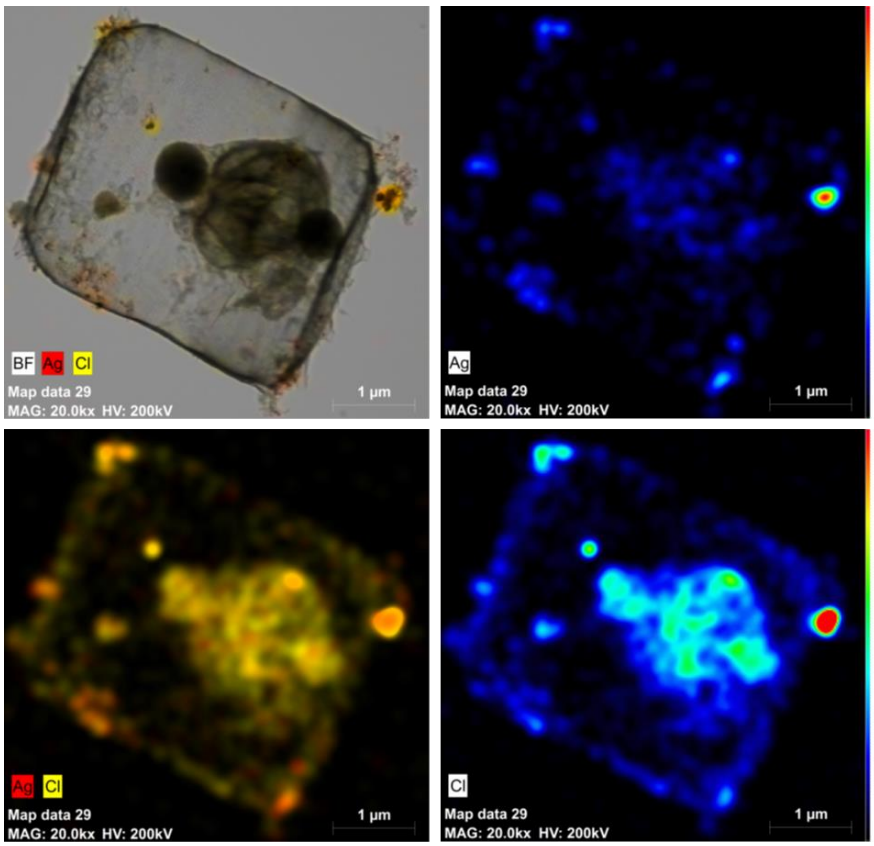

Figure 4: Top left panel shows the overlapped bright field STEM image of a cell exposed to 50µM AgNP and the EDX maps for silver (red) and chloride (yellow). The EDX signal for both silver and chloride is shown in bottom left panel. Top and bottom right panels show the recorded relative intensity signal of silver and chloride elements, respectively.

Cells exposed to $AgNO_3$ showed a faint signal for silver, spread along the cell, even at increased voltage (figure 5). EDX analysis is not compatible with ionic content evaluation allowing only the screening of the metallic fraction. EDX method can therefore discriminate only precipitated silver clusters. The complexation of silver ions with organic elements, such as sulphur, producing non soluble species [16], or the previously mentioned complexation with chloride, could explain the remaining faint signal in the cell region.

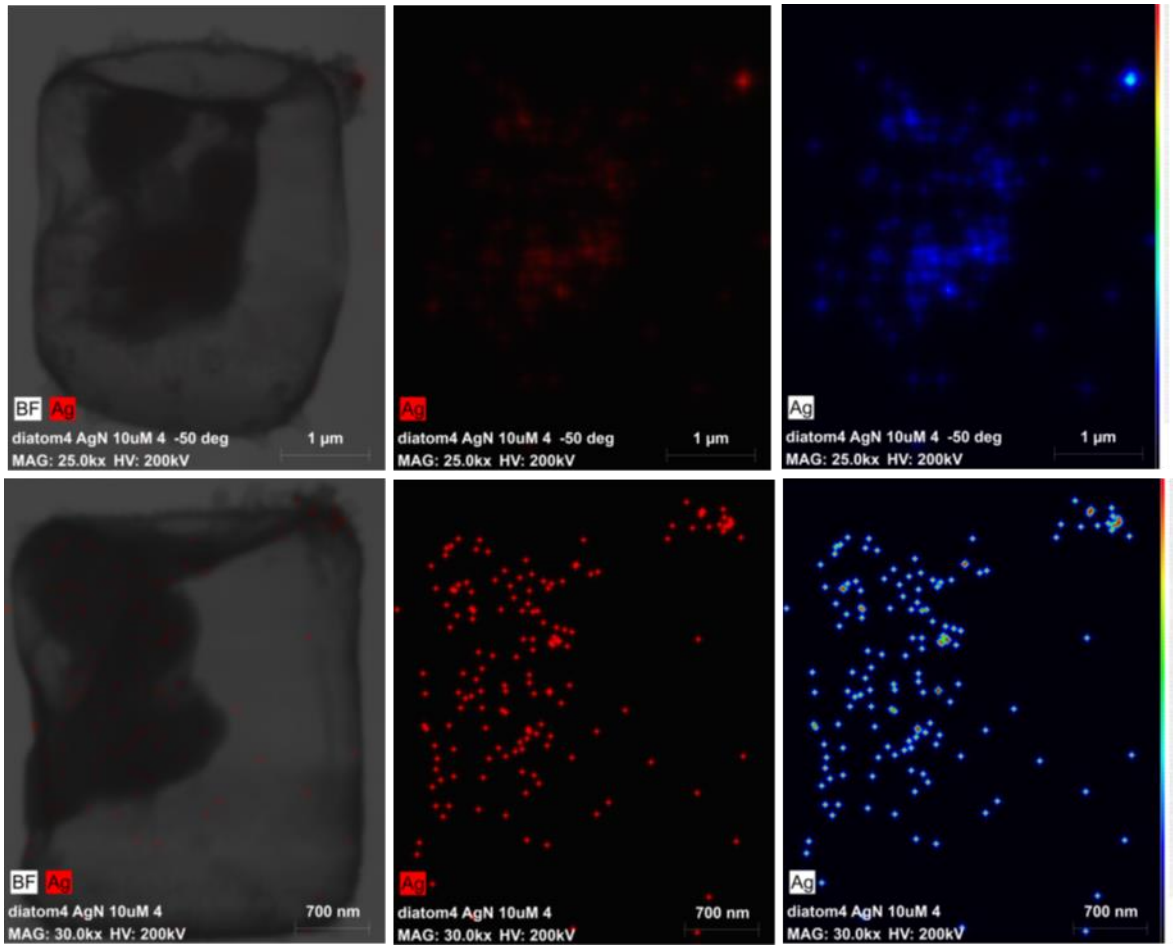

Figure 5: Bright field STEM image of a cell exposed to 10µM $AgNO_3$ in two different angles, and overlapping signal for silver, (top and bottom panels, respectively). The EDX maps for silver are shown in red and its relative intensity is presented on the right panels.

9.5. Conclusion

Regardless of the EM availability on research laboratories, this is certainly a technique of common use on the nano-(eco)toxicology field. Here we propose a straight forward method for uptake analysis that can partially replace the need for complex sample post-processing techniques based on sample slicing or milling. Moreover, it produces samples stable enough to be stored for few weeks, or to be shipped to other labs were instrumentation (TEM-EDX) is available. The sample preparation method used is also compatible with SEM imaging [5]. We demonstrate method feasibility for evaluation of complexed silver forms and its distribution within whole micro-scale cells. The major advantage of this process is the possibility to evaluate intracellular localization for heavy elements in whole cells. In addition, the chemical

data acquired can be used to discriminate the 3D model regions, enriching the model informative power [13]. Morover, chemical maps recorded at different tilt angles are expected to reduce uncertainty in cell regions discrimination.

Acknowledgments

We thank Dr. Paula Nativo for the nanoparticles and Joaquin Pinto Grande for technical assistance.

9.6. Supplementary information

9.6.1 I – Characterization of AgNP

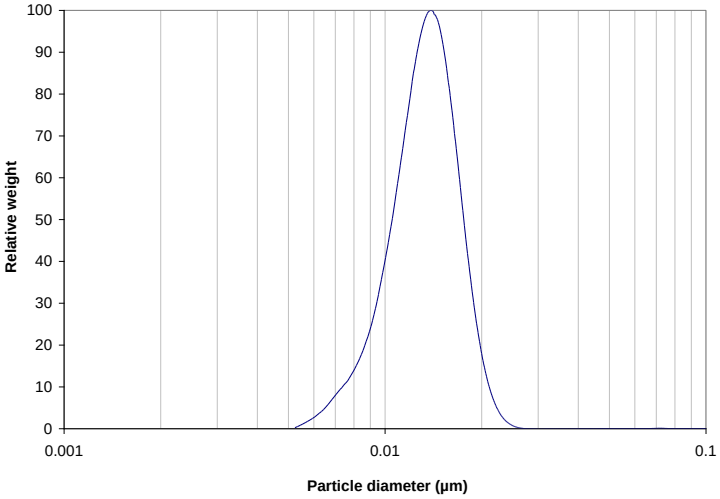

Figure S1. Nanoparticles size distribution, by weight, analyzed by CLS.

The graph above shows the size distribution of the produced maltose-stabilized AgNP, acquired by CLS. The adsorption to size conversion assumes a particle density equal to bare silver. The data reports a narrow size distribution with a single peak at 14 nm.

9.6.2 II – Tridimensional reconstruction model

Movies S1 and S2 show the reconstruction model of a diatom cell exposed to AgNP. The tridimensional model (Mocie S1) was reconstructed based on a pull of 120 images recorded at every ±1 degree. Movie S2 refers to the Z-stack reconstruction of the same cell presented on Movie S1.

Movie S1 Tridimensional reconstitution of a diatom exposed to AgNP. (see file in the annexed CD room)

Movie S2 Z-stack reconstitution of a diatom exposed to AgNP. (see file in the annexed CD room)

9.7. References

1. Shah, N.B., J. Dong, and J.C. Bischof, *Cellular Uptake and Nanoscale Localization of Gold Nanoparticles in Cancer Using Label-Free Confocal Raman Microscopy.* Molecular Pharmaceutics, 2011. **8**(1): p. 176-184.
2. Rocha, A., et al., *In vivo observation of gold nanoparticles in the central nervous system of Blaberus discoidalis.* Journal of Nanobiotechnology, 2011. **9**: p. 5-5.
3. Pletikapić, G., et al., *Atomic force microscopy characterization of silver nanoparticles interactions with marine diatom cells and extracellular polymeric substance.* Journal of Molecular Recognition, 2012. **25**(5): p. 309-317.
4. García, C.P., et al., *Microscopic Analysis of the Interaction of Gold Nanoparticles with Cells of the Innate Immune System.* Scientific Reports, 2013.
5. García, C.P., et al., *Detection of Silver Nanoparticles inside Marine Diatom <italic>Thalassiosira pseudonana</italic> by Electron Microscopy and Focused Ion Beam.* PLoS ONE, 2014. **9**(5): p. e96078.
6. Belcher, J.H. and E.M.F. Swale, *Species of Thalassiosira (Diatoms, Bacillariophyceae) in the plankton of English rivers.* British Phycological Journal, 1977. **12**(3): p. 291-296.
7. Burchardt, A.D., et al., *Effects of Silver Nanoparticles in Diatom Thalassiosira pseudonana and Cyanobacterium Synechococcus sp.* Environmental Science & Technology, 2012. **46**(20): p. 11336-11344.
8. Kvítek, L., et al., *The influence of complexing agent concentration on particle size in the process of SERS active silver colloid synthesis.* J. Mater. Chem., 2005. **15**(10): p. 1099-1105.

9. Bopp, S.K. and T. Lettieri, *Gene regulation in the marine diatom Thalassiosira pseudonana upon exposure to polycyclic aromatic hydrocarbons (PAHs).* Gene, 2007. **396**(2): p. 293-302.
10. Bray, D.F., J. Bagu, and P. Koegler, *Comparison of hexamethyldisilazane (HMDS), Peldri II, and critical-point drying methods for scanning electron microscopy of biological specimens.* Microscopy Research and Technique, 1993. **26**(6): p. 489-495.
11. Chambers, B.A., et al., *Effects of Chloride and Ionic Strength on Physical Morphology, Dissolution, and Bacterial Toxicity of Silver Nanoparticles.* Environmental Science & Technology, 2013. **48**(1): p. 761-769.
12. Ellwood, M.J. and K.A. Hunter, *The incorporation of zinc and iron into the frustule of the marine diatom Thalassiosira pseudonana.* Limnology and Oceanography, 2000. **45**(7): p. 1517-1524.
13. de Jonge, M.D., et al., *Quantitative 3D elemental microtomography of Cyclotella meneghiniana at 400-nm resolution.* Proceedings of the National Academy of Sciences, 2010. **107**(36): p. 15676-15680.
14. Wolfe-Simon, F., et al., *Localization and Role of Manganese Superoxide Dismutase in a Marine Diatom.* Plant Physiology, 2006. **142**(4): p. 1701-1709.
15. Raven, J.A., *Predictions of Mn and Fe use efficiencies of phototrophic growth as a function of light availability for growth and of C assimilation pathway.* New Phytologist, 1990. **116**(1): p. 1-18.
16. Thalmann, B., et al., *Effect of humic acid on the kinetics of silver nanoparticle sulfidation.* Environmental Science: Nano, 2016. **3**(1): p. 203-212.

10. General discussion and conclusions

Nanotechnology has become an appreciated tool in many industrial sectors. The use of nanomaterials has spread in number and functional application in the last decades. Consequently, a concern regarding its potential (eco)toxicological impact has grown. Furthermore, it raised the need to legislate the use of nanomaterials especially in products released to the end costumer, such as cosmetics or food. Both areas, scientific research and policy, grew the need to develop methods able to detect and characterize nanomaterials. Several methods have been developed and adapted to the evaluation of nanoparticles during the last decades, although none has yet been proved comprehensive. The combination of several techniques is usually used to retrieve enough data to characterize a material. Many presented approaches are optimized based on dispersions of nanoparticles in simple solvents. The transposition of such studies to real samples, were the complexity of the matrices are extremely high, is usually not straightforward. Not only a full characterization is required but it must be robust enough to overcome the expected particle modifications, such as particle surface coating which affects particle-particle and particle-surfaces interactions. In this work we tried to grasp this issue using different techniques which can complete themselves toward a more trustable and complete characterization of nanoparticles in complex matrices. Two different types of nanomaterials were evaluated, titania and silver nanoparticles. Both materials are expected to enter the aquatic ecosystem at the life endpoint of the nanoparticle-containing products or simply by nanoparticle leaching from the referred products. Several studies have analysed nanoparticle leaching and fate of nanomaterials in waste water treatment plants [68]. Waste water treatment plants and soil are the first expected reservoirs although natural soil leaching and discharge of water treatment plants are likely to be the main routes for contamination of aquatic system.

As commented before, the broad use of titania nanoparticles in several industrial sector augmented the probability of detection of engineered particles in the environment. In this study we focused on detection of titania NP in sunscreen lotion, following an exhaustive method setup using cosmetic and food additives. The use of sun protection is increasing from year to year subsequent to cancer prevention actions, increased access to information and adoption of healthier habits. In this scenario there is a direct entry route of NP in the ecosystem. In fact, the initial

sample treatment used for analysis consisted in few more than the dilution of the sunscreen lotion in an aqueous solution, as expected in recreational areas. On *Chapter I* we showed an exhaustive characterization of additive titania nanomaterials, namely pigment 6 white, used in cosmetics, and food additive E171. Pigment 6 white is a coated non photocatalitic material dispersible in deionised water. E171 is a food additive, sold in a starch mixture, also dispersible in water. Determination of material type was performed by Raman spectroscopy, evaluation of particle stability at various pH values was performed based on Z-potential and sample dispersion protocol was optimized. CLS was used to qualitatively evaluation the particle size distribution with respect to the different sample treatments. Real evaluation of particle size by CLS is possible only when particle density is known. In complex matrices nanoparticles interact with the matrix components which can affect the particle density, compared to bare materials, by promoting particle aggregation or agglomeration, or simply by coating the nanoparticles surface. To overcome this limitation, samples were analysed by AF4/UV-Vis/DLS. UV-Vis was used to follow the elution process but it must be remarked that titania absorbance, in the 250-300 nm range, is non-specific. DLS cannot deal with polydispersed material but AF4 allows the elution of the particles based on size. AF4 sample fractions were also collected and analysed by ICP-MS to confirm the presence of titanium in the sample and to quantify it. Total Ti concentration detected in each fraction supported the particle size distribution found both by DLS and CLS, revealing the presence of aggregated or agglomerated material. This study set the basis for TiO_2 NP analysis in sunscreen lotion. A similar approach was presented in *Chapter II*, were lotions were dispersed in aqueous solution and sonicated before injection into an AF4/UV-Vis/DLS hyphenated system. The lotion used in this study was spiked with non-coated titania nanoparticles. As previously tested by our group in commercial sunscreen lotions, the particle coating used in sunscreens does not affect nanoparticles characterization based on AF4, UV-Vis, DLS and ICP-MS analysis (data not shown). The matrix content was indeed the only variable to be considered, influencing the sample dispersion strategy (Dr. Claudia Cascio personal communication). The formulation prepared by AHAVA for this study showed to be easily dispersible in aqueous solution. Tego care 450 is a surfactant used in the formulation of lotions. Therefore it was used to facilitate the dispersion of the lotion-containing nanomaterials. Contrary of what shown in *Chaper 1*, UV-Vis and DLS

revealed not suitable for detection and size determination of such materials on fatty matrices. In fact both systems reported false positive reads when lotion not spiked with titania NP was analysed. The unspecificity of the UV-Vis signal was already expected, as proteins absorb at the same wavelength range. The results of DLS analysis however were surprising. Sizing of materials of 100 nm, in average, was reported for both spiked and non-spiked lotions. Considering the use of sonication, to optimize particle dispersion, and the presence of fatty components in the lotion matrix, we presume that the signal comes from micelles formed during sample preparation. To overcome the difficulties of analysis of lotion samples, ICP-MS was also used, allowing confirmation of Ti presence in the sample and determination of its concentration. In this study we made another advance, showing the possibility to use ICP-MS for Ti quantification on non-digested samples also in flow-mode, hyphenating the system as an end-detector to the AF4/UV-Vis/DLS chain. The fact that ICP-MS is an expensive and not broadly available technique required the adoption of alternative methods. Inverse supercritical CO_2 extraction was tested as alternative sample preparation method for the same lotions in *Chapter III*. Supercritical CO_2 extraction as a way to remove lipids from lipidic formulations have been patented already in 1984 [96]. In our work it proved very useful in evaluating TiO_2 NP by AF4/UV-Vis/MALS techniques. The simplification of the sunscreen lotion matrix allowed direct dispersion of the extract in deionised water and reduced the background signal recorded by UV-Vis. In fact, the reduction of the background noise allowed not only the use of UV-Vis as an alternative size determination method, the MALS. MALS analysis of anisotropic materials, like the spiked TiO_2 NP, allows not only the determination of its molecular weight, as usually used in protein evaluation, but also the determination of its radius of gyration. This last value can be used to calculate the average particle size of the eluted particles based on a fitting model. Although particles shape cannot be accessed by MALS, the shape factor can be calculate based on the radius of gyration considering the hydrodynamic radius is known [33, 97]. The simplified matrix is expected to translate in accurate DLS measurements by removing the micelle formation problem. The hydrodynamic size is not available for this sample and thus it is not possible to determine the shape factor. However, the MALS data were best fitted with the “random-coil” model, suggesting the presence of non-spherical particles. The presence of non-spherical particles is also shown in the TEM images acquired later. Regarding sample stability trough the $scCO_2$ extraction

process, data was not conclusive. The effects on particle aggregation were not fully evaluated, however TEM analysis revealed aggregation on the non-treated lotion as well. It is therefore not excluded that the recorded particle aggregation comes from the instability of the material in the lotion matrix. Overall, the methods described in the first 3 chapters are likely to be suitable for evaluation of titania NP in environmental samples even at lower concentrations. The characterization potential achievable by combination of inverse scCO2, DLS and MALS is expected to be enough for evaluation of commercial products as legally required. It is also relevant for evaluation of material used in toxicological studies however, attention must be paid to possible modifications of the material over time. As mentioned by Al-Kattan and colleagues, evaluation of pristine NP toxicity may not give enough information on ecological impact of the material due to the modified characteristics of the leached materials compared to the primary additive form [98].

In the case of silver-based nanomaterials the picture is different. After introduction of digital cameras, the disposal of silver nitrate waste products decreased exponentially, decreasing consequently its ecological impact. However, the antimicrobial properties of silver are being exploited to a greater extent. Nanoparticulated silver was shown to be a reservoir of silver ions of slow release and therefore its use increased in the health sector. Additionally, it has applications in the textile industry. Environmental release of silver forms may have decreased but is still a reality. Moreover, most of the new silver-containing products are directed to the general public, poorly aware of the potential impact of misuse and disposal of such products for the ecosystems and for public health [60, 99, 100]. Detection of silver in the environment and evaluation of its toxic potential is extremely important. Silver nanoparticles can be silver ion reservoirs, therefore toxic agents, also in the environment depending of the modifications they suffer. Their potential toxicity may affect not only the bacterioplankton in aquatic ecosystems but possibly also other organisms at the lower trophic levels, creating unbalance. It is known that AgNP can impair cell growth also in phytoplanktonic species such as diatoms and chlorophytes [89, 91] although comparison of studies is usually not possible due to the lack of information regarding nanoparticles properties [101]. For the detection of silver nanoparticles in environmental-like conditions we used two different approaches: i) characterization of nanoparticles in natural organic matrices and ii) evaluation of AgNP behaviour in marine systems. We have attempted a similar approach to what was used for titania

NP characterization in the evaluation of AgNP. Combination of AF4, UV-Vis, DLS and ICP-MS were evaluated with AgNP dispersion. The first approach, presented on *Chapter IV*, was to determine the capacity of the AF4 system in characterization of low concentrations of silver nanoparticles coated with organic compounds. Alginate was chosen to mimic presence of organic matter in the system due to its molecular simplicity. Separation of AgNP was obtained by AF4, starting from a previous work reported in literature [102]. In the case of metallic particles, there is one advantage on the particle detection area: metallic particles have specific LSPR which allows it's detection by UV-Vis. Spectroscopic analysis of metallic nanoparticles allows determination of size and concentration of a metallic particle based on its absorption wavelength, as shown for gold nanomaterials [103]. Spectroscopic-based evaluation of AgNP follows the same rule, indeed it is usually used to follow the synthesis of silver nanomaterials [104]. Silver nanoparticles have a specific LSPR between 400 and 500 nm, depending on size. On the other hand, MALS analysis is limited to the detection (and molecular weight determination) since silver nanoparticles do not show angular dependence of the scattered light. Verification of the AF4 separation suitability with bare AgNP showed size dependent elution time. Characterization of AgNP-alginate coated materials was attempted, showing variation of the elution time of bare *versus* coated particles of same core size. Approximate nanoparticle size determination based on AF4 retention time is possible for particles of same nature however, the presence of organic materials changes the membrane-particle interaction decreasing the retention time and thus underestimating the particle size. Charge screening was attempted by adding ammonium carbonate. We indeed optimized the elution in terms of retention time however the recovery was compromised. In fact, the increase of ionic strength is known to influence the separation of nanomaterial by field-flow fractionation [105]. DLS analysis in flow-mode was performed near the limit of sensitivity nevertheless, we showed that it is an interesting resource for size determination. Membrane coating with alginate excess present in the injected sample cannot be ruled out. To evaluate this variable samples should have been somehow washed although, could represent loss or modification of the material. Considering the limited sensitivity of the AF4/DLS system showed in this work we consider that it should not be a useful approach for detection in environmental samples. The simplicity of the analysis allows detection and quantification of AgNP in organic matrices in less than an hour. Validated the

AF4/UV-Vis/DLS approach, another study was conducted with the same material (AgNP-alginate) in high ionic strength conditions, mimicking marine environments (presented in *Chapter V*). The experiment was performed at the same conditions one would cultivate a marine organism, with constant mixing and temperature and exposed to a fixed light:dark regime. Unlike AgNP dispersed in deionised water, the AF4/UV-Vis signal for AgNP incubated in water at 3.2% salinity is undetectable after two days, even if organic matter is present in the system. In fact, AgNP behaviour in high ionic strength conditions was evaluated in a shorter time frame by UV-Vis revealing complete aggregation of the material. Bare particles were found to completely loss their LSPR signal at 430 nm after 30 minutes, in opposition to the two hours recorded for AgNP-alginate complexes, consequence of particle aggregation. DLS analysis, although not suitable for polydispersed materials, gives a clear qualitative indication of the presence of bigger particles or aggregates. The recorded Z-averages higher than 100 nm from the first time point, considering a primary particle size of 60 nm, reveals the immediate initiation of the aggregation process once NP enter in contact with chloride. Similar results were found when AgNP were complexed with humic acids, a component of the organic matter of higher molecular complexity. CLS analysis of the complexed nanomaterials after 10 minutes incubation in salty water revealed an extremely low signal close to the limit of detection of the system. AgNP-alginate complexes showed a maximum signal near 60 nm while bare particles showed a slightly lower signal and higher size (with maximum signal around 70 nm). CLS results were confirmed by spICP-MS where presence of particles near 55 nm, for bare material, and bimodal distribution near 55 and 75 nm, for complexed material, were detected. After two days incubation the signal was not detectable for either materials. Aggregates were not revealed in these techniques however detection range was set up to 200 nm. This study revealed that NP exposure to extreme conditions for long periods can hardly be evaluated by any of the proposed methods. However, organic matter was found to have a protective effect over AgNP, to a certain extent. Considering the simplicity of our model system, further studies in environmental samples must be performed to evaluate the application of such tools for detection of silver nanomaterials in real samples.

In general, characterization of AgNP in natural-mimicking waters as proven of scares outcome considering its low stability and high interactivity with organic compounds. The informative power (and sensitivity) of the presented techniques regards the

toxicologic impact of the materials is considerably low. Legislation regarding nano-wastes and its impact in the environment is not available. Up to now, only detection of pollutant metals for evaluation of water status is regulated [106]. The need for AgNP quantification is therefore irrelevant. On the other hand, as a toxic compound, its impact in the ecosystem is of high relevance. Therefore, a different approach was taken in the study of these materials. Electron microscopy is retained the most reliable technique for nano-characterization and is broadly used in (eco)toxicology. Consequently, it was chosen as prevalent method for AgNP detection and characterization in biological samples. In *Chapter VI* we present a proof of concept for AgNP evaluation in single cells. High concentration of AgNP was used for cell exposure in order to increase the probability to find cells with incorporated particles. The study consisted of SEM-FIB detection and characterization of AgNP interacting with diatom cells. Diatoms were used as model organism due to their size and structural characteristics (rigid outer shell composed of different size and shape nano-pores). We have combined SEM imaging with STEM mode to evaluate the relative position of the nanoparticles with regard to the cell. SEM imaging consists of a scan of the sample surface revealing the cell morphology. In this mode it is possible to image NP adsorbed to the outer diatom shell. The STEM mode works similarly to TEM imaging. By applying higher voltage it is possible to image the cell interior. In this mode imaged nanoparticles can be either in- or outside the cell. Nanoparticles which were plausible to be inside the cell were further analysed by milling. Using the focused ion beam the cell was 'sliced' *in situ*. The relative position of the material can then be confirmed and EDX analysis can confirm their chemical composition. SEM-FIB analysis was proven viable although technically demanding and time consuming. EDX showed quite promising for identification of materials inside the cell and consequent detection of toxicants in non-ionic forms. The drawbacks of FIB milling, namely possible sample displacement and curtain effect, invite for development of alternative methods. In *Chapter VII* we present an alternative method for evaluation of nanoparticles interacting with microorganisms. Using the same model organism and exposure conditions as presented on *Chapter VI* we evaluated the flexibility of the preparative method for TEM-based analysis. Furthermore we tested the feasibility of uptake evaluation on whole cells. Our results showed that the classic fixation with glutaraldehyde and osmium tetroxide followed by critical point drying are suitable for preparation of diatom cells for both SEM and

TEM analysis without further treatment. In this particular study cells spotted in carbon-cupper grids were placed on a high tilt specimen holder. This holder allows the rotation of the grid in two senses, around a fixed axis, to a total of 120 degrees. Images acquired at every degree were used to reconstruct a tri-dimensional model of the cell. Unlike SEM-FIB analysis, 3D-TEM analysis do not require post processing since transmission-based analysis allow evaluation of several focus planes (throughout the cell) without slicing. Additional information retrieved by EDX mapping of selected chemical elements allows discrimination of the image components. De Jonge and colleagues have previously shown the application of EDX coupled with 3D tomography to study diatom cells, differentiating components such as outer shell, cytoplasmatic membrane or organelles based on their main elemental constituents [38]. The innovative part of our work was the ability to differentiate between nanoparticles absorbed or internalized and to infer their relative position. Furthermore, by controlling the co-localization of different elements we could obtain information on the modification of nanoparticles in a cell environment. For example, chloride and silver co-localize mainly in the clusters adsorbed to the outer shell pointing to the presence of AgCl forms, derived from oxidation of the pristine material. Overall, we have shown a sample preparation method suitable for TEM and SEM analysis and a procedure suitable for silver nanoparticle localization in whole cells. Moreover, the presented method is not limited to the study of diatoms as, theoretically, any microorganism can be processed in similar way. Also, the nanomaterial of interest can differ, being only limited to the discriminative capacity of the EDX and the chemical composition of the cell. For instance, the evaluation of silica nanoparticles in the chosen model organism (diatom) would not be possible since the organism outer shell is of the same material. Additionally, we were able to detect cell-interacting AgNP at exposure concentrations of 10 µM (data not shown).

We think that the proposed TEM-EDX tomography method, although complex, can help evaluating AgNP-cell interactions such as the surface area uptake dependency. We believe such work contribute to unveil the AgNP mechanism of action and could be applicable to evaluation of natural samples, assuming a detectable silver concentration is present.

11. References

1. Calzolai, L., D. Gilliland, and F. Rossi, *Measuring nanoparticles size distribution in food and consumer products: a review.* Food Additives & Contaminants: Part A, 2012. **29**(8): p. 1183-1193.
2. Aitken, R.J., et al., *Manufacture and use of nanomaterials: current status in the UK and global trends.* Occup Med (Lond), 2006. **56**(5): p. 300-6.
3. *Commission Recommendation of 18 October 2011 on the definition of nanomaterial*. Official Journal of the European Union.
4. *Regulation (EC) No 1223/2009 of the European Parliament and of the Council of 30 November 2009 on cosmetic products*, in *Official Journal of the European Union*.
5. *Regulation (EC) No 1907/2006 of the European Parliament and of the Council of 18 December 2006 concerning the Registration, Evaluation, Authorisation and Restriction of Chemicals (REACH), establishing a European Chemicals Agency, amending Directive 1999/45/EC and repealing Council Regulation (EEC) No 793/93 and Commission Regulation (EC) No 1488/94 as well as Council Directive 76/769/EEC and Commission Directives 91/155/EEC, 93/67/EEC, 93/105/EC and 2000/21/EC*. Official Journal of the European Union.
6. Phani, G., et al., *Titania solar cells: new photovoltaic technology.* Renewable Energy, 2001. **22**(1-3): p. 303-309.
7. Iv, M., et al., *Clinical applications of iron oxide nanoparticles for magnetic resonance imaging of brain tumors.* Nanomedicine (Lond), 2015. **10**(6): p. 993-1018.
8. Rujitanaroj, P.-o., N. Pimpha, and P. Supaphol, *Wound-dressing materials with antibacterial activity from electrospun gelatin fiber mats containing silver nanoparticles.* Polymer, 2008. **49**(21): p. 4723-4732.
9. Yuan, G. and R. Cranston, *Recent Advances in Antimicrobial Treatments of Textiles.* Textile Research Journal, 2008. **78**(1): p. 60-72.
10. Rivero, P.J., et al., *Nanomaterials for Functional Textiles and Fibers.* Nanoscale Res Lett, 2015. **10**(1): p. 501.
11. Jain, P. and T. Pradeep, *Potential of silver nanoparticle-coated polyurethane foam as an antibacterial water filter*. Biotechnol Bioeng, 2005. **90**(1): p. 59-63.
12. Mahltig, B., H. Haufe, and H. Böttcher, *Functionalisation of textiles by inorganic sol–gel coatings.* Journal of Materials Chemistry, 2005. **15**(41): p. 4385.
13. Smijs, T.G. and S. Pavel, *Titanium dioxide and zinc oxide nanoparticles in sunscreens: focus on their safety and effectiveness.* Nanotechnol Sci Appl, 2011. **4**: p. 95-112.
14. Schilling, K., et al., *Human safety review of "nano" titanium dioxide and zinc oxide.* Photochemical & Photobiological Sciences, 2010. **9**(4): p. 495-509.
15. Alexander, J.W., *History of the medical use of silver.* Surg Infect (Larchmt), 2009. **10**(3): p. 289-92.
16. Levard, C., et al., *Environmental Transformations of Silver Nanoparticles: Impact on Stability and Toxicity.* Environmental Science & Technology, 2012. **46**(13): p. 6900-6914.
17. Wilkinson, L.J., R.J. White, and J.K. Chipman, *Silver and nanoparticles of silver in wound dressings: a review of efficacy and safety.* J Wound Care, 2011. **20**(11): p. 543-9.
18. Appendini, P. and J.H. Hotchkiss, *Review of antimicrobial food packaging.* Innovative Food Science & Emerging Technologies, 2002. **3**(2): p. 113-126.

19. Tian, J., et al., *Topical delivery of silver nanoparticles promotes wound healing.* ChemMedChem, 2007. **2**(1): p. 129-36.
20. Praveena, S.M. and A.Z. Aris, *Application of Low-Cost Materials Coated with Silver Nanoparticle as Water Filter in Escherichia coli Removal.* Water Quality, Exposure and Health, 2015. **7**(4): p. 617-625.
21. Rai, M., A. Yadav, and A. Gade, *Silver nanoparticles as a new generation of antimicrobials.* Biotechnol Adv, 2009. **27**(1): p. 76-83.
22. Piccinno, F., et al., *Industrial production quantities and uses of ten engineered nanomaterials in Europe and the world.* Journal of Nanoparticle Research, 2012. **14**(9): p. 1-11.
23. Giddings, J., F. Yang, and M. Myers, *Flow-field-flow fractionation: a versatile new separation method.* Science, 1976. **193**(4259): p. 1244-1245.
24. Nolte, D.D., *Diffraction and Light Scattering.* 2012: p. 49-94.
25. Cölfen, H. and T. Pauck, *Determination of particle size distributions with angström resolution.* Colloid and Polymer Science, 1997. **275**(2): p. 175-180.
26. Krpetic, Z., et al., *High-resolution sizing of monolayer-protected gold clusters by differential centrifugal sedimentation.* ACS Nano, 2013. **7**(10): p. 8881-90.
27. Ruf, H., *Data accuracy and resolution in particle sizing by dynamic light scattering.* Advances in Colloid and Interface Science, 1993. **46**: p. 333-342.
28. Berne, B.J. and P. Robert, *Dynamic Light Scattering: With Applications to Chemistry, Biology, and Physics*. 1976: R.. New York, NY (USA): Wiley-Interscience.
29. Gun'ko, V.M., et al., *Photon correlation spectroscopy investigations of proteins.* Advances in Colloid and Interface Science, 2003. **105**(1–3): p. 201-328.
30. Calzolai, L., et al., *Separation and characterization of gold nanoparticle mixtures by flow-field-flow fractionation.* J Chromatogr A, 2011. **1218**(27): p. 4234-9.
31. Kaszuba, M., et al., *Resolving Concentrated Particle Size Mixtures Using Dynamic Light Scattering.* Particle & Particle Systems Characterization, 2007. **24**(3): p. 159-162.
32. Chang, T.H., et al., *Crystal structure of vaccinia viral A27 protein reveals a novel structure critical for its function and complex formation with A26 protein.* PLoS Pathog, 2013. **9**(8): p. e1003563.
33. Baalousha, M., et al., *Size fractionation and characterization of natural colloids by flow-field flow fractionation coupled to multi-angle laser light scattering.* J Chromatogr A, 2006. **1104**(1-2): p. 272-81.
34. Iavicoli, P., et al., *Application of Asymmetric Flow Field-Flow Fractionation hyphenations for liposome–antimicrobial peptide interaction.* Journal of Chromatography A, 2015. **1422**: p. 260-269.
35. Sandercock, J.R., *Trends in brillouin scattering: Studies of opaque materials, supported films, and central modes.* 1982. **51**: p. 173-206.
36. Milne, J.L.S., et al., *Cryo-electron microscopy: A primer for the non-microscopist.* The FEBS journal, 2013. **280**(1): p. 28-45.
37. Spurr, A.R., *A low-viscosity epoxy resin embedding medium for electron microscopy.* Journal of Ultrastructure Research, 1969. **26**(1): p. 31-43.
38. de Jonge, M.D., et al., *Quantitative 3D elemental microtomography of Cyclotella meneghiniana at 400-nm resolution.* Proceedings of the National Academy of Sciences, 2010. **107**(36): p. 15676-15680.
39. Ashoka, S., et al., *Comparison of digestion methods for ICP-MS determination of trace elements in fish tissues.* Analytica Chimica Acta, 2009. **653**(2): p. 191-199.
40. Mitrano, D.M., et al., *Detecting nanoparticulate silver using single-particle inductively coupled plasma-mass spectrometry.* Environ Toxicol Chem, 2012. **31**(1): p. 115-21.

41. Mitrano, D.M., et al., *Tracking dissolution of silver nanoparticles at environmentally relevant concentrations in laboratory, natural, and processed waters using single particle ICP-MS (spICP-MS).* Environmental Science: Nano, 2014. **1**(3): p. 248.
42. Raventós, M., S. Duarte, and R. Alarcón, *Application and Possibilities of Supercritical CO2 Extraction in Food Processing Industry: An Overview.* Food Science and Technology International, 2002. **8**(5): p. 269-284.
43. Moore, W.N. and L.T. Taylor, *Analytical inverse supercritical fluid extraction of polar pharmaceutical compounds from cream and ointment matrices.* Journal of Pharmaceutical and Biomedical Analysis, 1994. **12**(10): p. 1227-1232.
44. Long, T.C., et al., *Nanosize Titanium Dioxide Stimulates Reactive Oxygen Species in Brain Microglia and Damages Neurons in Vitro.* Environmental Health Perspectives, 2007. **115**(11): p. 1631-1637.
45. Miller, R.J., et al., *TiO₂ Nanoparticles Are Phototoxic to Marine Phytoplankton.* PLoS ONE, 2012. **7**(1): p. e30321.
46. Miller, R.J., et al., *Impacts of Metal Oxide Nanoparticles on Marine Phytoplankton.* Environmental Science & Technology, 2010. **44**(19): p. 7329-7334.
47. Zhu, X., J. Zhou, and Z. Cai, *TiO2 Nanoparticles in the Marine Environment: Impact on the Toxicity of Tributyltin to Abalone (Haliotis diversicolor supertexta) Embryos.* Environmental Science & Technology, 2011. **45**(8): p. 3753-3758.
48. Carlson, C., et al., *Unique Cellular Interaction of Silver Nanoparticles: Size-Dependent Generation of Reactive Oxygen Species.* The Journal of Physical Chemistry B, 2008. **112**(43): p. 13608-13619.
49. Sanders, J., G. Abbe, and G. Riedel, *Silver uptake and subsequent effects on growth and species composition in an estuarine community.* Science of The Total Environment, 1990. **97-98**: p. 761-769.
50. Reinfelder, J.R. and S.I. Chang, *Speciation and Microalgal Bioavailability of Inorganic Silver.* Environmental Science & Technology, 1999. **33**(11): p. 1860-1863.
51. Boenigk, J., et al., *Effects of Silver Nitrate and Silver Nanoparticles on a Planktonic Community: General Trends after Short-Term Exposure.* PLoS ONE, 2014. **9**(4): p. e95340.
52. Mulley, G., A.T.A. Jenkins, and N.R. Waterfield, *Inactivation of the Antibacterial and Cytotoxic Properties of Silver Ions by Biologically Relevant Compounds.* PLoS ONE, 2014. **9**(4): p. e94409.
53. Liau, S.Y., et al., *Interaction of silver nitrate with readily identifiable groups: relationship to the antibacterialaction of silver ions.* Letters in Applied Microbiology, 1997. **25**(4): p. 279-283.
54. Loeschner, K., et al., *Distribution of silver in rats following 28 days of repeated oral exposure to silver nanoparticles or silver acetate.* Particle and Fibre Toxicology, 2011. **8**(1): p. 18.
55. Wagner, P.A., W.G. Hoekstra, and H.E. Ganther, *Alleviation of Silver Toxicity by Selenite in the Rat in Relation to Tissue Glutathione Peroxidase.* Experimental Biology and Medicine, 1975. **148**(4): p. 1106-1110.
56. Van Vleet, J.F., *Induction of lesions of selenium-vitamin E deficiency in pigs fed silver.* American journal of veterinary research, 1976. **37**(12): p. 1415-1420.
57. Ganther, H.E., *INTERACTIONS OF VITAMIN E AND SELENIUM WITH MERCURY AND SILVER.* Annals of the New York Academy of Sciences, 1980. **355**(1): p. 212-226.
58. Chen, C., et al., *Experimental Platform to Study Heavy Metal Ion−Enzyme Interactions and Amperometric Inhibitive Assay of Ag+ Based on Solution State and Immobilized Glucose Oxidase.* Analytical Chemistry, 2011. **83**(7): p. 2660-2666.

59. Skjolding, L.M., et al., *A Critical Review of Aquatic Ecotoxicity Testing of Nanoparticles - The Quest for Disclosing Nanoparticle Effects.* Angewandte Chemie International Edition, 2016: p. n/a-n/a.
60. Benn, T.M. and P. Westerhoff, *Nanoparticle silver released into water from commercially available sock fabrics.* Environmental Science & Technology, 2008. **42**(11): p. 4133-4139.
61. Kaegi, R., et al., *Release of silver nanoparticles from outdoor facades.* Environmental Pollution, 2010. **158**(9): p. 2900-2905.
62. Turetta, C., et al., *Trace element determination in seawater by ICP-SFMS coupled with a microflow nebulization/desolvation system.* Analytical and Bioanalytical Chemistry, 2004. **380**(2): p. 258-268.
63. Hans Wedepohl, K., *The composition of the continental crust.* Geochimica et Cosmochimica Acta, 1995. **59**(7): p. 1217-1232.
64. Wen, B., et al., *Preconcentration of trace elements in sea water with poly (acrylaminophosphonic – dithiocarbamate) chelating fiber for their determination by inductively coupled plasma mass spectrometry.* Fresenius' Journal of Analytical Chemistry, 1999. **363**(3): p. 251-255.
65. Sagee, O., I. Dror, and B. Berkowitz, *Transport of silver nanoparticles (AgNPs) in soil.* Chemosphere, 2012. **88**(5): p. 670-675.
66. Schlich, K. and K. Hund-Rinke, *Influence of soil properties on the effect of silver nanomaterials on microbial activity in five soils.* Environmental Pollution, 2015. **196**: p. 321-330.
67. Cornelis, G., et al., *Retention and Dissolution of Engineered Silver Nanoparticles in Natural Soils.* Soil Science Society of America Journal, 2012. **76**(3): p. 891-902.
68. Kaegi, R., et al., *Behavior of Metallic Silver Nanoparticles in a Pilot Wastewater Treatment Plant.* Environmental Science & Technology, 2011. **45**(9): p. 3902-3908.
69. Xiu, Z.-m., et al., *Negligible particle-specific antibacterial activity of silver nanoparticles.* Nano Letters, 2012. **12**(8): p. 4271-4275.
70. Sharma, V.K., et al., *Organic-coated silver nanoparticles in biological and environmental conditions: Fate, stability and toxicity.* Advances in Colloid and Interface Science, 2014. **204**(0): p. 15-34.
71. Liu, J., et al., *Controlled Release of Biologically Active Silver from Nanosilver Surfaces.* ACS Nano, 2010. **4**(11): p. 6903-6913.
72. Dobias, J. and R. Bernier-Latmani, *Silver Release from Silver Nanoparticles in Natural Waters.* Environmental Science & Technology, 2013. **47**(9): p. 4140-4146.
73. Byrne, R.H., *Inorganic speciation of dissolved elements in seawater: the influence of pH on concentration ratios.* Geochemical Transactions, 2002. **3**(1): p. 1-6.
74. Hong, H., et al., *Characterization of dissolved organic matter under contrasting hydrologic regimes in a subtropical watershed using PARAFAC model.* Biogeochemistry, 2012. **109**(1): p. 163-174.
75. Cumberland, S.A. and J.R. Lead, *Particle size distributions of silver nanoparticles at environmentally relevant conditions.* Journal of Chromatography A, 2009. **1216**(52): p. 9099-9105.
76. Zhu, M., et al., *The effect of humic acid on the aggregation of titanium dioxide nanoparticles under different pH and ionic strengths.* Science of The Total Environment, 2014. **487**: p. 375-380.
77. Gunsolus, I.L., et al., *Effects of Humic and Fulvic Acids on Silver Nanoparticle Stability, Dissolution, and Toxicity.* Environmental Science & Technology, 2015. **49**(13): p. 8078-8086.

78. Aiken, G.R., H. Hsu-Kim, and J.N. Ryan, *Influence of Dissolved Organic Matter on the Environmental Fate of Metals, Nanoparticles, and Colloids.* Environmental Science & Technology, 2011. **45**(8): p. 3196-3201.
79. Thalmann, B., et al., *Effect of humic acid on the kinetics of silver nanoparticle sulfidation.* Environmental Science: Nano, 2016. **3**(1): p. 203-212.
80. Boullemant, A., et al., *UPTAKE OF LIPOPHILIC CADMIUM COMPLEXES BY THREE GREEN ALGAE: INFLUENCE OF HUMIC ACID AND ITS pH DEPENDENCE1.* Journal of Phycology, 2011. **47**(4): p. 784-791.
81. Loosli, F., P. Le Coustumer, and S. Stoll, *Impact of alginate concentration on the stability of agglomerates made of TiO2 engineered nanoparticles: Water hardness and pH effects.* Journal of Nanoparticle Research, 2015. **17**(1): p. 44.
82. Loosli, F., P. Le Coustumer, and S. Stoll, *Effect of electrolyte valency, alginate concentration and pH on engineered TiO2 nanoparticle stability in aqueous solution.* Science of The Total Environment, 2015. **535**: p. 28-34.
83. Hsiao, I.-L., et al., *Quantification and visualization of cellular uptake of TiO2 and Ag nanoparticles: comparison of different ICP-MS techniques.* Journal of Nanobiotechnology, 2016. **14**(1): p. 50.
84. Milić, M., et al., *Cellular uptake and toxicity effects of silver nanoparticles in mammalian kidney cells.* Journal of Applied Toxicology, 2015. **35**(6): p. 581-592.
85. Gitrowski, C., A.R. Al-Jubory, and R.D. Handy, *Uptake of different crystal structures of TiO2 nanoparticles by Caco-2 intestinal cells.* Toxicology Letters, 2014. **226**(3): p. 264-276.
86. Farkas, J., et al., *Uptake and effects of manufactured silver nanoparticles in rainbow trout (Oncorhynchus mykiss) gill cells.* Aquatic Toxicology, 2011. **101**(1): p. 117-125.
87. Kwok, K.W.H., et al., *Uptake of silver nanoparticles and toxicity to early life stages of Japanese medaka (Oryzias latipes): Effect of coating materials.* Aquatic Toxicology, 2012. **120–121**: p. 59-66.
88. Maurer, L.L., et al., *Intracellular trafficking pathways in silver nanoparticle uptake and toxicity in Caenorhabditis elegans.* Nanotoxicology, 2016. **10**(7): p. 831-835.
89. Burchardt, A.D., et al., *Effects of Silver Nanoparticles in Diatom Thalassiosira pseudonana and Cyanobacterium Synechococcus sp.* Environmental Science & Technology, 2012. **46**(20): p. 11336-11344.
90. Miao, A.-J., et al., *Intracellular Uptake: A Possible Mechanism for Silver Engineered Nanoparticle Toxicity to a Freshwater Alga <italic>Ochromonas danica</italic>.* PLoS ONE, 2010. **5**(12): p. e15196.
91. Książyk, M., et al., *Toxic Effect of Silver and Platinum Nanoparticles Toward the Freshwater Microalga Pseudokirchneriella subcapitata.* Bulletin of Environmental Contamination and Toxicology, 2015. **94**(5): p. 554-558.
92. Pletikapić, G., et al., *Atomic force microscopy characterization of silver nanoparticles interactions with marine diatom cells and extracellular polymeric substance.* Journal of Molecular Recognition, 2012. **25**(5): p. 309-317.
93. Denys, L., *Relation of abundance-weighted averages of diatom indicator values to measured environmental conditions in standing freshwaters.* Ecological Indicators, 2004. **4**(4): p. 255-275.
94. Rovira, L., R. Trobajo, and C. Ibáñez, *The use of diatom assemblages as ecological indicators in highly stratified estuaries and evaluation of existing diatom indices.* Marine Pollution Bulletin, 2012. **64**(3): p. 500-511.
95. Carvalho, R.N., et al., *Gene biomarkers in diatom Thalassiosira pseudonana exposed to polycyclic aromatic hydrocarbons from contaminated marine surface sediments.* Aquatic Toxicology, 2011. **101**(1): p. 244-253.

96. Friedrich, J.P., *Supercritical CO2 extraction of lipids from lipid-containing materials*. 1984, Google Patents.
97. Iavicoli, P., et al., *Application of Asymmetric Flow Field-Flow Fractionation hyphenations for liposome-antimicrobial peptide interaction.* J Chromatogr A, 2015. **1422**: p. 260-9.
98. Al-Kattan, A., et al., *Behavior of TiO2 Released from Nano-TiO2-Containing Paint and Comparison to Pristine Nano-TiO2.* Environmental Science & Technology, 2014. **48**(12): p. 6710-6718.
99. Silver, S., *Bacterial silver resistance: molecular biology and uses and misuses of silver compounds.* FEMS Microbiology Reviews, 2003. **27**(2-3): p. 341-353.
100. Percival, S.L., P.G. Bowler, and D. Russell, *Bacterial resistance to silver in wound care.* Journal of Hospital Infection. **60**(1): p. 1-7.
101. Tourinho, P.S., et al., *Metal-based nanoparticles in soil: Fate, behavior, and effects on soil invertebrates.* Environmental Toxicology and Chemistry, 2012. **31**(8): p. 1679-1692.
102. Geiss, O., et al., *Size and mass determination of silver nanoparticles in an aqueous matrix using asymmetric flow field flow fractionation coupled to inductively coupled plasma mass spectrometer and ultraviolet–visible detectors.* Journal of Chromatography A, 2013. **1321**(0): p. 100-108.
103. Haiss, W., et al., *Determination of Size and Concentration of Gold Nanoparticles from UV−Vis Spectra.* Analytical Chemistry, 2007. **79**(11): p. 4215-4221.
104. Bhui, D.K., et al., *Synthesis and UV–vis spectroscopic study of silver nanoparticles in aqueous SDS solution.* Journal of Molecular Liquids, 2009. **145**(1): p. 33-37.
105. Kantak, A.S., M. Srinivas, and B.K. Gale, *Effect of Carrier Ionic Strength in Microscale Cyclical Electrical Field-Flow Fractionation.* Analytical Chemistry, 2006. **78**(8): p. 2557-2564.
106. *Directive 2000/60/EC of the European Parliament and of the Council of 23 October 2000 establishing a framework for Community action in the field of water policy*. Official Journal of the European Communities.

Estes anexos só estão disponíveis para consulta através do CD-ROM.
Queira por favor dirigir-se ao balcão de atendimento da Biblioteca.

Serviços de Biblioteca, Informação Documental e Museologia
Universidade de Aveiro